UNIVERSITÀ DEGLI STUDI DI TORINO

Department of Physics

PhD School in Physics – XXXIV cycle

Tailoring the optical, structural and surface properties of artificial diamond for biomedical applications

Supervisor:

Prof. Ettore Vittone

Candidate:

Pietro Aprà

Co-supervisor:

Dr. Federico Picollo

PhD school coordinator:

Prof. Paolo Olivero

Academic years 2018 – 2021

To my mother, my father and Saetta.

“I won't be impressed with science
until I can download a waffle”
- Sean Gabay

“If we knew what we were doing,
it wouldn’t be called research”
- Albert Einstein

“Sometimes I think the surest sign that
intelligent life exists elsewhere in the universe
is that none of it has tried to contact us"
- Bill Watterson (Calvin and Hobbes)

“One measurement, one publication.
Two measurements, no publication”
-Anonymous

Summary

Preface

During the last decades, micro-nanotechnology turned out to be a promising field of research. One of its most prominent applications are found in the context of biomedicine, leading to the definition of new disciplines known under the names of *nanobiotechnology and nanomedicine*. Indeed, many micro- and nanosystems are under development with purposes such as biosensing, tissue engineering, drug delivery, nanodiagnostic and biolabeling.

In these contexts, diamond is acquiring ever-increasing interest, due to its biocompatibility, chemical inertness, durability and transparency. Bulk diamond has been widely studied and modified to obtain tailored biosensors with the capability of detecting electrochemical activities of cultured cells or biological magnetic fields.

Moreover, diamond nanocrystals (or nanodiamonds) have gained a solid reputation in the biomedical field thanks to the possibility to easily modify their surface with specific biomolecules or drugs, together with their applicability as fluorescent biomarkers, thanks to the presence of optically active defects in their crystal lattice (e.g.: NV centers).

The main perspective of the work carried out in this thesis is the development and characterization of diamond-based biosensors and drug delivery systems, by using ion beam-based techniques and thermal modification processes of diamond.

More precisely, graphitic structures of a diamond biosensor for excitable cells analysis and fluorescent NV centers in nanodiamonds were realized with ion-beam fabrication and characterized with Raman/PL spectroscopy, providing useful structural and optical information for the optimization of these processes.

In addition, nanodiamonds were also investigated in terms of surface chemistry (DRIFT spectroscopy), dispersibility (DLS analysis) and electrical conductivity, with the final goal of making them suitable for further biochemical functionalization and for biological optical tracking.

This activity has been conducted in the context of the Solid-State Physics group of the University of Torino, but due to its strong interdisciplinarity, the work was carried out in close collaboration with researchers of chemistry, drug science, electrophysiology and neuroscience.

The manuscript is organized as follows:

- Chapter 1 presents the context in which the work is inserted, together with a description of the main physical and chemical properties of diamond and nanodiamonds, as well as the modification and ion-beam-assisted techniques for the functionalization of this material (creation of graphitic structures and fluorescent color centers).

- Chapter 2 is dedicated to the description of the instrumentation employed both for modifying and characterizing the samples.

- Chapter 3 includes a detailed description of the implemented processing techniques and presents the main results obtained in the modification and characterization of diamond and nanodiamonds samples.

- Chapter 4 summarizes the main results and presents the conclusions of the work, together with an overview of possible future developments of this research activity.

1 Introduction

1.1 Micro-nanotechnology

Micro-nanotechnology is an ever-growing research field that deals with the control and manipulation of matter at the micro and nanometric level, by developing processes of synthesis, characterization and application of nanostructured materials and devices. Its strong interdisciplinarity requires the integration of multiple scientific fields, such as physics, chemistry, biology, materials science, computer science and engineering.

Over the years, micro-nanotechnology gained increasing success, providing significant technological innovations in contexts such as nanoelectronics, mechanics, energy, environmental pollution and biomedicine. For the purposes of this thesis, it is important to deepen the aspects related to the latter topic. Indeed, micro-nanotechnology has proven extremely proactive in this field due to the typical size of the cells at the basis of living beings (1-10 μm). The cells themselves are constituted by different sub-micrometric compartments and macromolecules, such as nucleic acids and proteins, which are a few nanometers sized. Healthcare applications are thus in constant development, spacing between surgery, cancer diagnosis and therapy, identification of disease markers, molecular imaging, implantology, tissue engineering and drug delivery [1]. In these contexts, an increasing number of products are under clinical translation and many devices are already found in regular clinical practice. Different microdevices have been developed to measure with high sensitivity the responses of cells and biomolecules to mechanical [2–4], electrical, magnetic and chemical stimuli [5] (the so-called "lab-on-a-chip"). In these devices, microelectrodes and microchannels can be realized with dimensions comparable with those of single cells, allowing their investigation and the recording of multiple signals at the molecular [6]. Other micrometric devices called BioMEMS (MicroElectroMechanical Systems) are already found in pacemakers, glucose sensors, microcantilever-based systems for biomolecular detection or DNA microarray chips and are constantly opening to huge possibilities in future biomedical techniques [7]. In general, these miniaturized devices provide also advantages such as reduced manufacturing cost, improved portability, smaller sample sizes and reagents quantities. Ever-improving optical techniques are also employed to image biological microstructures and observe molecular mechanisms inside cells and tissues [8]. Many studies demonstrated how to integrate micro/nano fabrication techniques to shed light on the molecular mechanism of cellular

signaling and transduction, including the use of scaffolds for tissue engineering and micro-patterned devices for cellular environment manipulation to observe the response in terms of cells differentiation, proliferation and migration [5].

In the frame of nanobiotechnology, the most investigated and promising nanostructures with application diagnosis and therapy are nanoparticles (NP) (Figure 1), with typical sizes ranging from few nanometers up to 100-200 nm. Due to its centrality for this thesis, this topic will be discussed more in detail in the next section (1.2).

1.2 Nanoparticles in biomedicine

By virtue of their size, nanoparticles possess peculiar chemical and physical properties that are distinguished from those of bulk materials. According to their purpose, nanoparticles can be engineered to meet specific requirements (selectivity, size, shape, biocompatibility, etc.). The following paragraphs will present some of the current, or under development, applications.

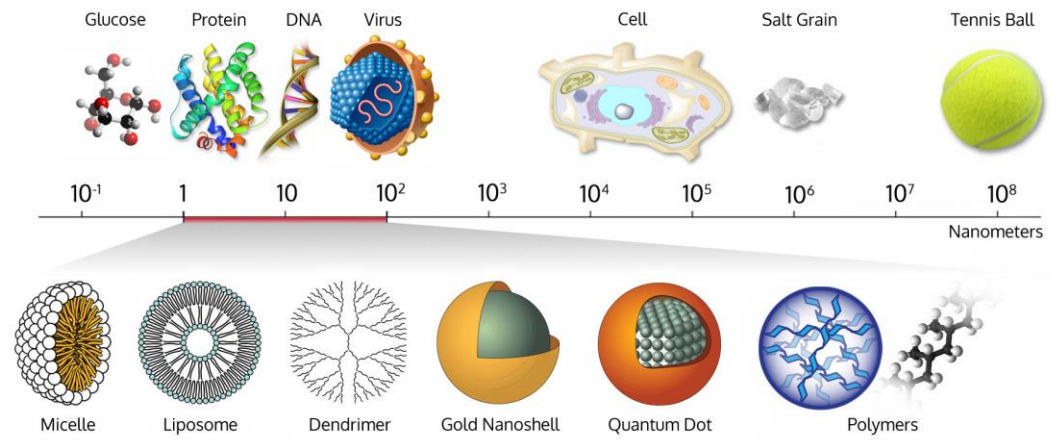

Figure 1: size scale and variety of potentially used nanoparticles in biomedicine [9].

1.2.1 Drug delivery

Drug delivery refers to all the approaches and technologies aimed at developing drug transport systems to specific targets in the human body [10]. The intention is to implement selective conveyance at the site of the pathology, overcoming biological barriers and avoiding healthy organs and tissues. In this manuscript, the integration of appropriate molecules on the surface of the nanomaterial to obtain the desired properties and specificities, will be referred as "functionalization". Once reached the target location, nanoparticles can be internalized into cells mainly by endocytosis or through the formation of large pores on the cytoplasmic membrane [11].

Several treatments for cancer, pain and nanoparticle-based infections have already been introduced into clinical practice. Among the first classes of therapeutic nanoparticles to receive approval for cancer treatment there are liposomes, in particular liposomal doxorubicin (LD) and nab-paclitaxel complex, consisting of chemotherapy (paclitaxel) encapsulated in an albumin micelle [1]. More recently, liposomes have been used to deliver nucleic acid therapeutics such as small interfering RNAs, and the first approved vaccines designed to face COVID-19 pandemic are actually based on this technology [12]. In addition to organic systems, polymeric and inorganic nanoparticles are also common in biomedical research [13]. Depending on their structure, they can be distinguished into *nanospheres,* if the drug is dispersed within a matrix, or *nanocapsules,* if it is confined within a coating membrane. Alternatively, drugs can be chemically bound to the surface of the nanoparticles themselves.

In the following paragraphs, the main biomedical applications of nanoparticles will be briefly discussed.

1.2.2 Cancer therapy

Cancer is a widespread disease all over the world. On average, one in three people in Europe is diagnosed with cancer in their lifetime. The therapy methods are multiple and often not exclusive to each other, depending on the type and the staging of the disease.

Tumor tissues are typically characterized by dense vascularization rich in fenestrations (small pores), thus exempting a greater supply of oxygen and nutriment to support the high metabolic activity of the cancer cells. This phenomenon is referred as "*Enhanced Permeability and Retention* (EPR)" [14]. Recently the development of nanotechnology has introduced new potential tools in the field of oncology, offering interesting innovations in both diagnostic and therapeutic terms. In particular, nanoparticles can be engineered to take advantage of the passive effect of EPR and to accumulate in tumor tissues [15]. However, based only on this mechanism, it is not possible to avoid the accumulation of nanoparticles even in other tissues that naturally possess fenestrated blood vessels such as liver and kidneys [16]. To overcome this problem, active targeting can be carried out by attacking ligands on the surface of the nanoparticles (Figure 2). Such ligands have a high specificity for certain receptors typically overexpressed on the membrane of cancer cells (e.g. glycans) [17] and their integration on the nanoparticle surface can reduce or eliminate the non-specific uptake by healthy tissues. Possible ligands include transferrin, folic acid, enzymes, proteins and properly engineered antibodies. Another advantage of using nano-vectors is the

possibility to load on them multiple drugs, thus allowing the implementation of a combined and more effective therapy.

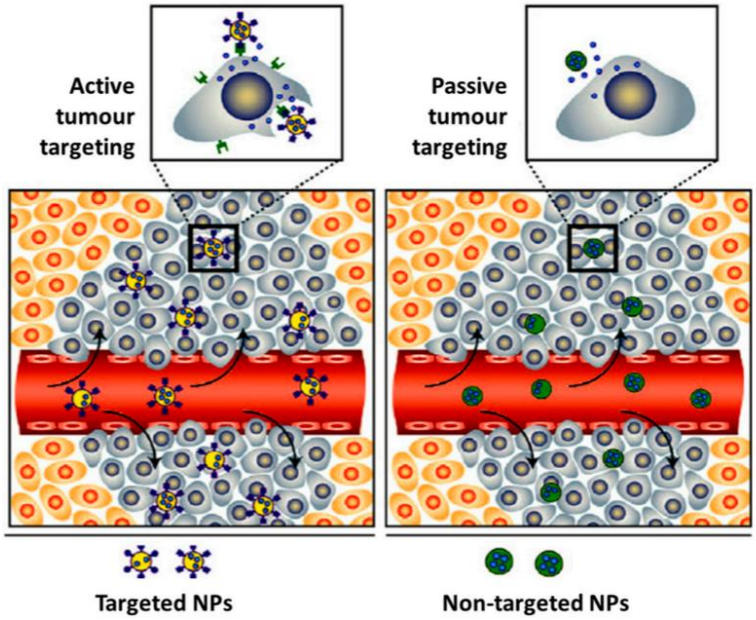

Figure 2: active and passive nanoparticles targeting mechanisms for cancer therapy [18].

1.2.3 Radiosensitizers

Nanoparticles are acquiring great interest also for enhancing radiotherapy. Often, high doses of ionizing radiation would be necessary to better treat cancer tissues. However, the potentially harmful effects of radiation on healthy tissues and the side effects, limit the use of higher doses. A possible strategy is to reduce the delivered radiation dose while enhancing its effects on tumor cells by using radiosensitizing agents (RS), which are usually constituted by macromolecules or nanomaterials [19,20]. Due to their possibility of being delivered to the tumour environment, different nanoparticles have been studied as RS. The principle underlying NP radio-enhancement is their potential to release electrons under irradiation, with consequent boosting of the induced ionization at the basis of cancer cells death (Figure 3). In this context, mainly high atomic number metal NP, including silver, platinum, and gold [19], have been investigated. Indeed, high atomic number materials require lower energies for photoelectric effect or Compton scattering to occur, thus easily releasing electrons and increasing the formation of the Reactive Oxygen Species (ROS) responsible for DNA damage and cells death. Several in-vitro and in-vivo experiments have provided evidence for the effectiveness of radio-enhancement by metal NP [19,21]. However, some studies have also shown that metal NP can be cytotoxic and reduce cell viability, then being unsuitable for clinical use [22,23].

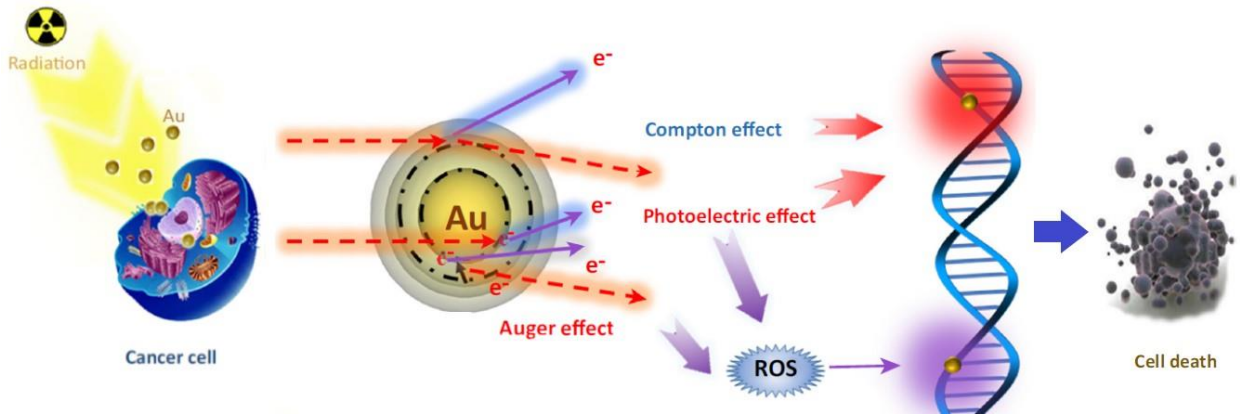

Figure 3: radiosensitizing mechanism of a metal NP (e.g.: Au) [20].

1.2.4 Other applications

The applications of nanoparticles in biomedicine are countless, here an inexhaustive list of few other examples is reported.

Worthwhile of mention is the necessity of transporting drugs to the central nervous system, which is severely restricted by the blood brain barrier (BBB) that prevents the brain from harmful and exogenous substances [24]. Some studies have shown that nanoparticles are able to facilitate the passage of drugs through BBB [25,26].

Several infectious diseases may in the future be treated with nanoparticle therapies. Numerous studies aimed at identifying drugs and treatment plans to combat the HIV virus. One of the fundamental problems is inherent to the process of replication of the virus, during which a large number of mutations make it resistant to antiviral drugs [27]. In a work by Elechiguerra et al. [28] it has been shown that silver nanoparticles are capable of interacting with the HIV-1 virus by inhibiting the cell attack (and therefore its replication).

Finally, superparamagnetic nanoparticles, such as iron oxide, are under investigation as contrast agents in magnetic resonance imaging (MRI) or to induce hyperthermia in cancer tissues to destroy the pathological cells [29,30].

1.3 Fluorescent bio-labelers

The observation and imaging of biological processes in cells or tissues with optical microscopy is often carried out with the aid of fluorescent substances, called fluorophores. These exist in many varieties, both organic and inorganic, and allow to locate and track the movement of specific molecules integrated into them.

One of the most employed fluorophores in biology is the "Green Fluorescent Protein" (GFP). Due to its protein nature, GFP (Figure 4) can be encoded in DNA so that it is expressed in connection with the structures to be traced in the cells of the sample under investigation. Although organic fluorophores are widely used, they possess two main limitations consisting in a generally low quantum yield and a high susceptibility to photobleaching phenomena (i.e.: a reduction in fluorescence properties due to their photochemical degradation).

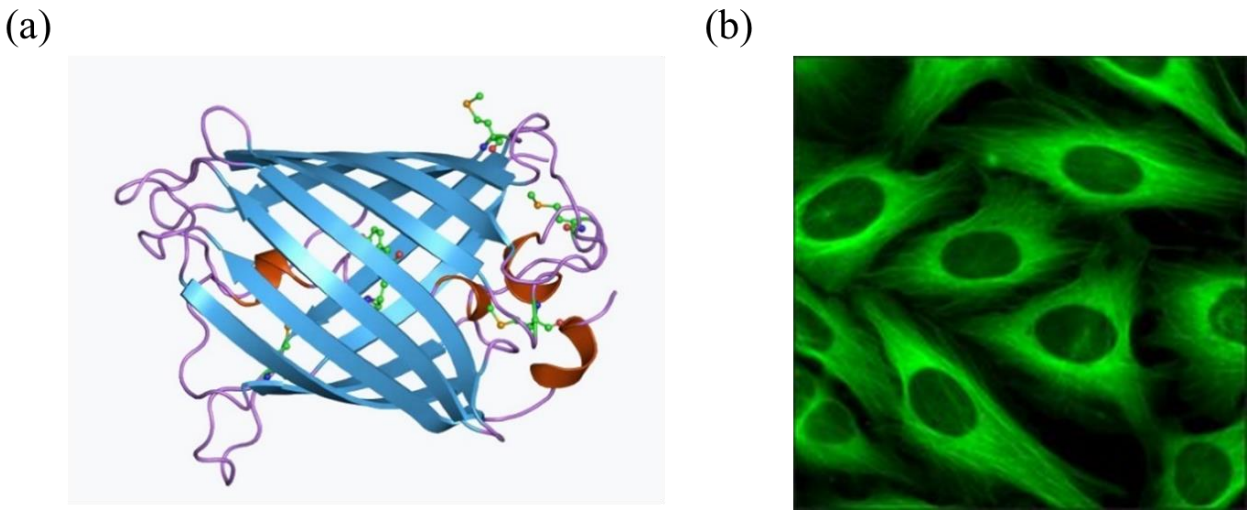

Figure 4: (a) three-dimensional protein structure of GFP; (b) optical microscope photography of cells in which the tubulin has been genetically marked with GFP [31].

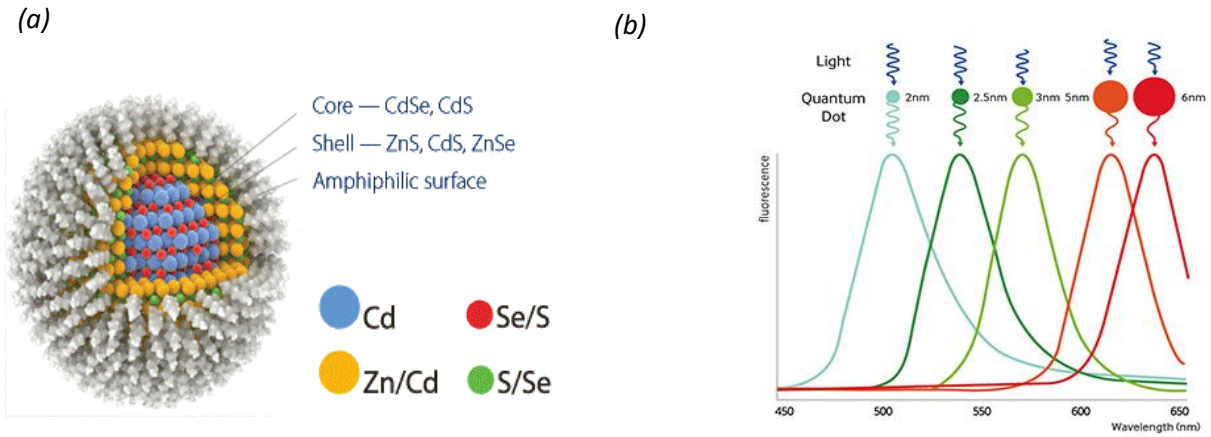

Figure 5: (a) schematic configuration of a quantum dot, with a CdS/CdSe core and shell constituted by ZnS, ZnSe and CdS; (b) quantum dots emission spectra depending on nanocrystal size [32].

Also in this context, nanomaterials can provide alternative solutions. It is the case, for example, of Quantum Dots (QD), which have a high intensity of photoluminescence and photostability. QD are nanocrystals formed by inclusion of semiconductor material within another semiconductor with a wider energy gap (e.g. CdSe coated by ZnS) [33]. The emission spectrum is adjustable by properly tuning the nanocrystals size (Figure 5). Nonetheless, even such systems possess important limitations represented mainly by their cytotoxicity [34].

In general, the development of new potential inorganic biomarkers is parallel with the discovery of new lattice defects in solids, which introduce intermediate levels into the energy gap, thus allowing electronic transitions at the basis of their fluorescent properties (optically active defects). This type of emissions, due to the absence of chemical degradation typical of biomolecular systems such as GFP, are typically characterized by high efficiency and temporal stability.

1.4 Diamond

Among the wide variety of materials under investigation for biomedical micro-nanotechnologies, artificial diamond is emerging as one of the most appealing. Many studies highlighted its excellent biocompatibility [35–37], which is an essential feature when willing to interface a material with biological systems. In addition, its chemical inertness avoids interactions with the culture medium or the cellular environment, while its wide optical transparency window makes it useable with fluorescence microscopy. Interestingly, the electrical properties of diamond substrates can be modified by means of either doping [38] or inducing a transition to the graphitic phase [39–41], thus allowing the realization of conductive electrodes, as will be better discussed in 1.5.1.

Based on these properties, the solid-state physics group of the University of Torino among which this thesis work was carried out, has been devoted for a long time to the development of this kind of techniques to create diamond-based biosensors for detecting electrochemical signals from cultured cells. Recently, also diamond nanocrystals, or nanodiamonds (ND), started to be investigated by the solid-state physics research group, in parallel with the activity carried out by the candidate. Because of its centrality in this thesis, the next paragraphs are dedicated to the properties and the modification techniques of diamond.

1.4.1 Diamond properties

Diamond (from Greek αδαμας, adamas: "indestructible") is one of the allotropic forms of carbon. This element is a second period (group IV) non-metal with electronic configuration [He] $2s^2 2p^2$. Its chemical combination depends on the type of hybridization of the external s and p orbitals. In the case of diamond, hybridization is in sp^3 configuration, which allows the establishment of

covalent bonds with 4 other carbon atoms, forming a robust tetrahedral structure. Conversely, sp^2 hybridized carbon is at the basis of graphite, which is characterized by overlaps of solid hexagonal-structured planes held together by weak Van der Waals forces.

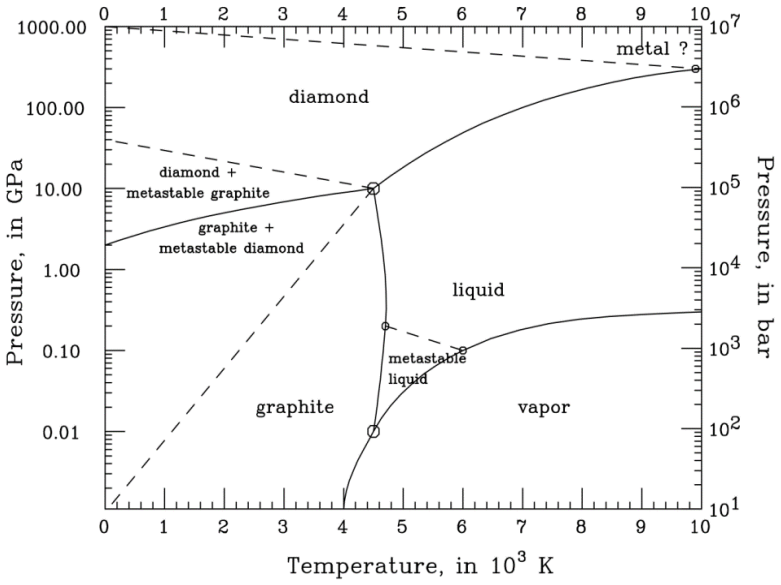

Figure 6: carbon phase diagram [42].

Figure 6 shows the carbon phase diagram. As can be observed, diamond is synthetized only at high pressures and temperatures (above 10 GPa and 2000 K). In environmental conditions graphite is stable, while diamond is "metastable", i.e. the energy needed to break its chemical bonds and turn it into graphite is too high to occur by a spontaneous process [42]. Therefore, this peculiarity allows it to be kinetically stable even at room temperature and atmospheric pressure.

Carbon is naturally found also in amorphous form or can be synthesized in the laboratory in new nanostructured artificial configurations such as fullerene, graphene and nanotubes (Figure 7).

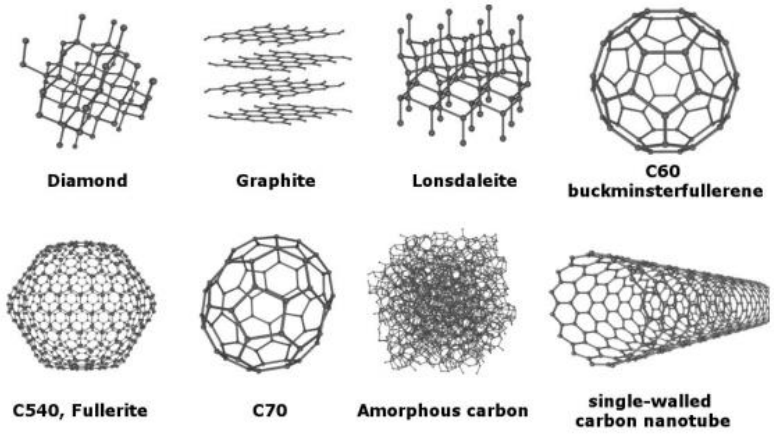

Figure 7: allotropic forms of carbon [43]

Crystalline structure of diamond (Figure 8) is organized in a cubic centered-face lattice (FCC) with base of 2 carbon atoms at positions (0; 0; 0) and (1/4; 1/4; 1/4) and a lattice constant equal to 3.57 Å. Thanks to its configuration, diamonds possesses a very high density $\rho = 3.54$ g cm^{-3}, greater than that of graphite (2.26 g cm^{-3}) [44].

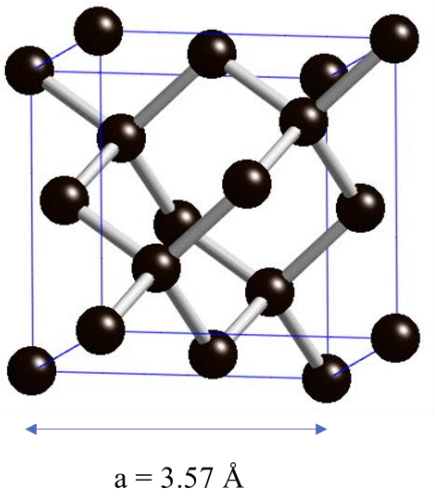

- sp^3 hybridization
- Covalent bonds
- Face-centered-cubic structure (FCC)
- Interatomic distance: 1.54 Å
- Lattice constant: 3.57 Å
- Atomic density: 1.77 10^{23} atoms cm^{-3}

Figure 8: diamond lattice cell and its characteristics [45].

Diamond presents high interatomic cohesion energy: 7.37 eV atom^{-1} (711 kJ mol^{-1}) [44]. This feature is at the basis of several extreme macroscopic properties, including:

- an extreme hardness value (10 on the Mohs scale), the maximum found in nature;
- high Young's modulus (1220 GPa);
- chemical inertia and excellent biocompatibility [36].

It is also characterized by a high thermal conductivity, around 2200 W m^{-1} K^{-1} [46]. This property derives from the fact that, at room temperature, the phonon density is relatively low compared to other crystals, thus presenting a reduced probability of interaction between the lattice vibrations themselves (higher mean free path of phonons) and resulting in a high thermal conductivity.

As observable in the band diagram reported in Figure 9, diamond has a wide indirect energy gap ($E_g = 5.47$ eV [47]). As a result, it presents high transparency from ultraviolet to far infrared, it is electrically insulating at room temperature and can accommodate a high number of defects. Noteworthy is the high refractive index: its average value in the visible spectrum is about $n = 2.42$ [48]. The resulting high reflectance, although determining a considerable interest in jewelry manufacture, represents a limit when willing to detect the radiation emitted by embedded color centers, originating from the presence of defects and impurities in the crystal lattice. The presence of such defects introduces intermediate electronic states within the energy gap that can

alter the optical properties of diamond, allowing radiative transitions (mainly in the visible range). Nowadays more than 500 different color centers are known in diamond, many of which are artificially made through ion implantation processes [46].

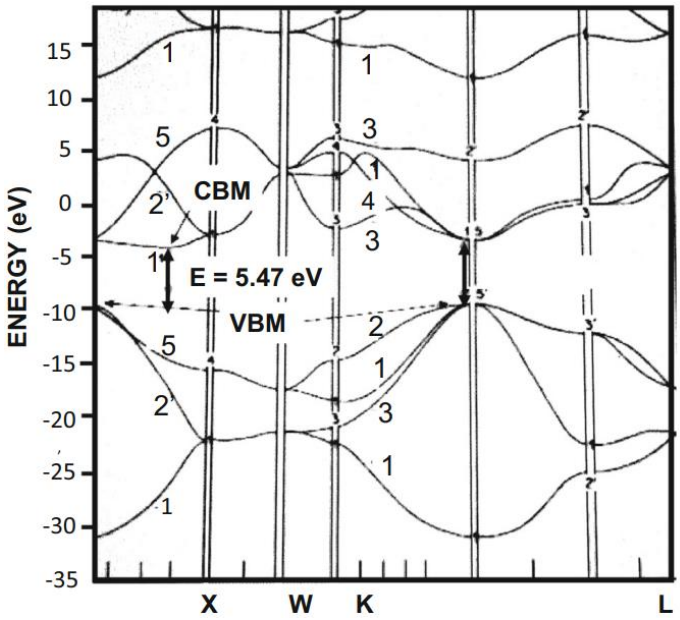

Figure 9: diamond bands diagram [47].

1.4.2 Synthesis and classification of diamond

Due to its poorly standardizable characteristics and the high cost, natural diamond is unsuitable for scientific and/or industrial applications. Therefore, in the last century artificial synthesis techniques have been developed under controlled conditions to allow systematic reproducibility.

The most widespread techniques are summarized below.

- High Pressure High Temperature (HPHT): in this process graphite is subjected to very high pressure and temperature conditions (around 10 GPa and 2000 K - 3000 K), thus determining its conversion to diamond, in the energy-favorite allotropic form of carbon [49].
- Chemical Vapor Deposition (CVD): diamond is grown through the slow deposition of atomic layers on a low-quality single-crystal diamond substrate. The process occurs in the controlled atmosphere containing hydrocarbons, typically methane, which provides the carbon atoms for the deposition, while other gases, such as nitrogen and boron, can be introduced to create specific color centers. The main advantage of this technique is the possibility of accurately controlling the concentration of impurities [50,51].

- Detonation diamonds: nanometer-sized diamond crystals can be synthesized in sealed chambers by the detonation of highly explosive carbon-containing compounds, including trinitrotoluene (TNT) and cyclotrimethyl-enetrinitramine (RDX) mixtures. Thus, the high pressures and temperatures reached on the detonation wavefront provide the conditions for the synthesis of diamond nanocrystals [52].

Depending on the degree of purity, diamond can be classified into 4 categories [44] based on the nitrogen and boron content and the absorption spectrum in the visible. In particular:

- Type Ia: high and variable nitrogen content (100-3000 ppm). Despite the high level of impurities, it has low absorption in the visible, making it widely employed for applications that take advantage of the high hardness or in jewelry. Most of natural diamonds falls in this category, while only in rare cases they can be found in the other categories.
- Type Ib: nitrogen concentration between 100-500 ppm. The light absorption window falls in the green and blue range, making it to appear yellowish. HPHT synthesized diamond typically belongs to this category.
- Type IIa: very low nitrogen concentration (less than 10 ppm), offering excellent transparency. It is rare in nature and is usually synthesized with the CVD technique. Nonetheless, also HPHT techniques can be employed [53];
- Type IIb: nitrogen concentrations even lower than type IIa. In this frame, the presence of boron impurities become relevant, providing p-type semiconductor behavior.

1.4.3 Color centers in diamond

The diamond lattice can accommodate several types of defects which can consist of:

- interstitial atoms, in the presence of additional atoms in the crystal lattice;
- substitutional atoms, when a carbon atom is replaced by different atomic species;
- vacancies, in the absence of a carbon atom from its lattice position.

These defects are naturally present in diamond or can be created by ion implantation techniques (see paragraph 1.5.2). The presence of such defects introduces additional electronic levels into the energy gap. These levels may be close to the valence and/or conduction bands, determining a semiconductor behavior, or deep, resulting in localized electronic states. The latter usually occurs in the form of a fundamental state and one or more excited states, resulting in the possibility of radiative transitions in the visible light range. In this case, the defects are named "color centers".

Color centers can be excited via an appropriate laser source with sufficient photons energy. From a quantum point of view, if the excitation energy is lower than the differences between the levels, the photons can be absorbed and re-emitted assuming the creation, starting from a photon, of a virtual state of an electron-hole pair for such a Δt time that $\Delta t \cdot \Delta E \geq \hbar/2$. Rayleigh scattering occurs when, during the existence of such virtual state, no phonons are created or destroyed. Conversely, as shown in Figure 10, if a phonon is created/destroyed, the photon re-emitted following the recombination of the electron-hole pair will have an energy lower/higher than that of excitation, resulting in the so-called Stokes/anti-Stokes Raman effect [54]. This energy shift, referred as Raman shift, is equal to the energy of the phonon exchanged and is specific to each type of lattice vibration. Thus, from this effect, structural information on the crystal can be obtained. For single-crystal diamond the energy of the phonons (and therefore also the Raman Shift) is, as expressed in wavenumber, 1332 cm^{-1} [46].

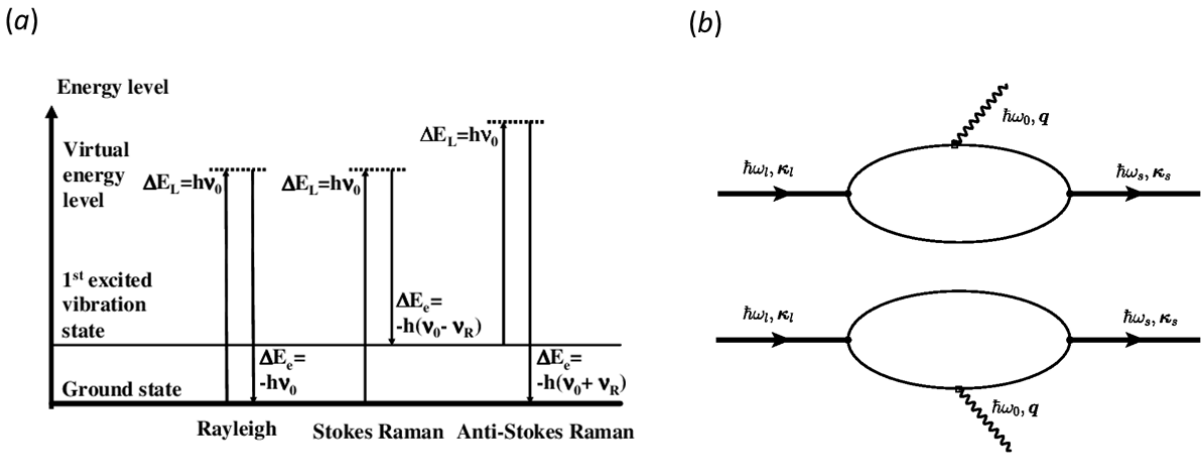

Figure 10: (a) diagram of the Raman effect [55]*; (b) Feynman diagram of Raman scattering. Rayleigh scattering occurs when, during the existence of the virtual state, no phonons are created or destroyed* [56].

Fluorescence transitions can also occur with or without coupling with the lattice vibrations of the crystal. In the first case, the interaction between electronic and phonon states during excitation or relaxation results in a characteristic emission band called "phonons replicas". In the absence of this type of interaction, a very narrow spectral emission occurs, called “zero-phonon line” (ZPL), with an energy corresponding to the energy leap of relaxation of the excited electrons.

Up to date, there is a large amount of discovered color centers in diamond (e.g.: silicon-vacancy (Si-V) [57], germanium-vacancy (Ge-V) [58], tin-vacancy (Sn-V) [59], lead-vacancy (Pb-V) [60]),

but for the purposes of this thesis, in the next paragraph the attention will be focused on the nitrogen-vacancy center (N-V).

1.4.4 Nitrogen-Vacancy center

The most well-known color center is the nitrogen-vacancy center [61]. It consists of a nitrogen substitutional atom nearby a vacancy immediately adjacent (Figure 11a). Due to its size being similar to that of carbon, the N atom fits easily into the lattice, thus representing the most common impurity in diamond crystals. The NV center occurs with two different charge states:

- NV^0: a neutral 5-electrons (spin 1/2) system, 4 of which come from the dative bonds of the carbon atoms adjacent to the vacancy and 1 from the fifth valence nitrogen electron. The photoluminescence spectrum has a ZPL at 575 nm and a wide phonon sideband at higher wavelengths (up to about 650 nm) [46];
- NV^-: unlike the NV^0 center, NV^- presents a negative charge due to the presence of a sixth electron trapped in the defect (spin 1). The ZPL is at 638 nm and the phonon band extends beyond 800 nm. The quantum efficiency of this point defect is estimated at about 0.7 [62].

Figures 11 shows the photoluminescence spectrum (a) and the level structure (b) of the two charge states of the NV center. Overall, this defect has a wide red emission spectrum from 550 to 750 nm.

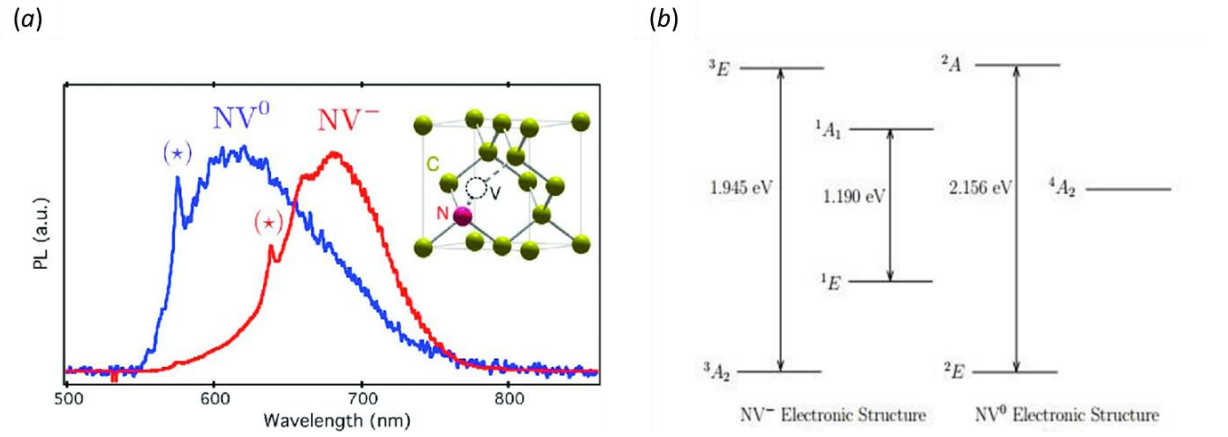

*Figure 11: (a) structure of the NV center in the diamond lattice and photoluminescence spectra of NV^- and NV^0 centers under 532 nm of laser excitation; * refer to the zero-phonon-lines* [63]. *(b) Electronic structure of NV centers.*

The concentration of nitrogen and the surface chemistry influences the position of the Fermi level and therefore the formation of one charge state with respect to the other [64] (Figure 12). In samples with low nitrogen concentration, without external influences, the Fermi level is about 2.75 eV above the valence band, so over the fundamental state of the NV^- center (at 2.0 eV), which in turn

is located above the fundamental state of the NV^0 center (at 1.2 eV). The presence of surface hydrogen terminations, providing a dipole moment that can interact with NV centers near the surface, causes the fundamental levels to bend upwards, so that the Fermi level occurs at a lower energy than that of NV^- states. This situation makes NV^0 states more likely. Since nitrogen impurities act as electron donors, as their concentration increases the Fermi level rises towards the conduction band, thus increasing the population of the level associated with the NV^- state. The effect of oxygen terminations has an opposite effect with respect to that of hydrogen, and, by bending states downwards, it realizes a situation where NV^- states are more likely. The effect of such interactions is appreciable up to about 20 nm deep, as it is inversely proportional to the square of the distance.

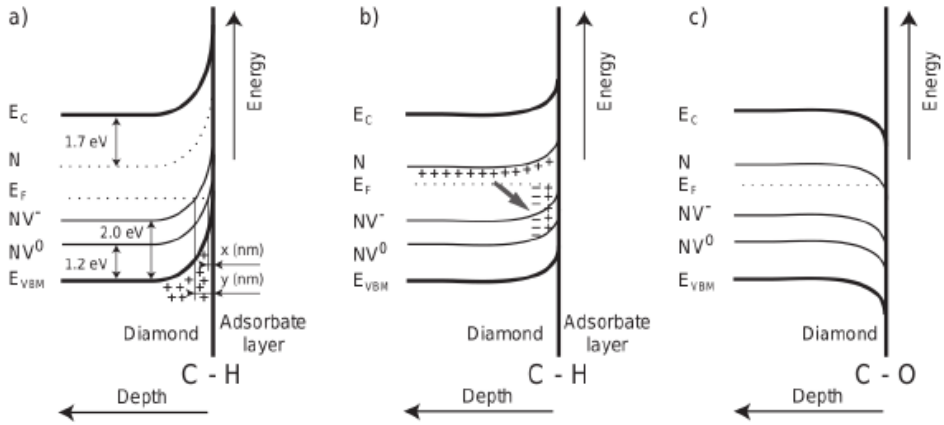

Figure 12: level structure of diamond containing NV centers, in the case (a) of low nitrogen concentration and hydrogen termination, (b) high nitrogen concentration and hydrogen termination and (c) oxygen terminations. In (a) x and y represent the depth at which the Fermi level crosses, respectively, the NV^0 and NV^- states [61].

Figure 13 shows the peculiar electronic level structure of the NV^- center. This structure can be perturbated by a magnetic field, through the Zeeman effect and thanks to the "Optically Detected Magnetic Resonance" (ODMR) technique it is possible to measure very weak electro-magnetic fields [65], and likewise interestingly, also small temperature variations [66], providing appealing perspectives also for the investigation of biological samples, with extreme spatial resolution and sensitivity [67,68]. More details concerning this technique and preliminary measurements conducted on nanodiamonds investigated during this thesis are reported in Appendix D.

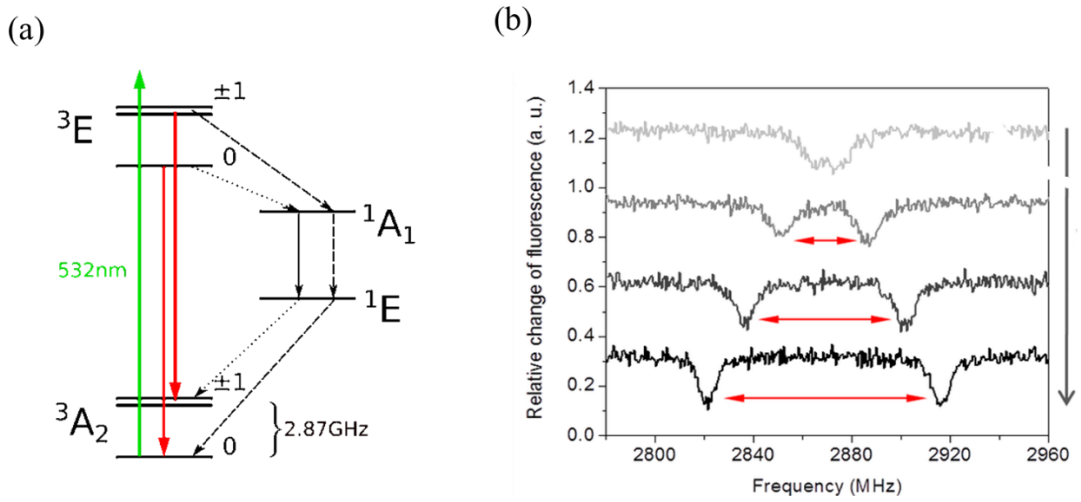

Figure 13: (a) level structure of the NV$^-$ center [69]*; (b) examples of ODMR spectra with different applied magnetic fields.* [70] *Details concerning the technique are reported in Appendix D.*

1.4.5 Nanodiamonds

Nanodiamonds sizes generally range between 5 nm and 300 nm. These nanocrystals can be synthesized with several methods, among which the main ones are:

- detonation of explosive carbon-containing compounds (TNT and RDX) [71];
- monocrystalline diamond fragmentation synthesized using HPHT method [72];
- CVD with short growth times, to control the size [73];
- laser-induced phase transition [74];

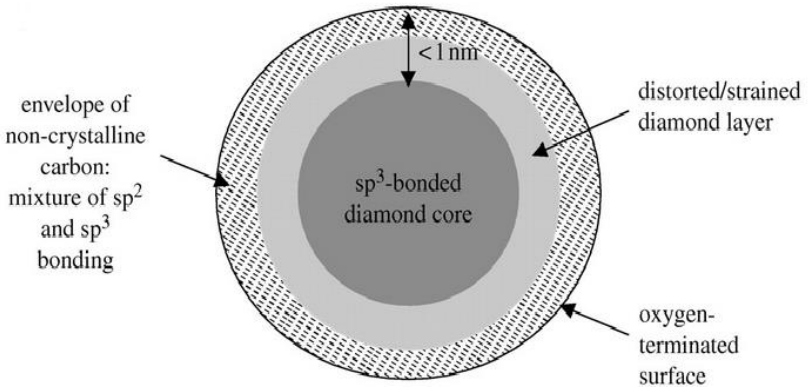

Figure 14: simplified structure of a nanodiamond [75]

As a side effect due to the stresses that occur during their synthesis process, nanodiamonds present an onion-like structure [52] (Figure 14). In particular:

- a diamond core (phase sp^3), at the basis of the luminescence properties in presence of color centers;
- a thin layer (typically up to ~1 nm) of distorted sp^3 phases and amorphous carbon;

- a non-crystalline envelope of sp^2 phases with surface termination of hydrogen and oxygen.

The photoluminescence properties of ND make them excellent candidates for tracking fluorescent biomarkers for *in-vitro* experiments [52,76–79]. Nonetheless, certain surface layers can negatively influence the optical properties of ND, since disordered and defective carbon phases have a quenching effect on the luminescence emitted by the color centers present in the diamond core [81]. Indeed, an important objective of this work will be the optimization of a processing protocol to purify ND and ameliorate their fluorescence properties.

The control of surface chemistry also plays a central role in this thesis. Surface chemical bonds or graphitic layers, in fact, are the starting substrates for functionalization with specific molecules and drugs [82–85]. Indeed, thanks to their excellent properties of biocompatibility and tunability of the surface and the small achievable sizes, in the last decade ND were proposed as interesting drug delivery systems candidates [52,86,87].

1.5 Ion-beam-based modification techniques

1.5.1 Microlithography for diamond biosensors

Ion beams can be exploited with the purpose of modifying materials with a high spatial resolution. In these techniques, accelerated ions reach energies up to several MeV according to the desired penetration depth and, once into the substrate, progressively lose their kinetic energy as a result of the interaction with electrons and nuclei. This energy loss is mainly due to Coulomb interactions with the electronic shells, as the cross section for nuclear collisions is significantly lower. The phenomenon can be described with the “electronic stopping power” formula, developed by Bethe and Bloch, which quantifies the average value of energy lost in the medium by an ion per unit of the path travelled in the matter (dE / dx). In non-relativistic approximation, the formula (eq. 1) can be simplified as follows:

$$-\frac{dE}{dx} = \frac{4n\pi Z_1^2 Z_2^2 e^4}{m_e v_1^2} \ln\left(\frac{2m_e v_1^2}{I}\right) \quad (1)$$

where Z_1 and v_1 are respectively the atomic number and the speed of the ion, Z_2 and n the atomic number and the electron density of the target material respectively, m_e the mass and e the charge of the electron and I the ionization potential.

Bethe-Bloch curves for different heavy charged particles is shown in figure 15a.

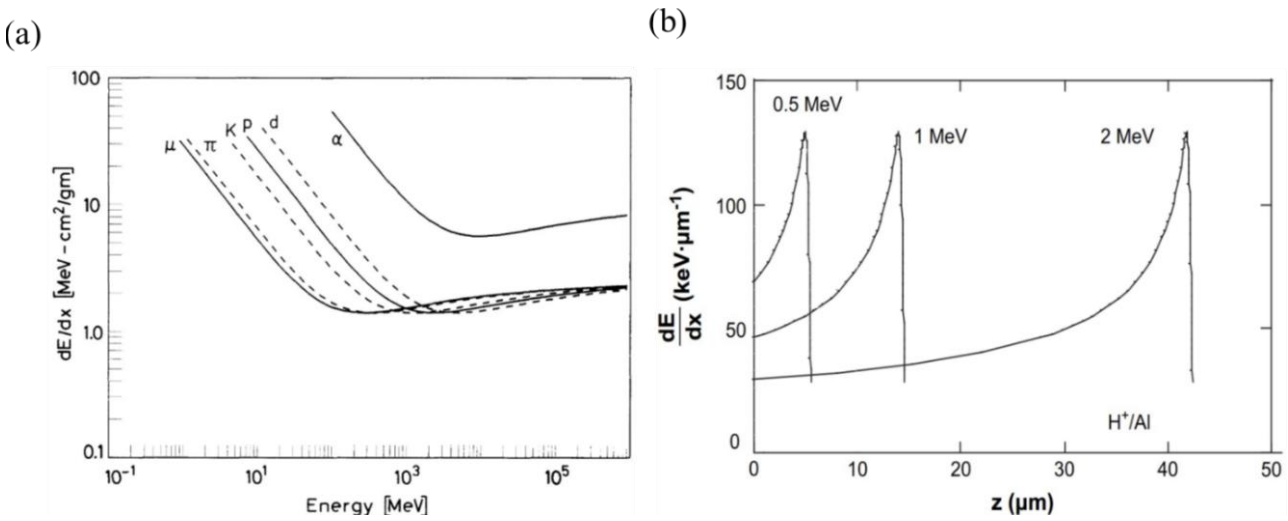

Figure 15: (a) electronic stopping power as a function of energy for different heavy charged particles [88]*; (b) Bragg curves for protons in aluminum at different energies*

As can be evinced from the graph, the energy loss is higher at lower particle velocity, as the energy loss of the particle is inversely proportional to the square of its velocity. When the electronic stopping power is plotted as a function of the ion depth inside the substrate (figure 15b), the obtained curve shows how most of the energy is deposited in correspondence of a spatially localized peak called the “Bragg peak”, whose position depends on the initial energy of the radiation.

Despite electronic collisions being the main energy loss mechanism, the collisions with the nuclei of the crystal lattice play a fundamental role in ion lithography. Indeed, the amount of energy that the ion releases during a collision with an atomic nucleus of the sample, which is typically less than 10 keV, is sufficient to induce damage in the crystalline structure of the material. This type of interaction is strongly localized and allows the creation of defects which, in the case of diamond, induces its amorphization if a critical threshold is overcome. The Monte Carlo code "SRIM" (Stopping and Range of Ions in Matter), developed by James F. Ziegler and Jochen P. Biersack in 1983 [89], allows to numerically simulate the effects of the interaction between the ions and the target material. In figure 16, a SRIM simulation of the profile describing the energy loss of the ion due to nuclear interaction in the case of He^+ ions accelerated to 2 MeV in diamond, is reported.

During nuclear collisions, if the energy of the impinging ions is higher than the displacement energy of the sample atoms (i.e.: the energy required to dislocate an atom from its lattice position), a vacancy can be created, and the undermined atom can in turn acquire further kinetic energy, possibly creating other structural defects, until it stops becoming an interstitial defect. This new

couple of defects is also named “Frenkel pair”. Oppositely, if the energy transmitted during the impact is not high enough, the atom remains in its reticular position and the energy is transferred to the crystal in the form of reticular vibrations (phonons).

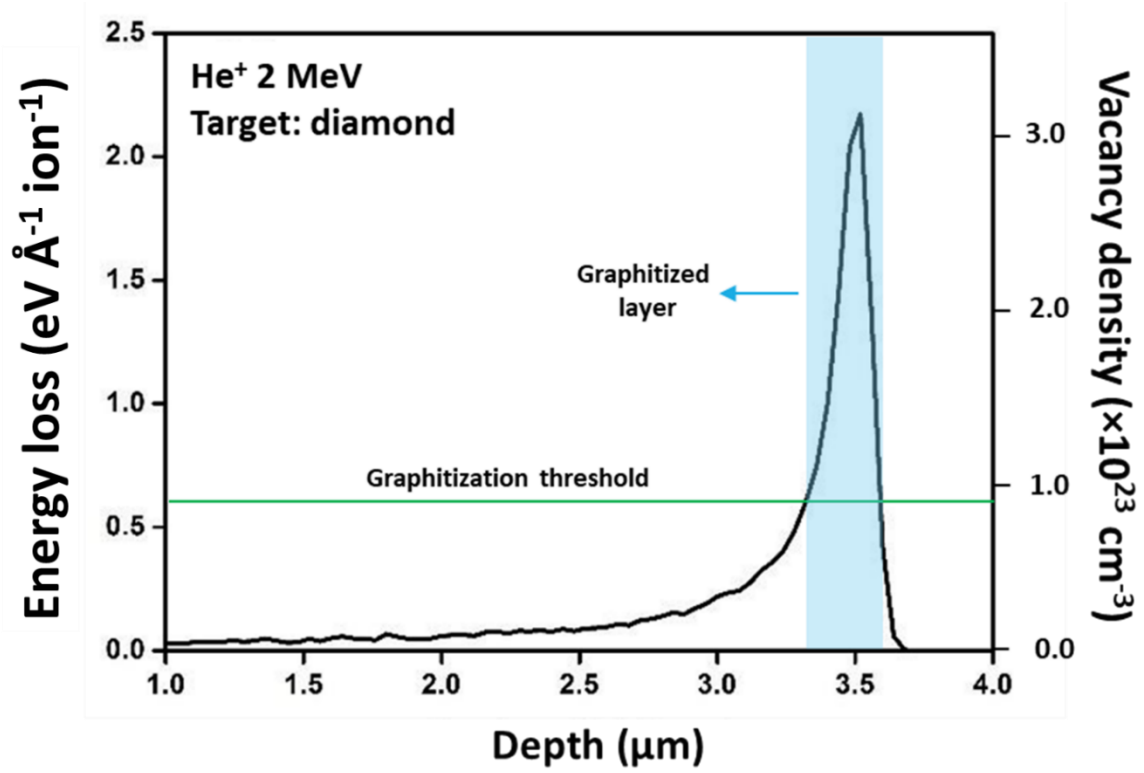

Figure 16: damage profile of 2 MeV He^+ ions in diamond, as simulated with SRIM software

The MeV Deep Ion Been Lithography (DIBL) for diamond modification takes advantage of these principles and of the metastable nature of diamond to obtain graphitic microchannels at localized depth in the sample. Indeed, if the ion fluence delivered on the substrate is enough to generate a density of defects higher than a certain threshold value, the crystalline structure collapses, transforming the diamond into amorphous carbon. This threshold, also referred to the graphitization threshold, occurs at a vacancy density ranging within 2-6 × 10^{22} vacancies cm^{-3} [90–93]. By means of a following High Temperature Thermal Annealing (HTTA) process (see section 1.6.1), the regions whose damage is above this threshold are converted to graphite. Conversely, regions implanted below this critical value are restored to a pristine diamond structure, since a large fraction of the Frenkel pair defects are recombined [94].

A previous study evidenced how the graphitization level increases with the energy of the ions and therefore as the implantation depth increases [95]. This observation can be justified by considering the increase in the internal pressure of the implanted diamond. In fact, the conversion of diamond

into graphite leads to an expansion of the material; however, this is limited by the diamond layer located above the graphitic layer, which, having a higher density, hinders this expansion process. Therefore, since greater depth reached by the ions corresponds to greater thickness of the surface diamond layer, the internal pressure due to the expansion will determine an increase in the critical density value of the damage. The mechanical deformation effect is called swelling and reflects the dynamics underlying the damage to the crystal, which depends on the type of implanted ions, their fluence, the post-implantation heat treatment temperature and the generation of local mechanical stresses. By measuring these deformations, it has been possible to obtain an in-depth study of the phenomenon, with the aim of determining the graphitization threshold. The results published by F. Bosia et al. [96] were obtained from the combination of SRIM simulations with finite element (FEM) simulations, with the aim of modeling the effects of ion implantation, such as internal stresses and the evolution of the structural properties of the diamond following the heat treatment. Thanks to DIBL, graphitic channels with micrometric resolution can be realized in diamond substrates [40,41]. With this technique, over the years the solid-state physics group of the University of Torino, managed to realize diamond-based biosensors which exploit these conductive microchannels to measure electrochemical signals from cells (mostly neurons) directly cultured on the sensor. These sensors are fabricated starting from a monocrystalline CVD diamond. He^+ beams with few MeV of energy are generally employed. Microchannels geometry has been developed into two versions, with sixteen or sixty graphitic microelectrodes converging in a central region (Figure 17).

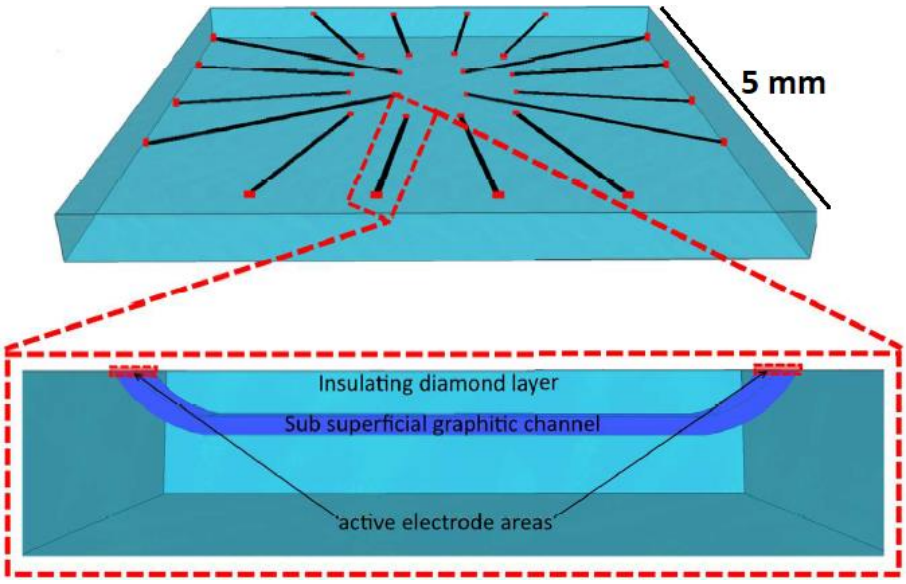

Figure 17: model of a diamond-based biosensor with embedded graphitic microchannels

The microchannels have an average length of 2 mm, width of 20 μm and a depth of 2 μm. Their thickness depends on the width of the Bragg peak of the beam used during the implantation, which is generally between 200-500 nm. To allow the functioning of the biosensor, the exposure of the graphitic channels to the surface is required both in correspondence of the central region, for cells-electrodes contact, and of the peripheral regions, for the bonding with front-end electronics. Previous modification processes developed by the solid-state physics group and published in [97,98], solved this problem by gradually reducing the penetration depth of the ions by means of a metal mask with a variable thickness profile directly applied on the sample surface, thus tuning the energy of the ions impinging on the diamond substrate. The developed biosensors are meant to detect neuronal cell culture signals, in particular action potentials and neurotransmitters release upon exocytosis (e.g.: dopamine). To allow a better adhesion of cells on the biosensor, the diamond surface is generally coated with a poly-L-Lysine (0.1 mg ml^{-1}).

Devices based on different materials to measure these signals are already present on the market, such as carbon fiber microelectrodes (CFE) to perform amperometric measurements of the exocytosis [99], or potentiometric multi-electrodes arrays (MEA) to detect neuronal action potentials. Only a few prototypes have been developed so far to perform both kinds of detections simultaneously from the same cellular network [37], but an optimal and easy-to-use device to this scope is not yet available, and with this scope, the research group is working on a diamond biosensor capable of it. In this frame, over the past years, a strong collaboration has been established with the neuroscience division of the Department of Drug Science and Technology of the University of Torino in order to test the sensors, leading to several publications [97,98,100,101].

1.5.2 NV centers fabrication

NV centers can be already present both in natural and artificial diamond. Nonetheless, their concentration can be increased by means of ion-beam-based techniques. If the starting sample contains few nitrogen impurities, these can be introduced by the implantation of nitrogen ions [102]. Nanodiamonds used in this thesis are classified as type Ib, with a nitrogen content between 100-200 ppm. Therefore, in this case, a simple creation of new vacancies is sufficient to create a relevant amount of NV centers.

Different damaging techniques can be employed to create vacancies, such as electron [103], neutron [104] and ion irradiations [105]. This work will be focused on the latter technique, by using H^+ beams with energies of the order of MeV, exploiting the inelastic interaction of accelerated protons with the nuclei of the sample atoms [106]. This process can be simulated using SRIM to determine the expected value of relevant parameters such as the depth of penetration of the ions,

lateral and longitudinal dispersion, the created vacancy density and the energy loss due to the interactions with electrons and nuclei. Oppositely, once selected the desired vacancy density, it is possible to derive the ion irradiation parameters to be implemented. According to previous studies reported in literature, the optimal displacement energy is of 50 eV [107]. Since vacancies are produced randomly in the implanted volume, post-implantation annealing must be carried out in order to pair them with the nitrogen impurities present (thermodynamically favored situation) and activate the new NV (see paragraph 1.6.1).

The manufacture of new NV centers in nanodiamonds to intensify their luminescence is a central aspect of the thesis and the experimental procedure will be discussed in detail in 3.2.4.

1.6 Bulk and surface thermal modification

Structural and surface modifications of diamond can be performed with a wide variety of thermal or chemical processes according to the desired result. This thesis work will be mainly focused on thermal modification.

1.6.1 High Temperature Thermal Annealing

High Temperature Thermal Annealing (HTTA) (Figure 18) is a thermal process (about 800 °C or more) in an inert atmosphere (vacuum or argon/nitrogen flow) that has multiple objectives:

- the graphitization of any amorphous carbon phases. This is true both for diamond bulk and nanocrystals. No transition takes place for the diamond phase, whose conversion into graphite requires temperatures above 1100-1200 °C [108]; this process is commonly used after ion-beam-based microlithography to induce the phase transition of the amorphous damaged areas. As already mentioned, this conversion is to graphite only when the graphitization threshold, is reached, while regions implanted below this critical value are restored to a pristine diamond structure.
- the activation of color centers. Indeed, after ion implantation, ions are found in interstitial or substitutional positions of a highly damaged lattice. The HTTA restore the crystal structure and mobilizes the defects. More precisely, the color center formation relies on the thermal diffusion of the native or ion-induced vacancies. In the case of interest for this thesis, when the ion irradiation randomly creates new vacancy defects, during HTTA these are allowed to migrate and couple with the nitrogen impurities already present in Ib type diamond, thus forming new NV centers [105,108,109].

- surface chemical reduction: the vacuum or inert environment during HTTA causes a chemical reduction of the ND surface, thus removing most of oxygen-containing groups [110].

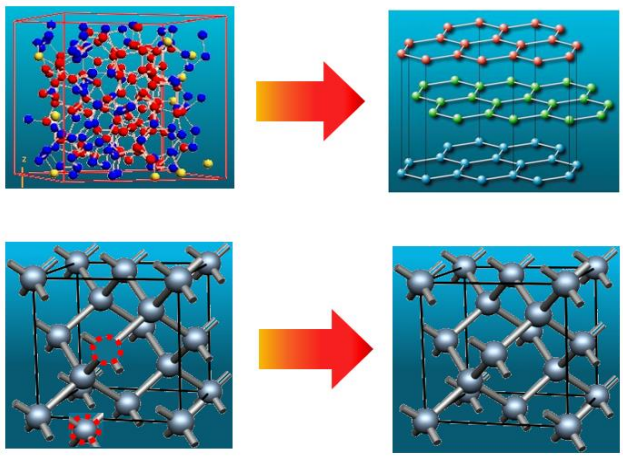

Figure 18: effects of annealing treatment on diamond. On the one hand it allows the graphitization of amorphous carbon components, while on the other it allows rearranging the crystal by migrating the vacancies next to nitrogen impurities.

1.6.2 Thermal oxidation and hydrogenation

Untreated nanodiamonds do not typically possess high luminescence and are contaminated by a pronounced sp^2 component on the surface. Thermal treatments aimed at improving these characteristics are predominantly oxidative [111–114]. These processes are usually carried out at temperatures between 400-550 °C in oxidizing atmosphere (air or oxygen flow). Oxygen exposure at such temperatures results in a progressive removal of surface graphitic layers, thus decreasing the shielding and quenching effect on the luminescence produced in the diamond core [81,111,115] (Figure 19a).

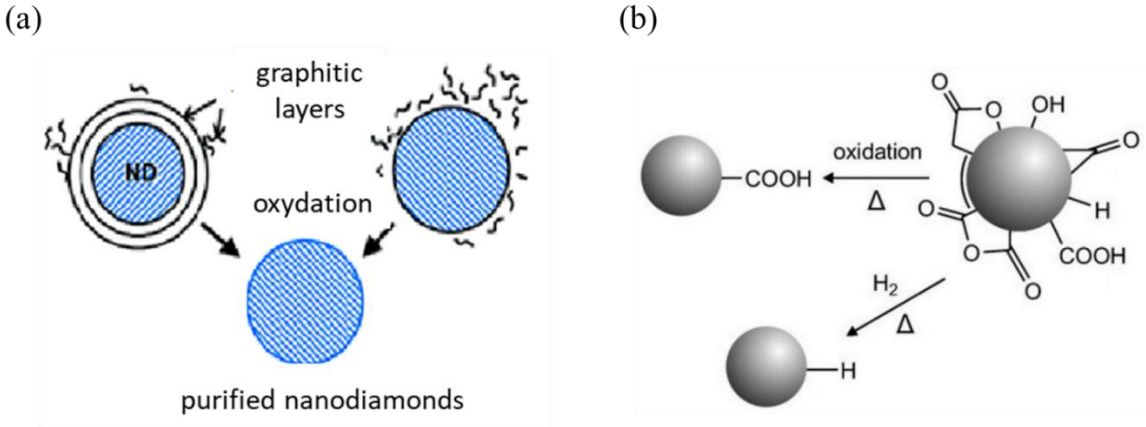

Figure 19: Effects of thermal processes on nanodiamonds. (a) removal effect of surface graphitic phases by oxidation [111]*; (b) surface termination following oxidation or hydrogenation* [116].

In parallel, following this treatment, many oxygen-containing groups (mainly carboxyl and carbonyl) are formed on the surface, which in turn can represent the substrate for further chemical functionalization (Figure 19b).

Hydrogenation of diamond surface can also be achieved through a thermal process in hydrogen-containing atmosphere. Interestingly, since hydrogen electronegativity is lower than that of carbon ($X_H = 2.20$, $X_C = 2.50$) [117], the C-H bond is polarized with a positive charge δ^+ on the H atom. Hence, the dipole moment component of the C-H bonds perpendicular to the surface is positive, resulting in negative electron affinity of H-diamond surface (χ = -1.3 eV) [118,119]. In contrast, oxygen terminations increase diamond electron affinity (with a positive value of +1.7 eV), due to the high electronegativity of O ($X_O = 3.44$).

Hydrogen terminations also considerably decrease ionization energy, defined as the difference between E_{vac} and the top of the valence band (E_v), to 4.2 eV (Figure 20). Consequently, hydrogenated diamond can transfer electrons from E_v to physiosorbed surface adsorbates, particularly water, provided that their electron affinity exceeds this value. The phenomenon results in the formation of a subsurface accumulation of holes, which determines a significant surface conductivity [119].

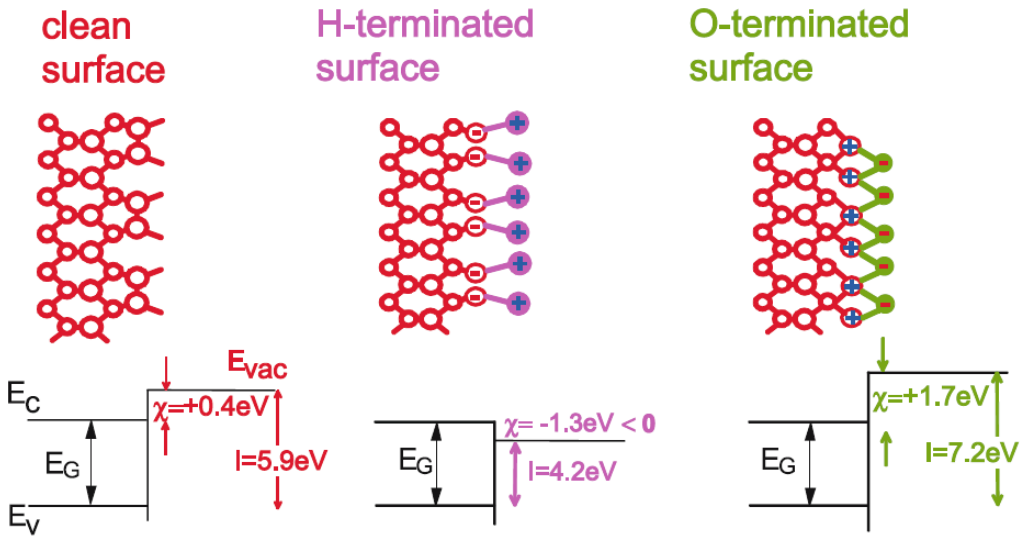

Figure 20: Scheme of the modification of electron affinity and ionization energy of diamond surfaces by hydrogen and oxygen terminations and band diagrams for the clean and the fully H/O-terminated diamond surfaces [119].

When a thin water layer formed over H-terminated diamond surfaces, it behaves as an electron acceptor system, leaving holes on the diamond surface which acts as mobile charge carriers, thus allowing conduction to occur [120]. Electron exchange from diamond to the water layer is driven by the difference in the chemical potential of electrons in the liquid phase (μ_e) and in diamond

(Fermi level, E_F) and causes the reduction of hydroxonium ions to H_2 and H_2O. Electron transfer is regulated by the following redox reaction:

$$2H_3O^+ + 2e^- \leftrightarrow 2H_2O + H_2$$

and continues as long as μ_e is below E_F, until an equilibrium is reached (Figure 21).

It is worthwhile noting that the high conductivity of hydrogenated diamond is not peculiar to hydrogenation itself, but it requires the presence of the above-mentioned water layer.

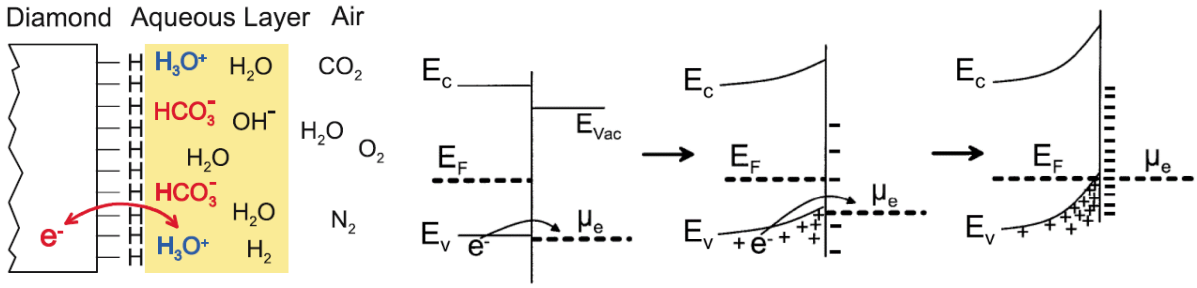

Figure 21: surface charge transfer of hydrogenated diamond surfaces with adsorbed water [119,120]. *The consequent charge separation keeps the so-formed holes near the surface, confined by an upward band bending potential.*

The low surface sheet resistance of hydrogenated diamond films (10^4-10^6 Ω/□) disappears after samples oxidation (>10^{10} Ω) [120].

Hydrophilicity is also strongly correlated with the surface termination of diamond. Hydrogenated diamond is hydrophobic, while oxidized surfaces display good hydrophilicity [121]. Previous experiments of water wettability of CVD diamond films by means of contact angle measurements showed a higher contact angle of water for hydrogenated with respect to oxidized samples. Indeed, the dipole momentum related to C-H heteropolar bond is lower than the one associated with C-O bond, hence reducing the interaction with water molecules [121–123].

Similarly, with bulk diamond, the above-mentioned properties are transferable to nanodiamonds. In hydrogenated nanodiamonds (H-ND), indeed, the negative electron affinity promotes electron emission under irradiation [117,118,123]. For this reason, H-ND are of increasing interest in the context of radiotherapy, since they can act as sources of ROS in addition to those generated by ionizing radiation, thus enhancing the biological damage and the therapeutic effects on cancer cells [124–126]. The electrical properties of 5 nm detonation H-ND have been already investigated in a previous work [127] by means of current-voltage characteristics, with ND packed in a glass cylinder. The results showed an evident decrease in resistivity from 10^7 Ω cm to 10^5 Ω cm following

hydrogenation between 600 °C – 900 °C (sp^2 phases were not affecting this result, since no graphitization was observed). In light of this consideration, a legitimate doubt may arise considering that in bulk diamond this conduction is due to the accumulation of holes below the surface, but the model does not provide an explanation for the conduction between adjacent ND.
Although oxidized diamond does not show this effect, the hydrophilic behaviour favours the interaction with water and its surface adsorption. The latter phenomenon is even more remarkable for ND powders, as it affects their electrical properties. Indeed, even if for oxidized ND no transfer-doping mechanism to allow conduction is possible, adsorbed water molecules allow charge mobility through the Grotthuss mechanism. This phenomenon consists of the hopping of a proton from a hydroxonium ion (H_3O^+) to a proximal water molecule. This implies the formation of a new H_3O^+ ion. The process is repeated in a chain, through the reaction:

$$H_3O^+ + H_2O \rightarrow H_2O + H_3O^+$$

This conduction effect rises further with higher amounts of adsorbed water [128], while it substantially drops upon heating ND in vacuum, since the treatment causes the removal of adsorbed water [129].

1.7 Finalities of the work

The first part of this thesis is dedicated to the characterization of monocrystalline diamond samples modified by means of ion-beam-based techniques to create graphitic conductive structures. The activity of the candidate has been mainly focused on the Raman and the electrical characterization of the graphitic structures, whose results were published in [101,130].
The second part is focused on the preliminary processing and characterization of nanodiamonds for many of the applications mentioned in this introductive chapter. In particular:

- thermal modification, purification and proton irradiation to enhance the fluorescence yield;
- thermal modification to tune the surface chemistry, hydrophilicity and electrical conductivity.

As underlined in the previous sections, each modification process offers specific physical and chemical properties whose in-depth characterization was carried out by combining multiple measurement techniques, such as Raman spectroscopy to identify the content of sp^3 and sp^2 carbon, photoluminescence spectroscopy to measure the emission spectra of luminescent defects embedded

in nanodiamonds, DRIFT infrared spectroscopy to recognize surface chemical species, SEM / TEM microscopy to analyze the morphology and the Dynamic Light Scattering technique to evaluate the dispersibility of the nanoparticles in solution.

Taking advantage of the results gradually obtained during the PhD course, a solid collaboration was established with the research group of Prof. Alessandro Barge of the Department of Drug Science and Technology to functionalize the surface of the processed nanodiamonds with biomolecules of potential interest for diagnostic and therapeutic applications. Furthermore, in the last year, another collaboration was established with the group of Prof. Gallicchio of the Department of Drug Science and Technology, with the purpose of testing the modified nanodiamonds samples for optical tracking applications in cell cultures.

2 Experimental set-up

This chapter is dedicated to the description of the instrumentation employed for the modification and the characterization of the samples.

2.1 Thermal treatment furnace

A ThermoConcept ROT 60/300/12 tubular oven (figure 22) was employed for thermal treatments of nanodiamonds. The maximum achievable temperature is 1200 ° C, with a power of 3 kW. The control system allows the programming of treatment ramps according to the desired process protocol. Samples are loaded inside the tube in an inert alumina crucible.

Figure 22: tubular thermal furnace ThermoConcept ROT 60/300/12

For HTTA treatments, a continuous laminar flow of inert gas (Ar or N_2 supplied by gas cylinders) is established inside the tube. Hydrogenation is performed by injecting H_2 produced with water electrolysis with a "Parker Domnick Hunter 60H" Hydrogen Generator, which guarantees a gas purity > 99.999% and 0-7 bar output pressure. The gas flow is controlled by a "Key Instruments" flowmeter, ranging between 0.1-0.4 l min^{-1}.

Oxidation processes are performed by leaving open the tube sides for the entire duration of the treatment so that the samples are exposed to the oxygen contained in the air (oxidizing atmosphere).

2.2 Ion accelerator

Ion beam-based modification of diamond was performed mainly for the creation of NV centers in nanodiamonds. Irradiation with protons with energies of the order of a few MeV was obtained by

using the AN2000 accelerator (Figure 23) located at the Legnaro National Laboratories (INFN). This facility consists of a Van der Graaf type electrostatic accelerator with a single loading stage and a maximum terminal voltage of 2 MV. Besides protons, also monovalent helium ions (He^+) can be accelerated, which were employed to create graphitic channels in bulk diamond samples to realize the biosensors mentioned in the introduction.

The treatment chamber is equipped with a maneuverable sample holder, which allows movements with micrometric precision along with all three directions. Furthermore, rotations with a step of 1° are feasible, allowing an inclination of the sample with respect to the direction of the beam. The spot diameter ranges from a few hundred of µm up to about 5 mm.

Asides from the mentioned activities, the facility is employed every year by about 30 international research groups, for a total amount of machine time equal to 2500 hours per year. The main experiments carried out concern the microfabrication by ion beam lithography, elemental characterization with nuclear physics techniques, ion channeling, Elastic Recoil Detection Analysis (ERDA), X-ray emission induced by protons (PIXE) on semiconductors, ceramics and glass materials, environmental samples and marine aerosols.

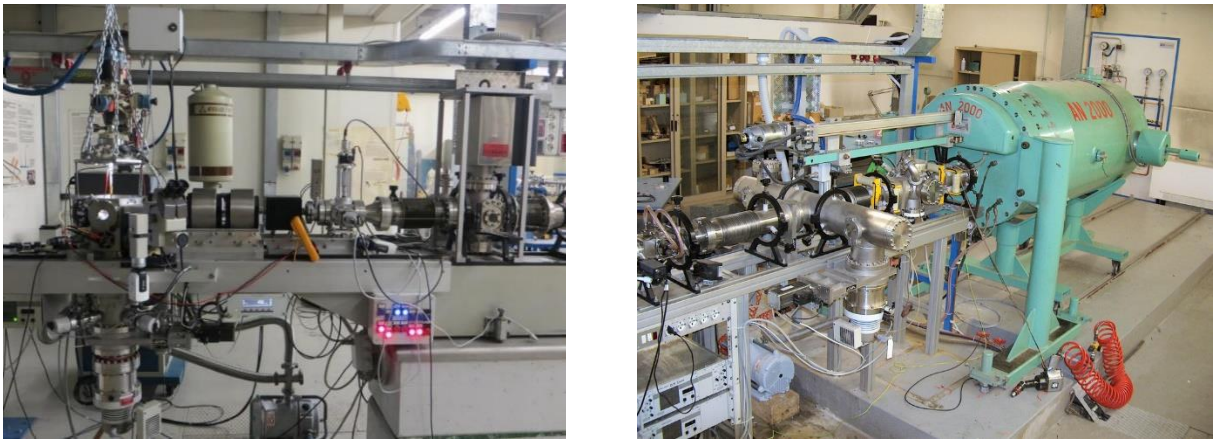

Figure 23: AN2000 accelerator, INFN laboratories – Legnaro (PD), Italy

2.3 Electron Microscopy (SEM/TEM)

Electron microscopy allows to obtain images with nanometric resolution by using electron beam probes. It is therefore ideal for observing the morphology and estimating the dimensions of the nanoparticles and nanostructures.

SEM characterization was assessed with “FEI - Inspect FTM” (Figure 24a), available at Nanofacility Piemonte (INRiM). The instrument is equipped with a Field Emission Gun (FEG)

source and works in high vacuum (about 10^{-6} mbar). For the acquisition of nanodiamonds micrographs, a low accelerating voltage (5 kV) was set in order to reduce charge effects and better investigating the surface morphology, allowing for ~ 10 nm spatial resolution. The imaged samples were prepared by dispersing the ND in isopropyl alcohol, with a concentration of ~0.1 mg ml^{-1}. The solutions were then sonicated with Elmasonic S15H (35W ultrasonic power) and finally deposited and dried over a silicon substrate.

TEM images were acquired with a JEOL 3010 UHR TEM microscope (Centro dell'Innovazione, University of Torino, Figure 24b), operating at an acceleration voltage of 300 kV and allowing to reach a resolution of 0.17 nm. Samples were prepared by depositing the same solutions employed for the SEM specimen preparation over a lacey-carbon copper grid.

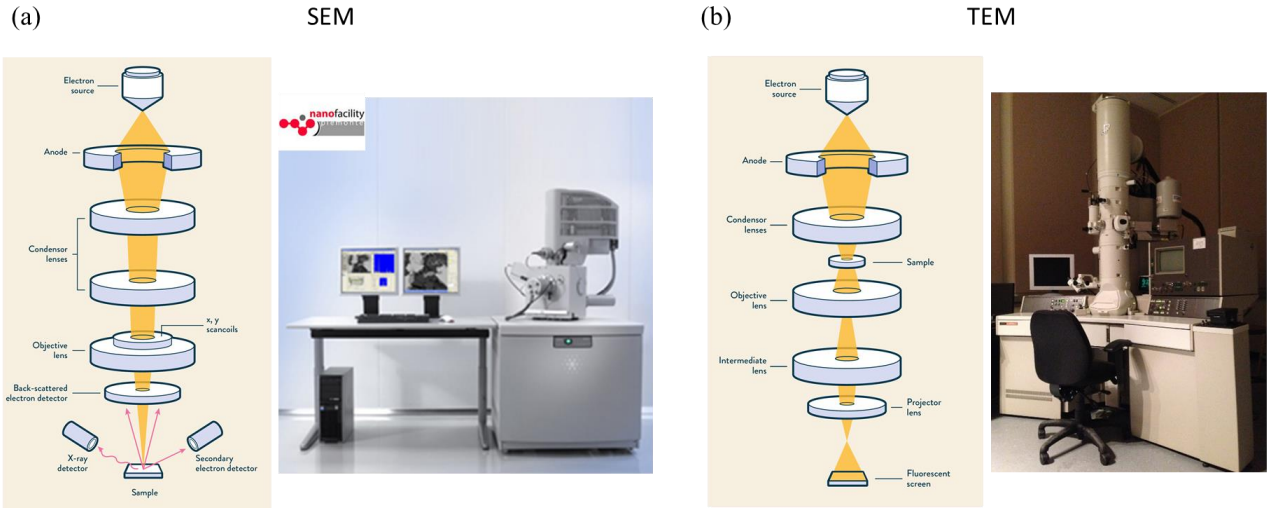

Figure 24: (a) Inspect F^{TM} SEM; (b) JEOL 3010 UHR TEM

2.4 Dynamic Light Scattering (DLS)

Dynamic Light Scattering, or DLS, is a characterization technique for measuring the size of nanoparticles and molecules in aqueous environment. The working principle exploits the Brownian motion: the nanoparticles in solution, in fact, are constantly in motion due to the thermal agitation of the liquid, with a velocity inversely proportional to their mass and, therefore, to their size. In short, the technique consists in investing with a large laser beam a vial containing the solution. After interacting with the nanoparticles, the scattered light undergoes destructive and / or constructive interference and is finally revealed by an Avalanche Photodiode Detector (APD). The detected "speckle pattern" is then processed evaluating the variation of the scattering intensity over

time. Faster variations are due to the passage of smaller nanoparticles and vice versa for slower variations (Figure 25a).

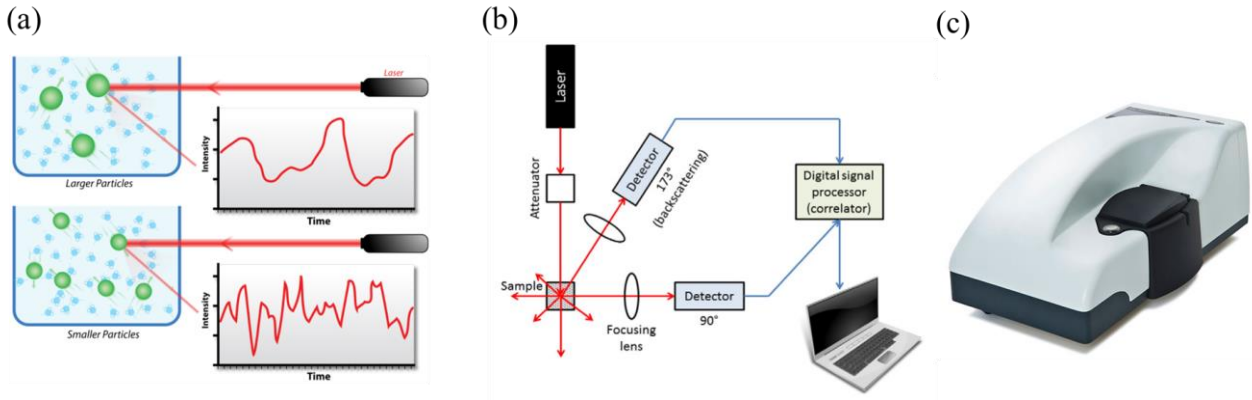

Figure 25: (a) exemplary schematic of the variation of the intensity signal over time due to the motion of the nanoparticles in solution [131]*; (b) schematic of a DLS measurement set-up; (c) Zetasizer Nano ZS.*

The distribution of sample sizes is generated starting from an autocorrelation function (eq. 2), given by:

$$g^2(q;\tau) = \frac{\langle I(t)I(t+\tau)\rangle}{\langle I(t)\rangle^2} \qquad (2)$$

where I is the measured intensity, t the time and τ delay time. Function g^2 measures the correlation between the time difference signals τ. As τ increases, the correlation decreases, since over time the signals are increasingly independent of each other. The speed with which the autocorrelation function decays (Γ) is linked to the diffusion coefficient of the nanoparticles (D), through the relationship $\Gamma = Dq^2$, where $q = \frac{\frac{4n}{\lambda_0} sen\theta}{2}$ (with n the refractive index of the solution, λ_0 the excitation wavelength of the laser and θ the scattering angle). Finally, the Stokes - Einstein equation (eq. 3) correlates the diffusion coefficient with the hydrodynamic diameter of the nanoparticles in solution (d_H):

$$d_H = \frac{kT}{3\pi\eta D} \qquad (3)$$

where k is the Boltzmann constant, T the temperature and η the viscosity of the solvent.

The instrument employed for the DLS measurements is the Zetasizer Nano ZS (Figure 25b), which presents a measurable size range (average diameter) between 0.3 nm and 10 µm, with particle

concentration ranging from 0.1 ppm up to 40% w / v. The light source is provided by a He-Ne 633 nm laser with 4 mW power.

DLS technique is particularly indicated to assess the level of aggregation of nanoparticles in solution, which is generally detrimental as it determines a reduction in the surface area available for chemical functionalization, as well as difficulties in cellular uptake. To obtain information about this issue, the same instrument can be employed also in Zeta Potential mode. This measure is related to the surface charge of NP which determines their behaviour in colloidal suspensions and depends both on the surface chemistry of the NP and the liquid in which they are dispersed. The main phenomena occurring in this condition include ionization of surface groups present on the NP and the adsorption on the NP of charged species from the liquid. Once a net surface charge is formed, oppositely charged ions present in the solution tends to accumulate near the surface of NP, thus originating the so-called *electrical double layer*. The latter is constituted by an inner layer of ions strongly bound to the surface of the NP, referred as Stern layer, and an outer layer of ions mildly bound, called *diffuse layer*. The electrostatic potential established between the external surface of the double layer (slipping plane) and the surface of the nanoparticle (Figure 26) is defined as the Zeta Potential (ZP, ζ).

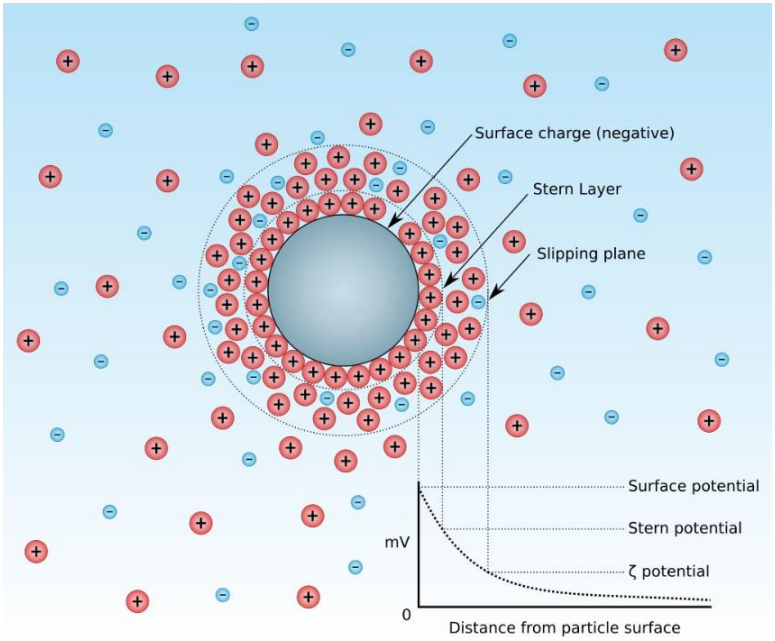

Figure 26: illustration of charge distributions around nanoparticles in solutions and of the related established electric potential as a function of the distance from the particle surface [132].

Greater negative or positive ZP corresponds to a higher level of repulsion between NP, thus reducing aggregation. Indeed, NP with |ZP| higher than 30 mV typically present a high degree of stability. Conversely, lower |ZP| values induce aggregation or flocculation phenomena due to Van der Waals interactions between the NP.

Zeta potential is usually determined by using a capillary cell with two electrodes at the ends (Figure 27). By applying an electric field to the electrodes, the charged NP acquire a net average velocity. The ratio between this velocity and the electrical field corresponds to the electrophoretic mobility (U_E), which is linked to the ZP via the Henry equation [133]. The Zetasizer Nano ZS employed in this thesis determines U_E by combining the laser Doppler anemometry (LDA) and phase analysis light scattering (PALS). In short, the measure of the frequency shift between the incident laser beam and the light scattered by the moving particles, which is proportional to the NP velocity (v), allows the evaluation of the electrophoretic mobility and, eventually, the ZP [134,135]

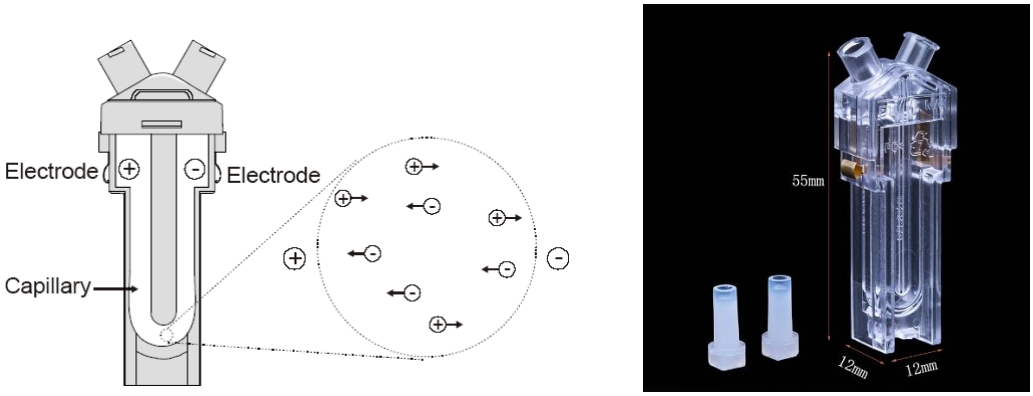

Figure 27: DTS1070 cell employed in ZP measurements.

2.5 Raman spectroscopy

As described in paragraph 1.4.3, Raman spectroscopy allows the identification of the vibrations associated with specific phases present in the sample, as well as the evaluation of its photoluminescence properties. The instrument used for this work is the Raman spectrometer available at the Scansetti Interdepartmental Center of the University of Turin (Figure 28). The instrument is equipped with a solid-state Nd: YAG laser with $\lambda = 532$ nm as excitation source. The spectra are collected with a Horiba JobinYvon HR800 spectrometer with a 600 mm^{-1} and 1800 mm^{-1} diffraction grating, which allows for a resolution of ~ 1 cm^{-1} in Raman Shift. The individual wavelengths are then collected by a CCD detector (cooled by a Peltier cell at - 70 ° C), thus evaluating their intensity. An Olympus BX41 optical microscope coupled with a color video camera allows the observation of the samples at 10 ×, 20 ×, 50 × and 100 × magnifications and to

focus the laser on the desired point and focal plane. The same optical system collects the light emitted by the sample and transfers it to the spectrometer.

The output laser power is 80 mW, but the effective power incident on the sample depends on the objective, with the possibility of further attenuations by applying proper filters. Appendix E shows a calibrated reference table of the actual laser power incident on the analyzed sample, depending on the applied objective and filter.

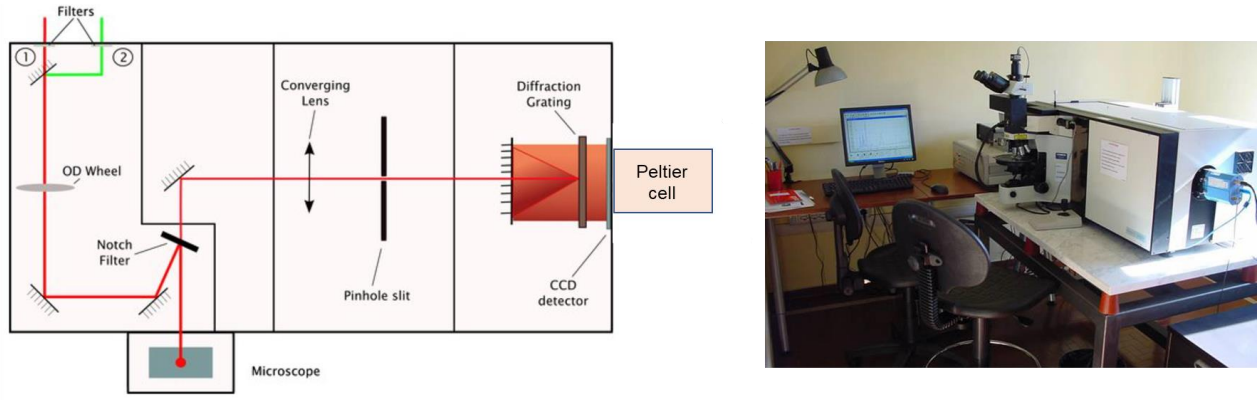

Figure 28: Raman spectrometer Horiba JobinYvon HR800 (Centro Scansetti, University of Torino)

2.6 DRIFT spectroscopy

By means of Diffuse Reflectance Infrared Fourier-Transform (DRIFT) spectroscopy, a sample is invested with a polychromatic infrared light, which excites the roto-vibrational modes of the chemical bonds present on the surface. Each type of chemical bond absorbs the applied radiation at a specific wavelength. Therefore, by evaluating the spectrum of the diffused radiation, it is possible to identify the presence of specific molecules and surface functional groups. As schematized in Figure 29a, the infrared radiation can be reflected directly from the surface of the sample ("normal specular radiation") or can penetrate inside it originating multiple reflections between the surfaces of the individual particles that compose it ("diffuse specular reflection"). In the latter situation, the signal emerges from the sample isotopically with respect to the incident beam.

In the context of this thesis, a Bruker Equinox 55 (Department of Chemistry, University of Torino), equipped with a Spectra tech DRIFT accessory (model 0030-011), was employed for the surface chemical characterization of nanodiamonds. As shown in Figure 29b, by means of a series of mirrors, the infrared light is conveyed on the sample. A second mirror system transfers both normal

and scattered specular radiation to an MCT detector (HgCdTe) operating at low temperatures (liquid nitrogen cooling) in the mid-infrared region from 400 cm^{-1} to 4000 cm^{-1}. Moreover, this setup allows the acquisition of spectra in a controlled atmosphere or under vacuum (i.e., residual pressure < 10^{-3} mbar), at a variable temperature (from room temperature up to 400 °C).
Spectra were acquired with a resolution of 2 cm^{-1} averaged over 64 interferograms. Reflectance data reported in this thesis have been converted in pseudo-absorbance: A = - log R, where R is the measured reflectance.

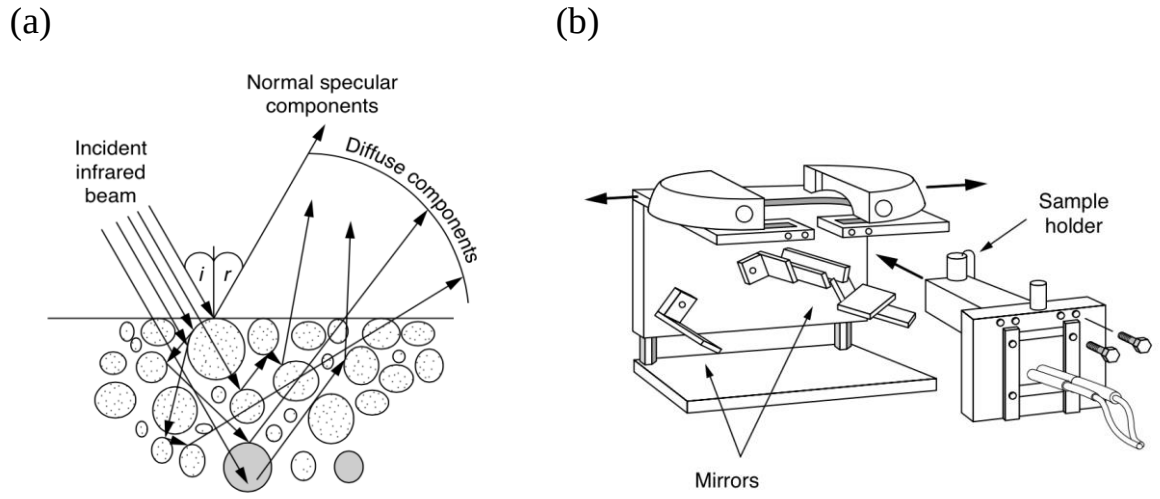

Figure 29: (a) diffusion of radiation by a powdered sample; (b) scheme of the internal construction of the interferometer.

2.7 Electrical characterization

Nanodiamonds current-voltage characteristics were acquired to assess the effects of thermal treatments on ND in terms of their electrical conduction properties. To this scope, ND powders were loaded into a polyamide cylindrical measurement chamber (depth t = (2.85 ± 0.05) mm and diameter d = (7.00 ± 0.05) mm) and closed with two aluminum electrodes (Figure 30a). Two springs coupled with plastic disks, ensured the sealing of the cell and the contact of the electrodes with the powder under uniform pressure. A Keithley 6487 picoammeter/voltage source (Figure 30b), communicating with a computer through a LabVIEW system, was employed to measure I-V curves. The measure range was set between -20 V/+20 V, with steps of 1 V. The instrument has an output impedance <100 Ω and is designed to measure resistances ranging from 50 Ω up to 1×10^{12} Ω. Finally, the resistance (R) values were calculated for each cell to compare the electrical conduction properties of the different specimens.

The same instrument has been used for the electrical characterization of the graphitic microelectrodes of the diamond biosensor introduced in section 1.5.1, by applying at their ends two microtips electrically connected to the instrument and controlled by two manipulators (30c). To ensure a proper electrical contact, the ends of the channels were covered with small drops of conductive silver paste.

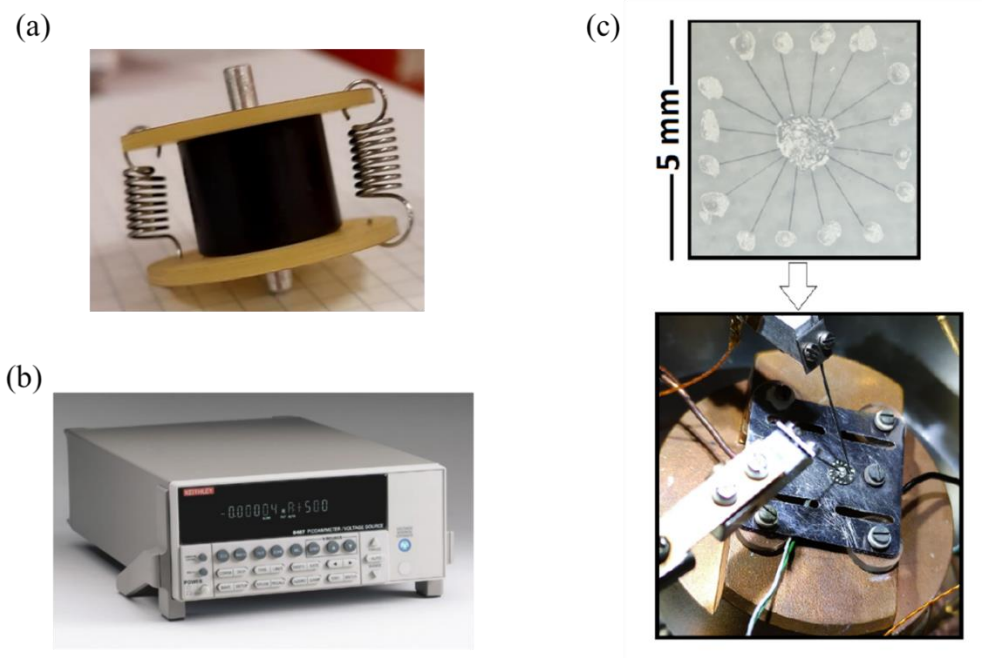

Figure 30: (a) polyammide cylinder to contain ND for electrical measurements; (b) Keithley 6487 picoammeter/voltage source; (c) measure configuration of the conductivity of the diamond biosensor channels.

3 Results

3.1 Characterization of ion beam modified structures in diamond

3.1.1 B implanted diamond (AFM and Raman analysis)

In this first section, the characterization of an ion implanted diamond sample is reported. Although a wide variety of studies already investigated this topic in the past, this study was carried out to provide integrative systematic characterizations, exploring a range of implantation parameters still not available in the literature. More precisely, high energy boron ions were employed, thus creating deep B-doped regions (more than 4 μm), whose realization has promising perspective in the development of integrated devices.

The analysis was conducted on a high-purity ("optical grade", type IIa) monocrystalline (100) oriented diamond, synthetized with Chemical Vapor Deposition by ElementSix™. The sample was previously implanted by the group coordinated by Prof. Maria Dolores Ynsa of the Department of Applied Physics of the "Universidad Autonoma de Madrid", at the microbeam line of the "Center for Micro Analysis of Materials" (CMAM) (Autonomous University of Madrid). An 8 MeV ^{11}B ion beam with a spot size of 5×5 μm^2 was employed to create 12 different square-shaped areas of ~100×100 μm^2 size, irradiated at different fluences and ion currents (see Table 1).

Region label	**Current (pA)**	**Ion fluence (10^{16} cm^{-2})**	**Estimated graphitic layer thickness (μm)**
A	500	0.5	-
B		0.23	-
C		0.1	-
D		4.4	0.309 ± 0.019
E		3.3	0.46 ± 0.03
F		2.1	0.55 ± 0.05
G		0.7	0.102 ± 0.018
H		0.9	0.142 ± 0.016
I		1.2	0.187 ± 0.016
J	50	1	0.157 ± 0.014
K	100	1	
L	500	1	

Table 1: labels of the implanted regions with the respective ion currents and delivered fluences.

After ion irradiation, the sample was annealed in high vacuum (3×10^{-7} mbar pressure) at 1350 °C for 2 h. To clean the diamond surface from graphitic layers formed due to the effect of High Temperature Thermal Annealing (HTTA) process on surface defects [136], the sample underwent an oxygen plasma cleaning for 15 min. In Figure 31 the optical micrograph of the sample is shown, both before and after HTTA. As can be seen from the image, all the irradiated regions were converted to graphite excepted areas B and C, which being irradiated at the lower fluences resulted in the re-conversion to diamond.

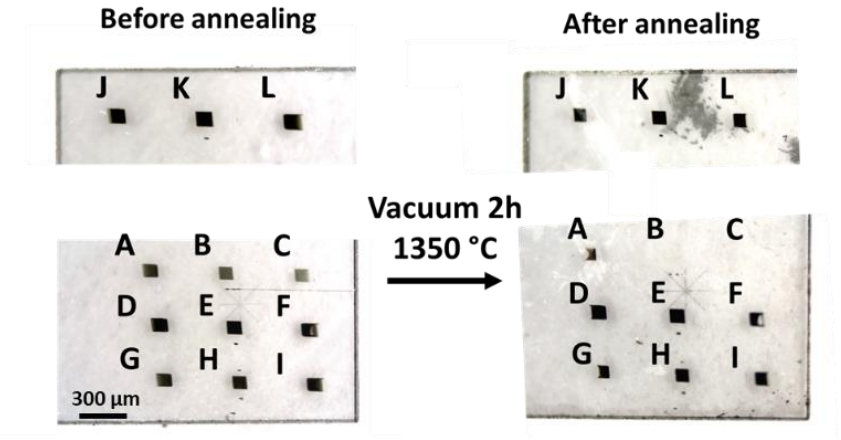

Figure 31: optical image of the implanted regions, before and after HTTA; the squares are labelled accordingly to Table 1.

The radiation-induced vacancy density was estimated with SRIM software, by running the "Detailed calculation with full damage cascades" mode and by multiplying the output linear vacancy density with the fluence delivered to each implanted area (density of diamond $\rho = 3.52$ g cm^{-3} and displacement energy of the carbon atoms of 50 eV were set). This estimation is based on a rough linear approximation that does not consider concurrent complex processes such as self-annealing or defect-defect interaction. The result is shown in Figure 32. As can be observed, 8 MeV B ions range is settled approximately at ~ 4.4 µm, with a maximum value of the linear vacancy density of ~ 800 vacancies µm^{-1} ion^{-1} in correspondence of the Bragg peak. As discussed in paragraph 1.5.1, according to former studies, the graphitization threshold related to ion-induced damage occurs between $2–6\times10^{22}$ vacancies cm^{-3}. In the case of the investigated sample, this threshold seems to have occurred around the fluence delivered in region A (corresponding to ~ 4.4×10^{22} vacancies cm^{-3}). This is further confirmed also by observing that this area resulted only partially graphitized following HTTA, while the areas which were implanted below this threshold recovered completely to diamond. The grey horizontal line in Figure 32 represents this threshold, with a 10% uncertainty which was associated in order to cover both the range of different values

reported in literature and to take into account the experimental uncertainty of the delivered fluences. By considering the intersection of this threshold with the vacancy density plot, it is possible to estimate the thickness of the graphitic layers (the 10% uncertainty was suitably propagated for the error evaluation). The results are reported in Table 1.

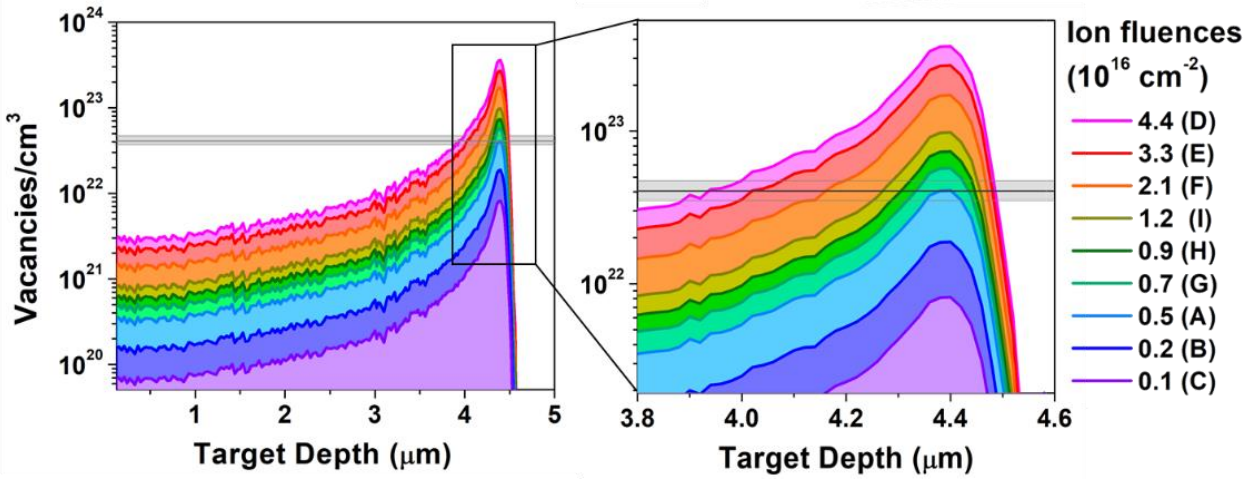

Figure 32: SRIM vacancy density profiles at the different fluences; the grey horizontal line corresponds to the estimated graphitization threshold (ranging between 3.7×10^{22} vacancies cm^{-3} and 4.5×10^{22} vacancies cm^{-3}).

Following the B irradiation, the group of the University of Madrid also performed AFM analysis to study surface topography and to assess the swelling effect due to the pressure applied to the surrounding diamond matrix by the amorphous carbon layer (as it presents a lower atomic density). As the fluence increases, the thickness of the amorphized layers increases, thus determining a more pronounced swelling. Figure 33 shows exemplarily the topography map (a) and the respective cross-sectional profile (b) of the edge of area D (irradiated at 500 pA and achieving a fluence of 4.4×10^{16} cm^{-2}). As expected, the profile evidenced the swelling effect. Moreover, the latter appeared more pronounced in correspondence of the edges of the implanted regions, showing a "lip" structure. This phenomenon was theoretically predicted in previous studies by using finite element methods [96] and analytical models [137] and experimentally observed in samples irradiated with swift heavy ions [138]. In this work, a better spatial resolution was obtained with respect to other studies where this effect was negligible [139].

During its PhD activity, the candidate compared the obtained result with theoretical predictions by applying to the observed lip the analytical model described in [137].

In the latter work, the swelling profile is described with eq. 4:

$$v(x) = v_0 + e^{\beta x}(c_1 \cos(\beta x) + c_2 \mathrm{sen}(\beta x)) + e^{-\beta x}(c_3 \cos(\beta x) + c_4 \sin(\beta x)) \quad (4)$$

where

$$\beta = \sqrt[4]{\frac{3E_{aC}}{E_d(h + v_0)t^3}} \quad (5)$$

$$v_0 = h\frac{(\rho_d - \rho_{aC})}{\rho_d} \quad (6)$$

E_{aC}=21.38 GPa and ρ_{aC}=2.14 g cm^{-3} are the Young Modulus and the density of amorphous carbon respectively. E_d=1144 GPa and ρ_d=3.52 g cm^{-3} are the same parameters referred to the case of diamond. h refers to the thickness of the amorphous carbon layer (estimated in this case as the region at which the graphitization threshold is exceeded, see Table 1 and Figure 32) and t is the thickness of the diamond cap-layer (estimated as the distance between the surface and the depth at which the graphitization threshold is overcome). It is worth noting that diversely from our case, in the mentioned work [137] the sample was investigated following HTTA, thus employing graphite parameters instead of amorphous carbon ones. Boundary conditions (v(0)=0, v′(0)=0, v(l)=0), v′(l)=0) determined the coefficients c1, c2, c3 and c4 (l is the side dimension of the implanted squares, ~100 μm). The result of the simulation is reported together with the measured AFM profile in Figure 33. While the overall profile is not perfectly in line with the theoretical simulation, the horizontal extension of the "lip" on both Z and X axes is acceptably compatible with the prediction. The discrepancies between the result and the simulation can be attributed to the ideal assumptions of the model, where an elastic foundation characterized by well-defined edges and a uniform spring constant embedded in a pristine diamond matrix was considered, differently from the actual case where the elastic foundation is formed by amorphous carbon phases possessing smoother edges with respect to post-annealing graphitic layers.

Concerning the height of the swelling, this depends on the damage density [138,139]. As shown in Figure 33 the collected height data for 8 MeV boron implantation were consistent with previous observations obtained for other ion species and different energies. More concisely, the graph shows the swelling height as a function of the "damage integral". The latter is defined in [138] as (eq. 7):

$$D_{int} = \int_0^{Z_{max}} \left(1 - e^{-\frac{\Phi \cdot S_n(z)}{a}}\right) \quad (7)$$

Φ corresponds to the delivered fluence, while S_n (z) is the nuclear stopping power as a function of the depth (z). a = (1.19 ± 0.11) × 10^{15} cm^{-2} keV nm^{-1} represents an empirical parameter. In this equation, the quantity under integration is defined as "damage fraction" and represents the fraction of amorphized carbon as a function of depth z in the matrix. By integrating this value over the total ion range, the damage integral is obtained, which is proportional to the total swelling occurring at the surface of the implanted diamond.

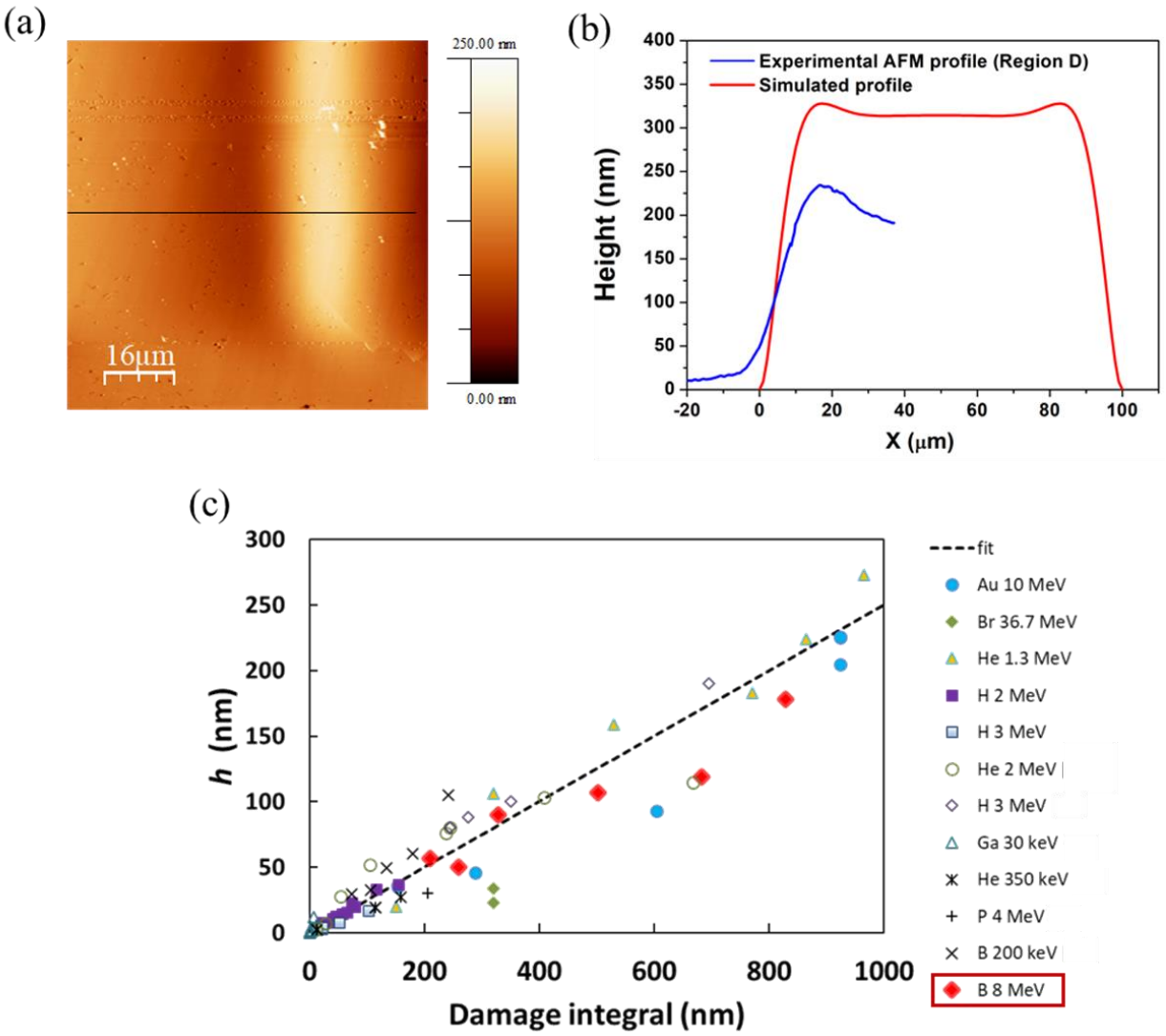

Figure 33: (a) AFM map of the edge of irradiated square D (ref. to Fig. 31); (b) acquired cross-sectional AFM profile from implanted region D along the horizontal black line showed in Fig. 33(a), compared with the simulated profile. (c) "Plateau" swelling height (h) as a function of the damage integral for 8 MeV B ions, in comparison with former data.

The sample was also characterized by the candidate with Raman spectroscopy to obtain structural information about the regions implanted increasing fluences, both before and after the HTTA

process. With the dual purpose of verifying the spatial uniformity of the implanted areas and the adequacy of single-spot spectra to perform the Raman characterization, multiple spectra were collected in linear scanning succession across the implanted areas (see Figure 34a). For each spectrum, the first-order Raman diamond peak signal at 1332 cm^{-1} was integrated after proper baseline subtraction. An exemplary selection of the results (for fluences of 0.23×10^{16} cm^{-2}, 0.9×10^{16} cm^{-2} and 3.3×10^{16} cm^{-2}) is reported in Figure 34b and 34c. The homogeneous intensity profile of the diamond peak across the implanted area confirms the suitability of single spot acquisitions in the center of the squares for the characterization of the whole region. Before HTTA the intensity of the first-order Raman diamond peak decreases as the fluence increases, due to higher crystal damage. After HTTA the squares implanted with a fluence below the graphitization threshold were completely restored to diamond (as evident for region B, blue line in Figure 34c), while all the regions irradiated at fluences overcoming the threshold showed comparable profiles. Indeed, the diamond Raman signals arises only from the diamond "cap-layer" between the surface of the sample and the embedded graphitic structures, thus determining a fainter signal with respect to regions implanted below the graphitization threshold.

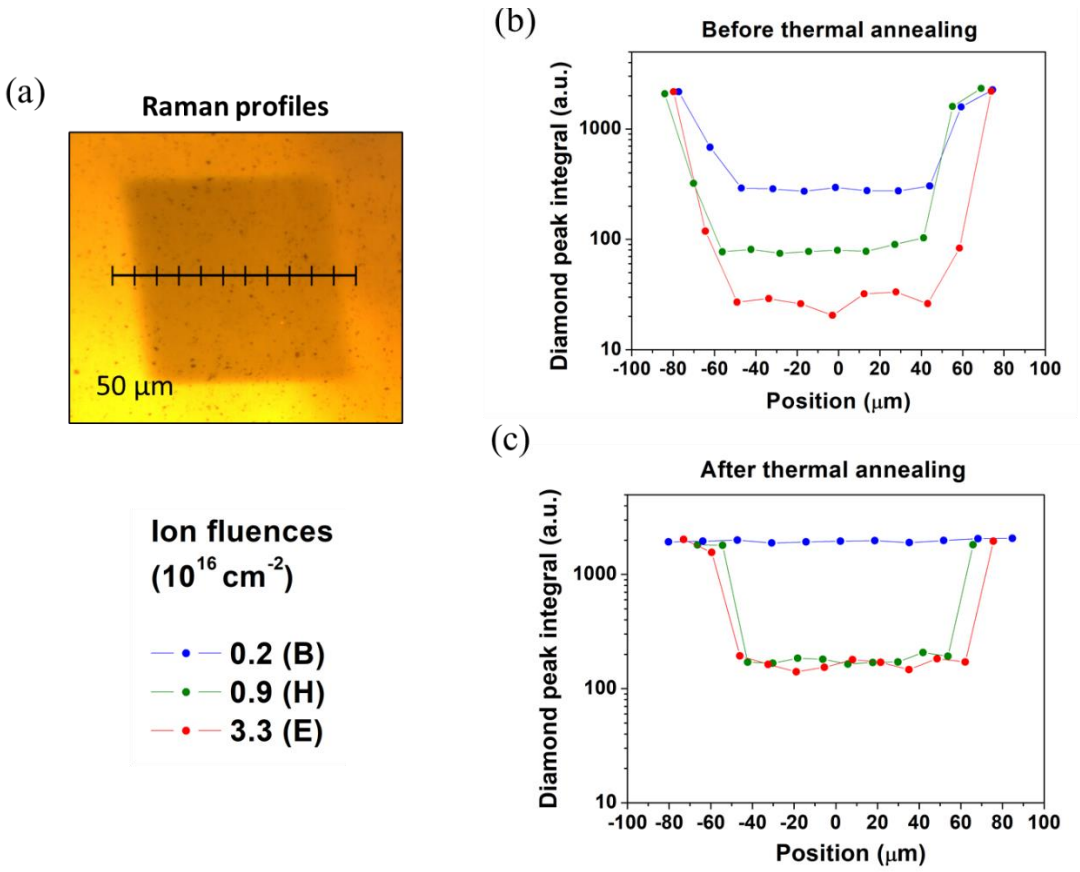

Figure 34: (a) Profile of Raman spectra acquisition; (b) integrated intensity of the first-order Raman diamond peak for regions B, H and E, as acquired before and (c) following HTTA.

Figure 35a shows the Raman spectra collected from all the regions before HTTA. The presented spectra were collected with a single spot acquisition in the center of each implanted area. First-order diamond peak at 1332 cm^{-1} is the main observable Raman feature. At the highest implantation fluences, two small peaks appear at 1500 cm^{-1} and 1635 cm^{-1}. According to the literature [46], these features are generally ascribable to ion damaged diamond and sp^2/amorphous carbon phases. The PL peak centered at 1420 cm^{-1} (575 nm) in the spectrum of the not-implanted areas corresponds to the ZPL of the NV^0 centers. As the damage level increases, its intensity decays until complete disappearance. This effect can be justified with the creation of an increasing number of quenching defects due to ion damage [105].

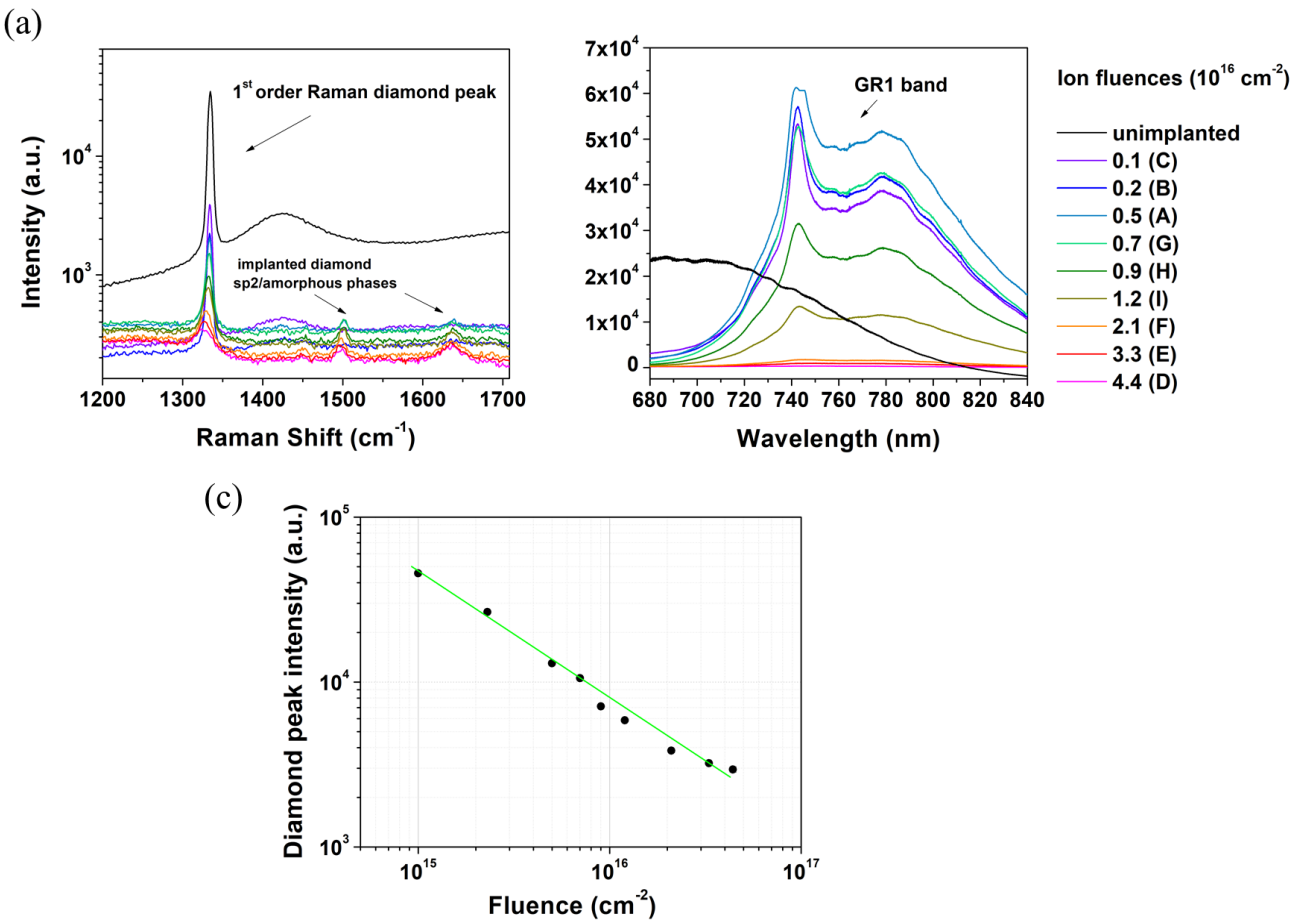

Figure 35: (a) Raman spectra of the implanted regions before HTTA; (b) photoluminescence spectra showing the GR1 band; (c) first-order diamond peak intensity as a function of the delivered fluence; error bars are included in the data points.

The formation of individual vacancies is also evidenced by the photoluminescence spectra shown in Figure 35b, where GR1 centers band appears between 720 nm and 800 nm [95]. This signal is not present in the non-irradiated regions, while it presents a high intensity in the squares implanted

at the lowest fluences, reaching its maximum for a value of 5×10^{15} cm^{-2}. As observed in previous studies [46], the intensity of this PL feature progressively decreases at furtherly increasing boron concentrations, due to the compensation effect of the acceptors. The same effect can also be explained with the creation of multiple vacancy complexes which can be formed at high ion fluences [105]. To evaluate the dependence of the intensity of the first-order Raman diamond peak as a function of the ion fluence (F), a proper fit was performed (Figure 35c). As a result, the intensity of the diamond peak showed a $\sim F^{-(0.77\pm0.04)}$ dependence, in good agreement with previous results [140] where $\sim F^{-1}$ relation was obtained for 60 keV B_2 implantation. A possible explanation for this discrepancy can be determined by the significantly different ion energies.

Following HTTA, the Raman characterization was repeated (Figure 36a).

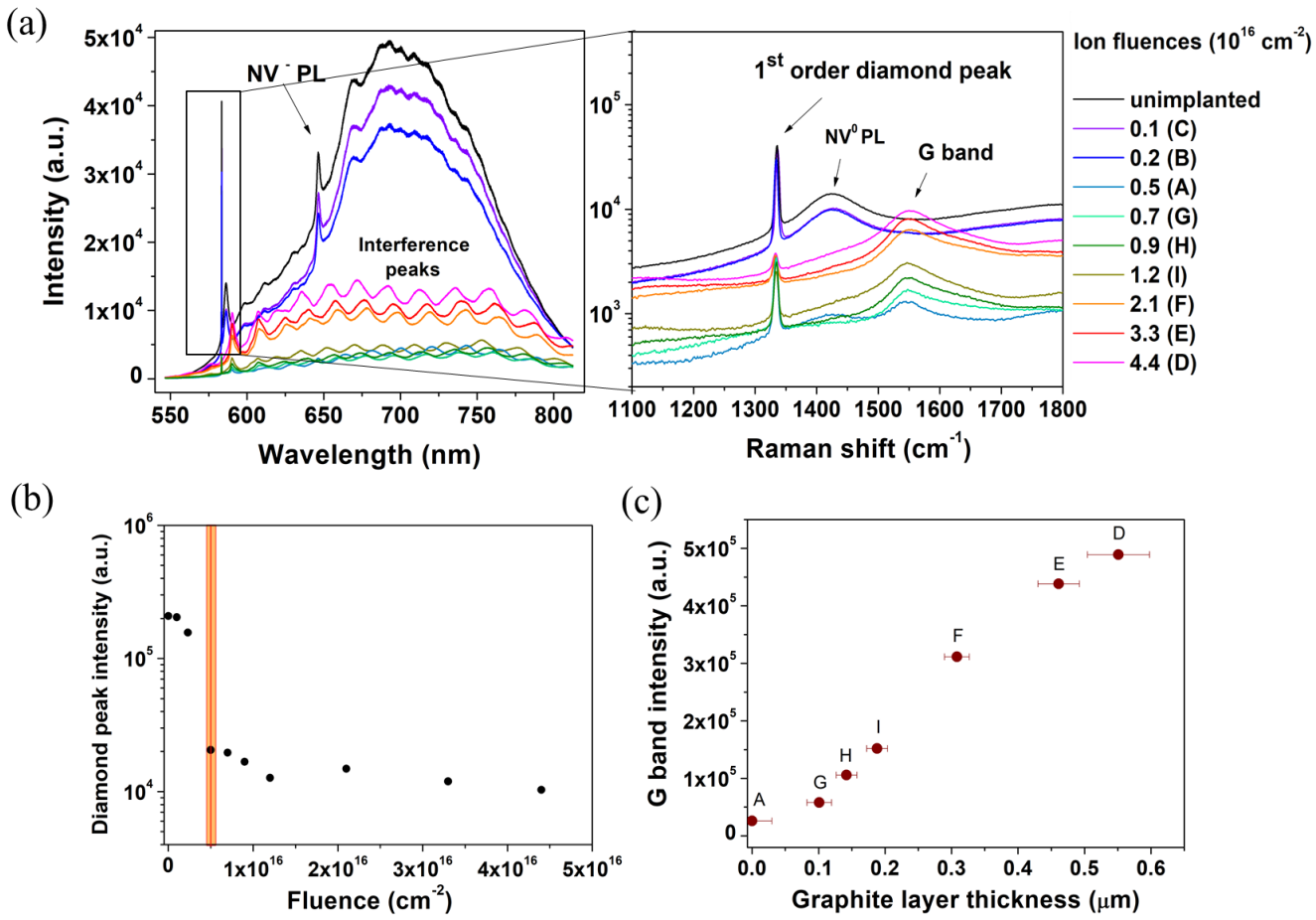

Figure 36: Raman/PL characterization following HTTA. (a) PL spectra acquired on the implanted squares and focus on the spectral region with the main Raman peaks/bands; (b) first-order Raman diamond peak intensity as a function of the delivered fluence; (c) G band intensity as a function of the graphite layer thickness, as estimated from SRIM in Figure 32 and shown in Table 1.

The intensity of the first-order Raman diamond peak at 1332 cm^{-1} (after proper subtraction of the background due to the G-band) decreases as the fluence increases, with a steep decline in correspondence of the fluence that overcomes the graphitization threshold (5×10^{15} cm^{-2}, see Figure 36b). Nonetheless, a smaller peak is still evident also in the graphitized areas due to the "cap layer" contribution. In the latter regions, Raman "G band" appears at 1550 cm^{-1}, which is in fact ascribable to disordered and sp^2 phases. Its intensity gradually increases at higher fluences, with a mostly linear dependence from the values of the graphitic layer thickness that were estimated with SRIM simulation (Figure 36c), thus relating with the increase of the graphitized volume. Not-implanted and regions implanted at low fluence (<7 $\times10^{15}$ cm^{-2}) shows NV^0 and NV^- ZPL at 575 nm and 638 nm, respectively, together with their phonon bands, while as the damaging level increases, a significant reduction of the NV PL emission occurs, together with a peculiar modulation of the spectral emission with periodic interference peaks. This phenomenon was already observed in [95] and can be ascribed to multiple internal reflections of the emitted radiation across the cap layer. Interestingly, it is possible to estimate the thickness of the cap layer from the period of the interference pattern (normal incidence), using the relation of eq. 8 [141]:

$$d = \frac{1}{2n[\frac{1}{\lambda_1}-\frac{1}{\lambda_2}]} \quad (8)$$

where d is the layer thickness, $n(\lambda)$ is the refractive index of diamond, and $\lambda_{1,2}$ are the wavelengths corresponding to two consecutive maxima (or minima) in the spectral pattern. Considering for example region E, the resulting thickness is $d=(4.6 \pm 0.3)$ μm, assuming a refractive index of 2.42 [142], which is, in first approximation, consistent with the expectations.

For a more detailed analysis of the main Raman features as a function of the fluence, in Figure 37a the position and width of the first-order Raman diamond peak is plotted, as measured both before and after HTTA. In general, concerning the peak position, a linearly decreasing trend is observable as damage increases. Due to the HTTA effect in the restoration of the crystal lattice, this tendency is less pronounced than the situation preceding the annealing. However, after HTTA the trend is not flat probably because of a residual amount of damage that does not allow a full recovery of the first-order Raman peak position to its original value. Also the width (as Full Width Half Maximum) of the first-order diamond Raman peak is affected varying the fluence, showing gradual increase with damage (Figure 37b). For similar reasons as for the peak position, also the width variation is less pronounced following HTTA. In both cases, it is worthwhile observing the slope change in correspondence of a fluence near to the graphitization threshold. According to a previous work

[143], these observations can be attributed to a decrease in phonon lifetime as a result of the scattering from the ion-induced defects and are described by the Kramers-Kronig relationships [144].

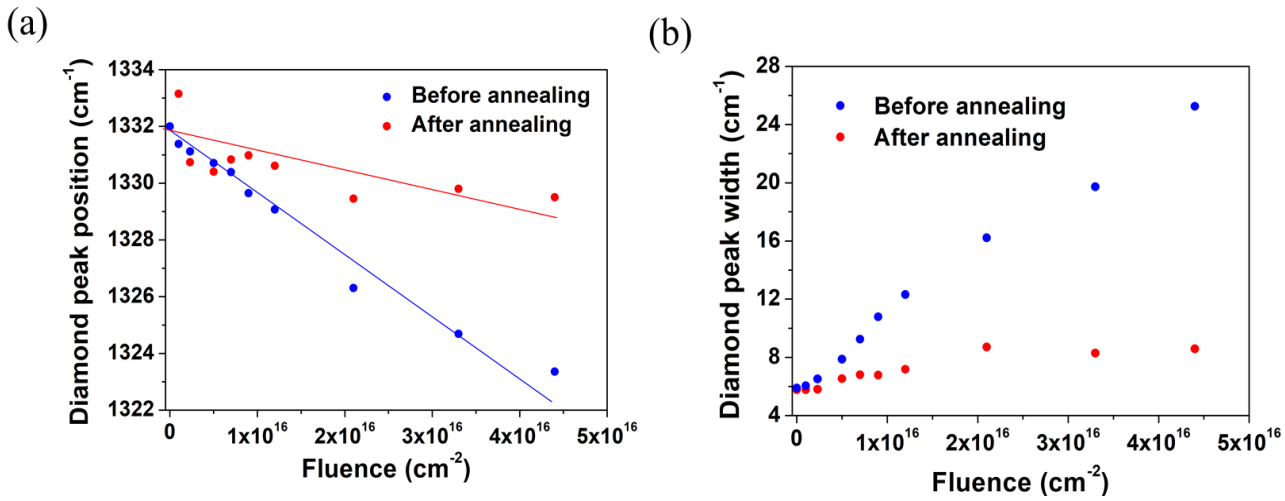

Figure 37: (a) first-order diamond Raman peak position as a function of the irradiation fluence; blue and red lines correspond to the linear fits of the respective data before and after HTTA. (b) First-order diamond Raman peak width as a function of the irradiation fluence before (blue) and after (red) HTTA.

Finally, in Figure 38 the Raman spectra collected from areas implanted at different ion beam currents (50 pA, 100 pA and 500 pA) and fixed fluence (1×10^{16} cm^{-2}, thus above the graphitization threshold). Different irradiation currents allow to evaluate possible "self-annealing" effects. Indeed, thermal heating can occur during ion irradiation, thus promoting the partial migration of the vacancies and the reductio in the vacancy complexes creation. Before HTTA, both the first-order Raman diamond peak at 1332 cm^{-1} (Figure 38a) and GR1 photoluminescence band (Figure 38b) appear higher at 100 pA and 500 pA with respect to 50 pA. Therefore, the use of higher currents showed effectiveness in partially decreasing the damage induced by ion irradiation itself. Figure 38c shows the spectra of the same regions following HTTA, providing results similar to the ones presented for the other implanted squares.

All the data presented in this section were published in [130].

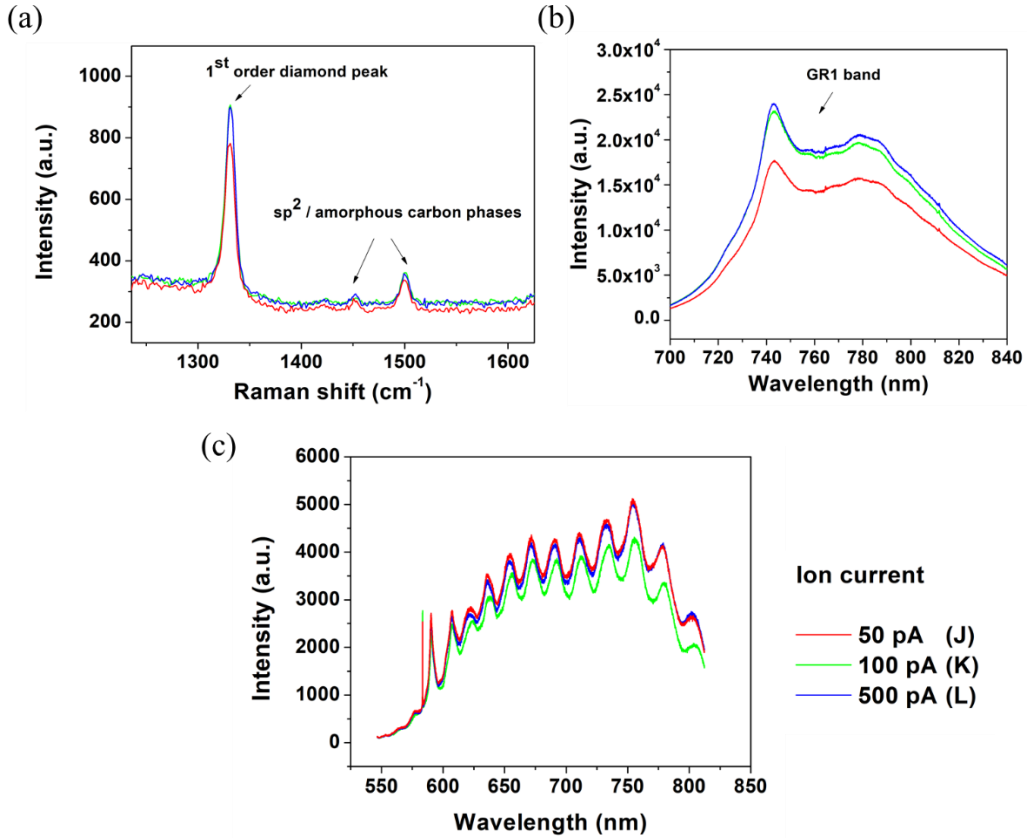

Figure 38: (a) Raman spectra of regions J, K and L before thermal HTTA;(b) PL spectra showing GR1 band of areas J, K and L before HTTA. (c) PL spectra acquired from areas J, K and L after HTTA.

3.1.2 Diamond sensor (electrical and Raman analysis)

This paragraph is devoted to the characterization of a micro-graphite-patterned diamond multi-electrode array (referred as μG-D-MEA) for cellular sensing, as introduced in paragraph 1.5.1. The employed pristine diamond sample was a high-purity, type IIa optical grade, artificial polycrystalline diamond produced with CVD by Diamond Material (Freiburg, Germany). Sizes are $5\times5\times0.4$ μm^3. As already mentioned, the creation of the graphitic microchannels was obtained by means of MeV Ion Beam Lithography. More precisely, a collimated 1.3 MeV He^+ beam with a current density of 1.5 μA cm^{-2} was used for the microchannels fabrication. The beam was provided by the AN2000 accelerator of the Laboratories of Legnaro of the National Institute of Nuclear Physics (LNL-INFN) described in section 2.2 [145]. The total delivered fluence was 1×10^{17} cm^{-2}, enough to guarantee the graphitization of a ~270 nm thick volume at a depth of ~ 2.2 μm from the surface. The geometry of the electrodes was defined by applying over the sample a metallic collimator manufactured by Kirana-laser company, as shown in Figure 39. In addition, a metal mask with a variable thickness profile directly applied on the sample surface allowed the tuning of

the energy of the ions impinging on the diamond substrate, thus allowing the emersion of the channels in correspondence of their ends. The sample was then annealed in high vacuum (10^{-6} mbar) at 950 °C for 2 hours, thus allowing the conversion of the implanted regions to graphite. In this case, due to the lower temperature with respect to the sample investigated in 3.1.1, no surface graphitic layers were formed, thus not requiring a plasma etching process to clean the surface.

The resulting device presents 60 independent graphitic microchannels whose emerging central end-points are arranged as an 8×8 matrix with ~200 μm spacing (see Figure 39). The diamond sensor is mounted on proper chip carriers which allows the signal transmission to a commercially available electronic acquisition chain (MultiChannels System, model MEA1060-Inv-BC). Moreover, a glass ring is mounted on the chip carrier to form a tiny container for cell culture medium (see Figure 39e) which is essential for the development of the cell network and for the administration of specific solutions and drugs.

In this frame, besides taking part to many ion-implantation runs of these devices, the activity of the candidate was focused on preliminary Raman and electrical characterizations to evaluate both the structural and electrical properties of the created micro-electrodes.

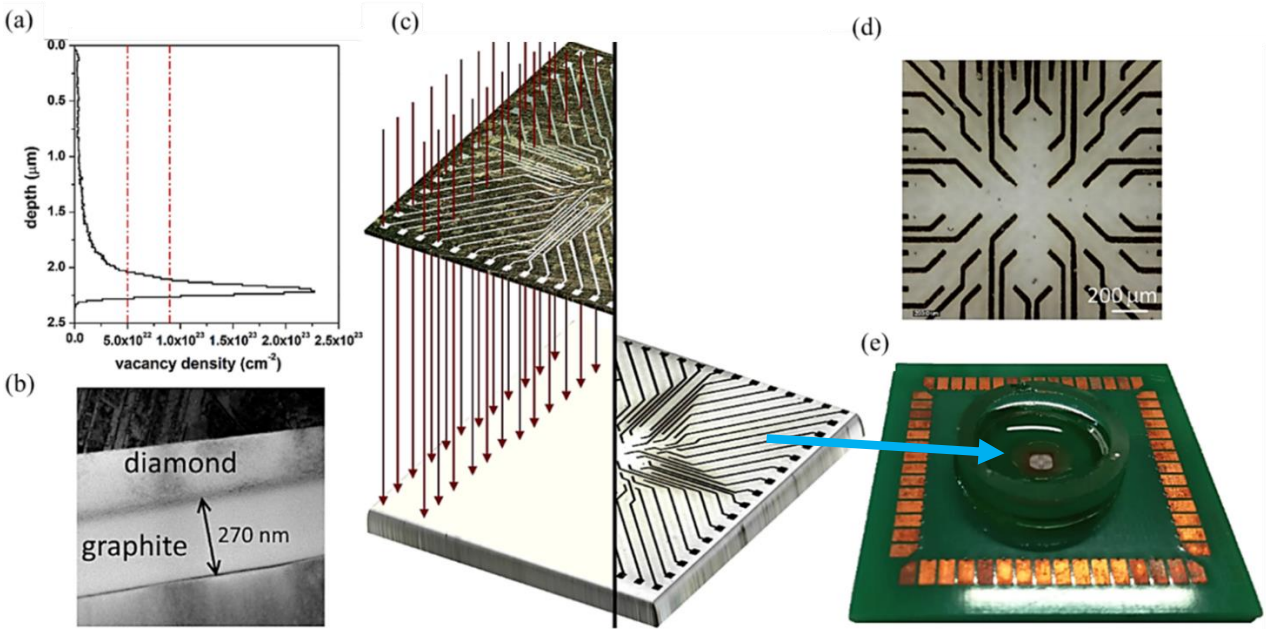

Figure 39: (a) SRIM simulation of vacancy density induced in diamond by 1.8 MeV He ion implantation. Red dashed lines represent the graphitization threshold interval; (b) cross-sectional TEM micrograph of a micro-electrode; (c) scheme of the ion beam fabrication process (left) and resulting device (right); (d) optical top-view picture of the biosensor; (e) image of the assembled biosensor on the chip carrier.

Raman characterization

Figure 40 summarizes the results of the Raman analysis of a microchannel of the biosensor. Raman spectra were acquired from different points of this region, in particular:

- a not-irradiated point of the diamond substrate, far from the implanted electrode (a);
- a point of the diamond substrate few micrometres close to the electrode (b);
- a point in correspondence of the emersion of the electrode (c);
- a point of the diamond substrate located directly above the embedded graphitic electrode (d).

Figure 40e shows the optical image of the emerging end of the investigated channel and the points from which the spectra were collected. The spectra collected from regions (a) and (b) (green and blue spots in Figure 40e) show the characteristic first-order Raman peak of diamond at 1332 cm^{-1}. The photoluminescence band located at 5260 cm^{-1} (739 nm) is ascribable to the Silicon-Vacancy colour centres (Si-V) [146], which are present due to the possible silicon impurities incorporated during the growth of the crystal (10 ppm of Si impurities were declared in the sample datasheet). No amorphous or sp^2-like phases related features are visible. Therefore, unirradiated regions of the sample seems to preserve their pristine diamond structure even in proximity of the channels. By performing the Raman analysis even closer to the implanted electrode (Figure 40b), an additional feature appears at 963 cm^{-1} (561 nm) compatible with the presence of He–related colour centres [147,148] which derives from the He^+ irradiation in correspondence of the microchannel.

Spectra acquired over the red point, Figure 40(c), which corresponds to the emersion area of the graphitic channel, show no diamond peak. Instead, two broad Raman features ascribable to D and G bands appear at 1361 cm^{-1} and 1582 cm^{-1}, respectively. These bands, already observed in spectra of paragraph 3.1.1, are mainly attributable to amorphous and disordered carbon phases (D band) and to C - C bonds vibrations of graphite-like phases (G band), thus confirming the actual exposure of the channel at the sample surface. In addition, a weaker and broader peak addressable to D+D' Raman resonance is evident at 2835 cm^{-1}.

Observing the spectra acquired over the areas located directly above the channels (black spot, Figure 40d), signals arising from both the diamond "cap layer" (first-order diamond Raman peak) and the embedded microelectrode (D and G bands) appear as expected, as the focal depth of the Raman set-up reaches ~3 μm, while the depth of the graphitic channel is approximately around 1 μm.

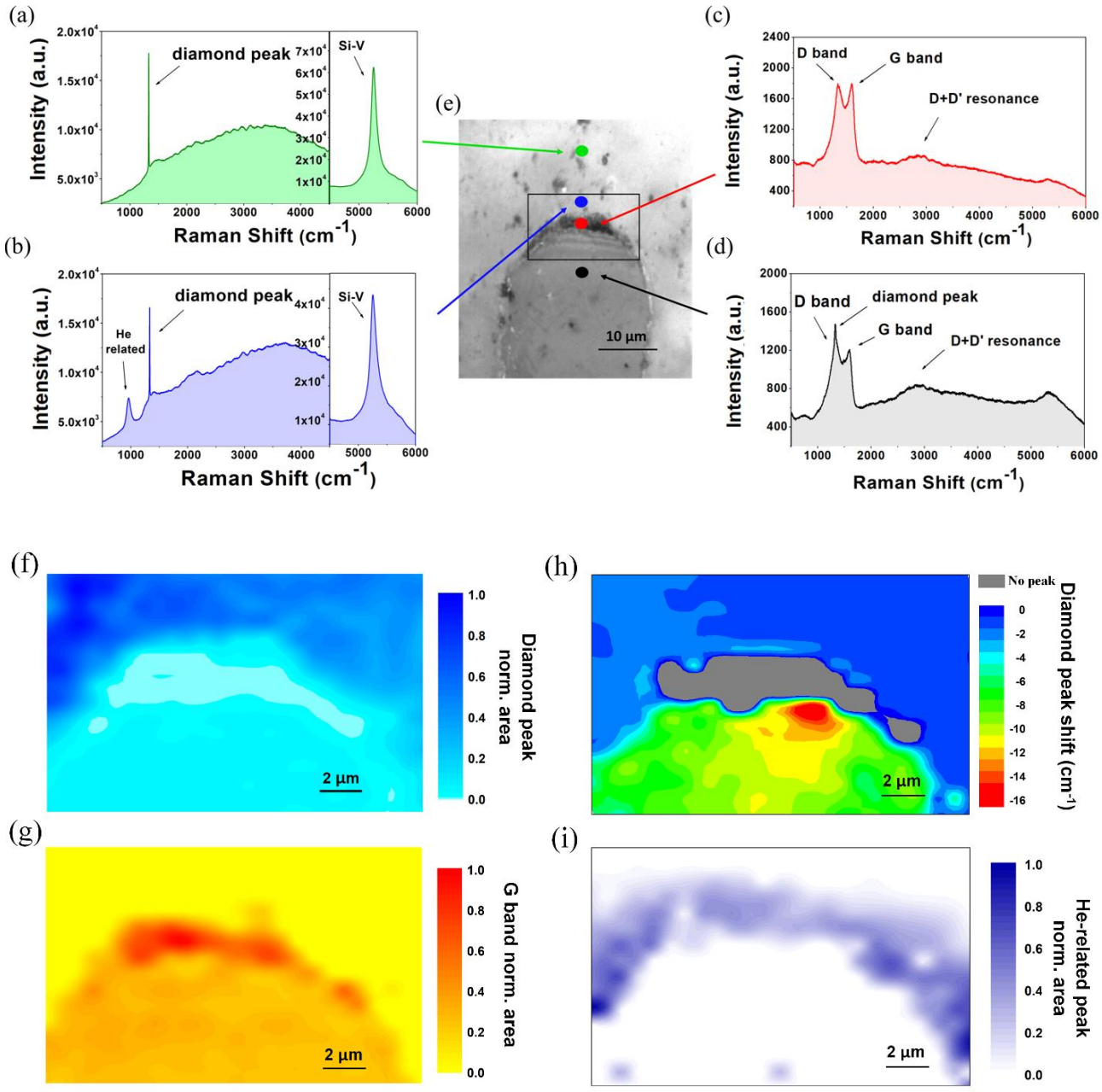

Figure 40: Raman spectra acquired from the diamond (a), the diamond in proximity of the channel (b), the exposed graphitic portion of the microchannel emerging region (c) and above the buried portion of the microelectrode (d); optical micrograph of the characterized electrode – colored points are the positions of the spectra acquisitions (e). Diamond peak (f) and G band (g) Raman intensity maps of the portion of the sensor described by the black square in (e); the color scale represents the normalized area of the integrated spectral range. (h) Map of the first-order diamond peak position shift (difference from 1332 cm^{-1}), proportional to the internal stress provoked by ion beam damaging. Grey color refers to the lack of a detectable diamond peak; (i) He-related peak intensity map.

To evaluate the spatial distributions of the intensities of the first-order Raman peak of diamond and G band, two-dimensional Raman maps of the microchannel were acquired with steps of ~ 0.80 μm along both axis (Figure 40f and 40g, respectively). The reconstruction of the maps was performed by means of a proper script written by the candidate, with particular attention to the correct background subtraction for the evaluation of the intensities of the mapped Raman features. The map related to the integrated first-order diamond peak shows a significant decrease of its intensity in correspondence of the microelectrode, until its total disappearance at the emersion point. Conversely, here the intensity of the G band reaches the maximum. By analysing the maps, it is also possible to evaluate the spatial extension of the graphitic portion exposed to the surface, resulting in an active detection area of ~ 2×10 μm^2.

As discussed in the introduction, due to the expansion pressure of the sub-superficial low-density graphitic channels on the surrounding diamond matrix, mechanical stress of the latter is expected to occur. To provide information about this issue, also the spatial distribution of the spectral red-shift of the first-order Raman peak of diamond was mapped (Figure 40h). A clear downshift of the peak position is evident over the microchannel, where relevant mechanical stress is applied to the diamond cap-layer. The maximum shift (i.e.: ~16 cm^{-1}) occurs in correspondence of an area close to the emersion point of the graphitic electrode. To obtain a rough quantification of the actual pressure occurring in this point, an empirical relation (eq. 9, [149]) correlating the Raman peak shift $\Delta\omega$ with the hydrostatic stress σ_h can be considered:

$$\Delta\omega = a \cdot \sigma_h + b \cdot \sigma_h^2 \qquad (9)$$

where $a = 2.83\ cm^{-1}\ GPa^{-1}$ and $b = -3.65\times10^{-3}\ cm^{-1}\ GPa^{-2}$.

By substituting the maximum shift, a pressure of ~5.7 GPa is obtained. This value is significantly higher with respect to previously results from non-emerging graphitic structures [150]. Nonetheless, this stress did not result in visible cracks or other mechanical damages around the emerging point.

Another interesting feature whose intensity was mapped is the He-related peak at 963 cm^{-1} (Figure 40i). The highest intensity is observed all around the outline of the channel structure, where a low fluence (below the graphitization threshold, but enough to implant He atoms and create He-related color centers) manage to reach the sample during the implantation. Differently, this signal is not observable anymore far from the irradiated area or over the channel, since the high fluence reached in this portion introduced too many defects acting as luminescence quenchers of the He colour center, similarly to what happened to the Si-V center luminescence.

Electrical characterization

To verify the electrical conduction of the graphitic microchannels, current-voltage characterization was carried out with the Keithley 2636 electrometer described in section 2.7. The measurements were performed in the ± 3 V voltage range at room temperature. To prepare the sample for the measures, small drops of silver paste were deposited on the ends of the channels to reduce the contact resistance between the probe microtip and the graphitic electrodes. The results are reported in Figure 41. All the I-V characteristics collected from the microchannels presented an ohmic behaviour, with resistance values ranging between 4 kΩ and 9 kΩ. The main explanation of this variability can be ascribed to the different geometrical parameters of the electrodes (see Figure 39d). Length and width of the channels (quantified from optical micrographs) as well as from their thickness (evaluated from cross-sectional TEM measurements, Figure 39b) were used to determine a mean value of resistivity equal to (2.7 ± 0.3) mΩ cm. This result is compatible with former works of the solid-state physics group [41,151] and with the resistivity of polycrystalline graphite. Indeed, the latter is comprised between the resistivity occurring along the parallel (0.5 mΩ cm) and perpendicular (300 mΩ cm) direction with respect to the graphitic planes [152].

Two additional drops were deposited on the diamond surface far from the microelectrodes in order evaluate the potential presence of parasitic conduction paths due to surface contaminations. In this case (see dashed line in Figure 41) the surface resistance resulted consistent with that of the electrometer (>1 TΩ).

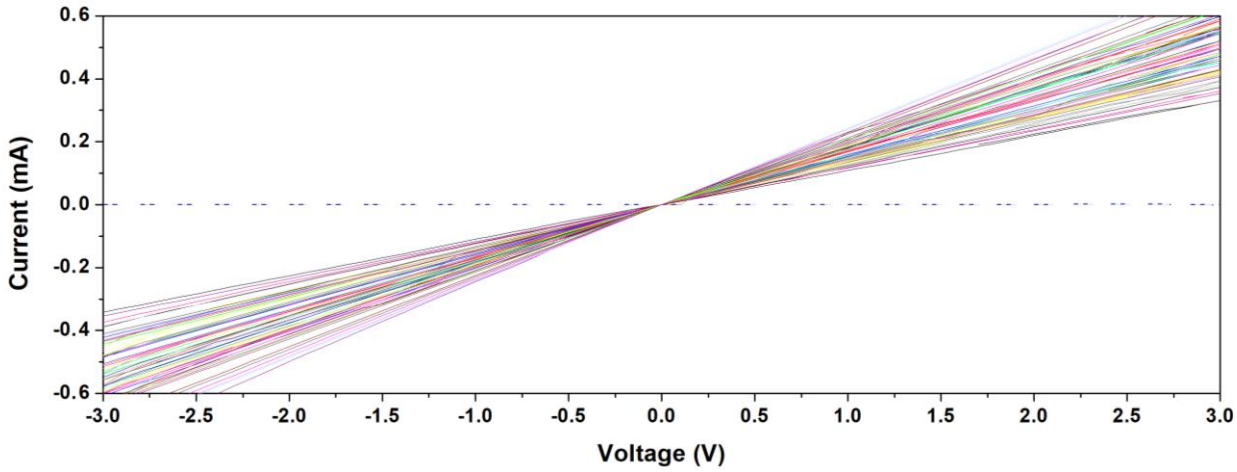

Figure 41: current-voltage curves for the 60 channels of the μG-D-MEA

3.1.3 Application of diamond-based biosensor for excitable cells study

As mentioned in section 1.5.1, the realized biosensor is meant to be applied mainly in the detection of the electrical and/or the secretory activity of neuronal and excitable cells (e.g.: cardiac tissue cells). In this paragraph a brief synthesis of the typical measurements performed by the colleagues of the Department of Drug Science and Technology are showed.

Action potential measurement

The action potentials (AP) are electrical signals that propagates along the axons of neuronal cells, allowing the communication with other neurons and the activation of physiological functions such as muscle cell contraction (included the heart).

The recordings of these signals are performed by employing a commercial "MCS MEA 1060-Inv-BC" amplifier from Multi Channel Systems (Figure 42a).

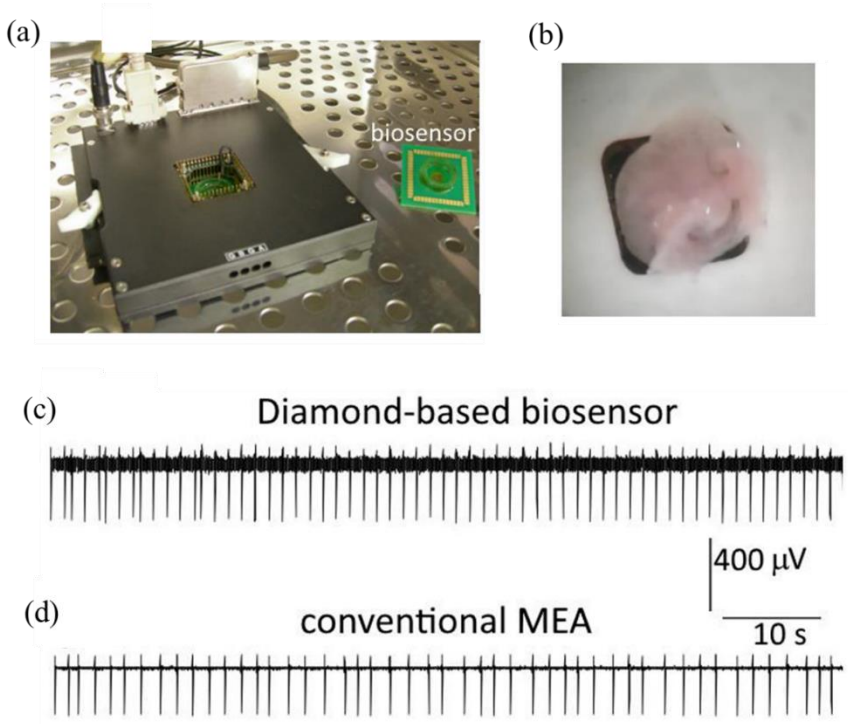

Figure 42: (a) front-end electronic (on the left) and biosensor mounted on the chip carrier (on the right); (b) picture of the sinoatrial node on the biosensor; (c) potentiometric trace of action potentials from the sinoatrial node was performed with µG-D-MEA and (d) with conventional MEA.

The diamond biosensors are characterized by a half-band noise of (35 ± 5) µV, thus possessing performances comparable with those of conventional Multi Electrode Array device (60MEA200/300iR-Ti, Multi Channels System), which possesses a noise level of (22 ± 2) µV. The

proper operation of the device was evaluated by performing in vitro measurements of the action potential occurring in the sinoatrial node, which is responsible for the generation of the electrical pulses at the basis of the heart contraction. This tissue was selected as it represents a benchmark biological sample generating intense action potentials (i.e. ~ 300 μV) across the whole tissue. The intact sinoatrial node (Figure 42b) was surgically obtained from a mouse and placed on the sensors recording area, under the perfusion with a saline standard solution at room temperature.

Figure 42c shows a representative trace of the sinoatrial node spontaneous activity acquired with μG-D-MEA. In this case, the mean basal frequency of firing was (3.5 ± 0.4) Hz. As for comparison, the same measurement was conducted on a convention MEA, resulting in a frequency of (2.8 ± 0.6) Hz (Figure 42d). The measured frequencies values were statistically compatible ($p > 0.05$).

Action potentials can be measured with the same sensors also from neurons directly plated above, as exemplary shown in Figure 43. In this case, the experiment was carried on hippocampal neuronal networks, requiring the capability of measuring lower intensity (few tens of μV) and faster (few ms) signals. The excellent diamond biocompatibility provides a proper adhesion onto the surface of the biosensor, which is fundamental for the signal collection (Figure 43a). Also for these measurements, an example of a potentiometric recording is shown in Figure 43b, which confirms the applicability of the developed biosensor for the detection of action potential also from cultured neurons plated directly on the surface of the sensor.

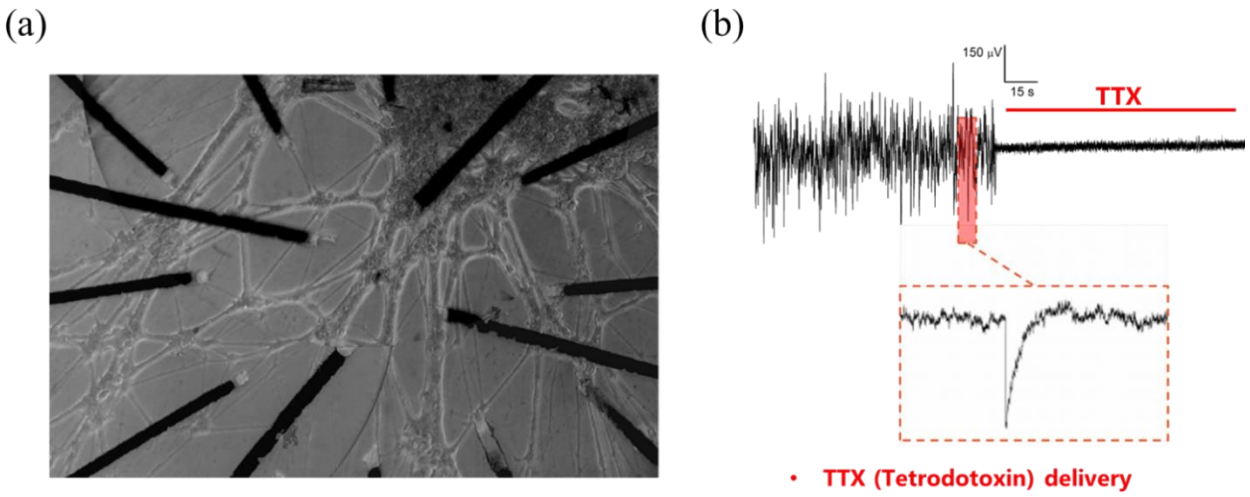

Figure 43: hippocampal neurons cultured on the diamond biosensor, with axons passing on the sensitive ends of the graphitic channels; (b) potentiometric recording before and after tetrodotoxin (TTX) administration (which acts as firing blocker).

Amperometric measurements

When employed in amperometric configuration, the biosensor allows the detection of secreted molecules from cultured cells. The measure is mediated by an oxidation-reduction reaction, obtained by properly polarizing the graphitic electrodes. Indeed, the neurotransmitters released by exocytosis are oxidized in correspondence of the surface of the microelectrode. From this reaction, electrons are released, and an electrical current is measured. A "spike" signal for each individual vesicular release is thus recorded. Figure 44 schematizes the process in the case of dopamine exocytosis. With this technique, the detection of neurotransmitters released by exocytosis from neuroendocrine chromaffin cells was extensively demonstrated with the biosensor and the results were published in previous works by the solid-state physics group [97,98].

In this paragraph, an exemplary proof-of-concept demonstration of the measurement of dopamine release from midbrain neurons is presented. With respect to chromaffin cells, the neurotransmitter release from neuronal cells is characterized by a smaller dimension of the vesicles and a consistently lower number of secreted molecules, thus requiring an optimization of the acquisition parameters (bias applied to the electrodes optimization by cyclic voltammetry [101] and low-pass band frequencies were increased) in order to successfully measure oxidative currents of the order of few pA and with a duration of fractions of ms.

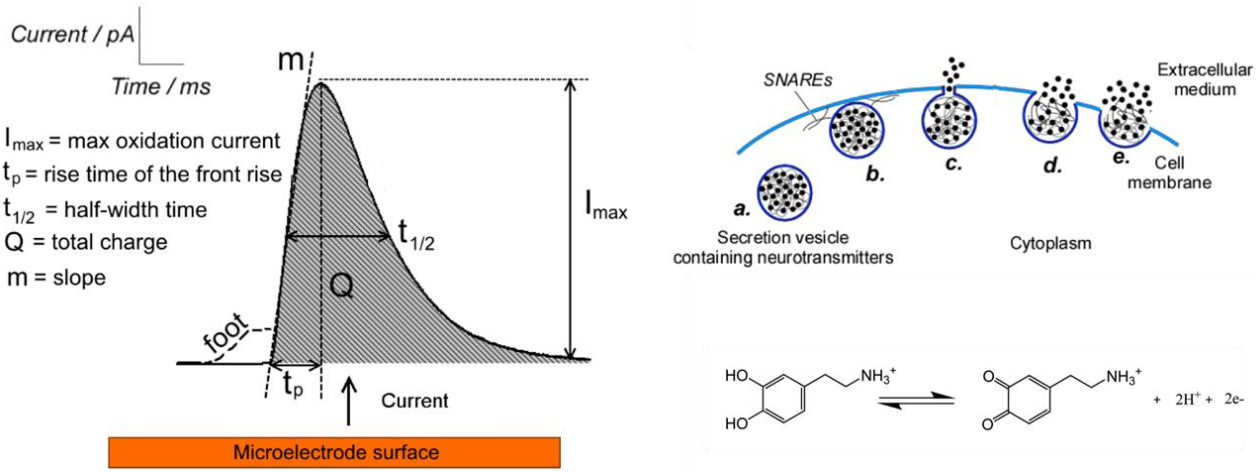

Figure 44: amperometric signal following exocytosis of dopamine, which undergoes oxidation on the microelectrodes.

The presented secretion measurements (Figure 45) were obtained from 12 days in-vitro midbrain neuron network by setting the sampling frequency at 8 kHz and 25 kHz with 800 mV electrode

bias. From the analysis of the acquired data, many parameters such as half-time width ($t_{1/2}$) and maximum current (I_{max}) can be studied to provide information about the exocytic process.

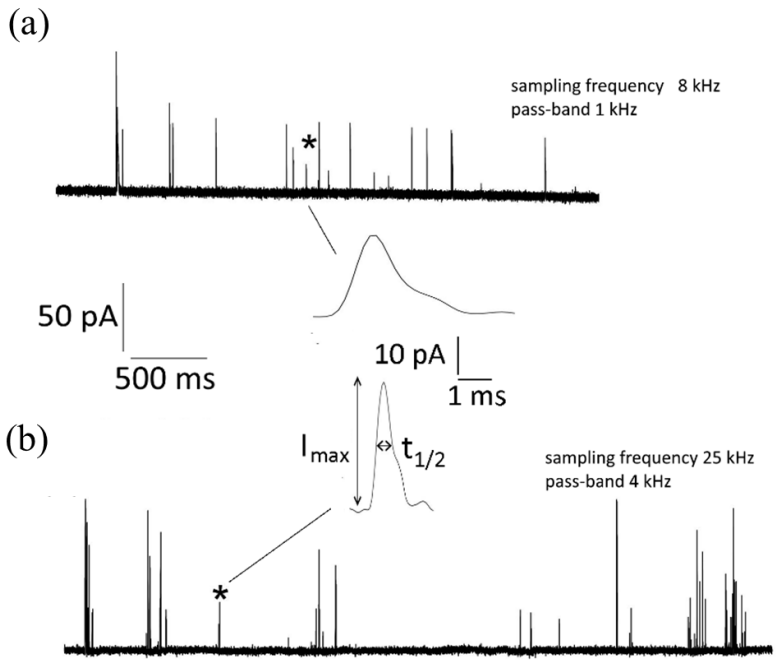

Figure 45: examples of amperograms collected from dopaminergic neurons at 8 kHz and 25 kHz of sampling frequency [101].

Both in the case of electrical and secretory activity, drugs or specific solutions can be administered in order to monitor their effect on the cell functioning.

3.2 Nanodiamonds

This chapter is dedicated to the main topic of the activity carried out by the candidate, concerning the modification and characterization of nanodiamonds.

Overall, four different batches of ND were investigated in this thesis, namely:

- detonation nanodiamonds (DND) from Adamas (NC, USA), with 5 nm nominal primary particle size;
- nanodiamonds produced from the milling of HPHT type-Ib single crystals (Milled Nanodiamonds MND):
    - Microdiamant MSY 0-0.1 with particle size varying in the 0-100 nm range (MSY-MND);

- ElementSix™ Micron+ with particle size varying in the 0-250 nm range (small Milled Nanodiamonds s-E6-MND);
- ElementSix™ Micron+ with particle size varying in the 0.5-1 μm range (large Milled Nanodiamonds l-E6-MND).

3.2.1 Basic modification and characterization

In this section, a systematic characterization of the above-listed samples is presented. Firstly, the ND were imaged with electron microscopy. Figure 46 shows TEM (for DND) and SEM (for MSY-MND, s-E6-MND and l-E6-MND) images of the untreated samples and the average diameter distributions. The latter were obtained by employing Fiji software, an ImageJ-based open-source image processing package. After adjusting their brightness and contrast, the images were converted in binary and the "watershed" feature from BioVoxxel toolbox [153] was applied to discriminate between touching particles. The use of the "particle analysis" feature of the software provided the value of the projected areas of ND, which were converted to diameters by assuming for simplicity a spherical geometry. When the pictures presented a bad contrast or overlap between ND preventing from a proper automated analysis, the measures were performed manually. As anticipated, DND analysis was assessed by means of TEM microscopy, due to the small size of the primary nanocrystals. The dimension of the nanoparticles was evaluated with a manual procedure since their images looked grainy and therefore the automatic procedure was inappropriate for the analysis. Eventually, the histograms of the size distribution were created by applying a proper binning (size measures from 4-5 micrographs from each sample were merged).

Morphologically, the ND presented sharp and irregular shapes. MND resulted properly dispersed, while DND primary nanoparticles were observed mostly in aggregates of 30-130 nm in diameter. Median diameters of the primary nanocrystals resulted in 3.1 nm for DND, 55 nm for MSY-MND, 240 nm for s-E6-MND and 400 nm for l-E6-MND, as reported in Figure 46. The widths of the distributions were significantly high (σ_{DND}: ~ 1.4 nm, $\sigma_{MSY\text{-}MND}$: ~ 24 nm, $\sigma_{s\text{-}E6\text{-}MND}$: ~ 90 nm and $\sigma_{l\text{-}E6\text{-}MND}$: ~ 140 nm) and the fractionation of their dimensions should be considered in the future in the perspective of biomedical applications.

After this preliminary characterization, the different batches of nanodiamonds were studied and compared in terms of their chemical and physical properties. In this first part, ND were investigated exploratively in three different versions:

1) as received

2) after HTTA in N_2 flux for 2 h at 800 °C

3) after process n° (2) + an air oxidation treatment for 8 h at 450 °C

For both processes (2) and (3), the tubular furnace described in section 2.1 was employed.

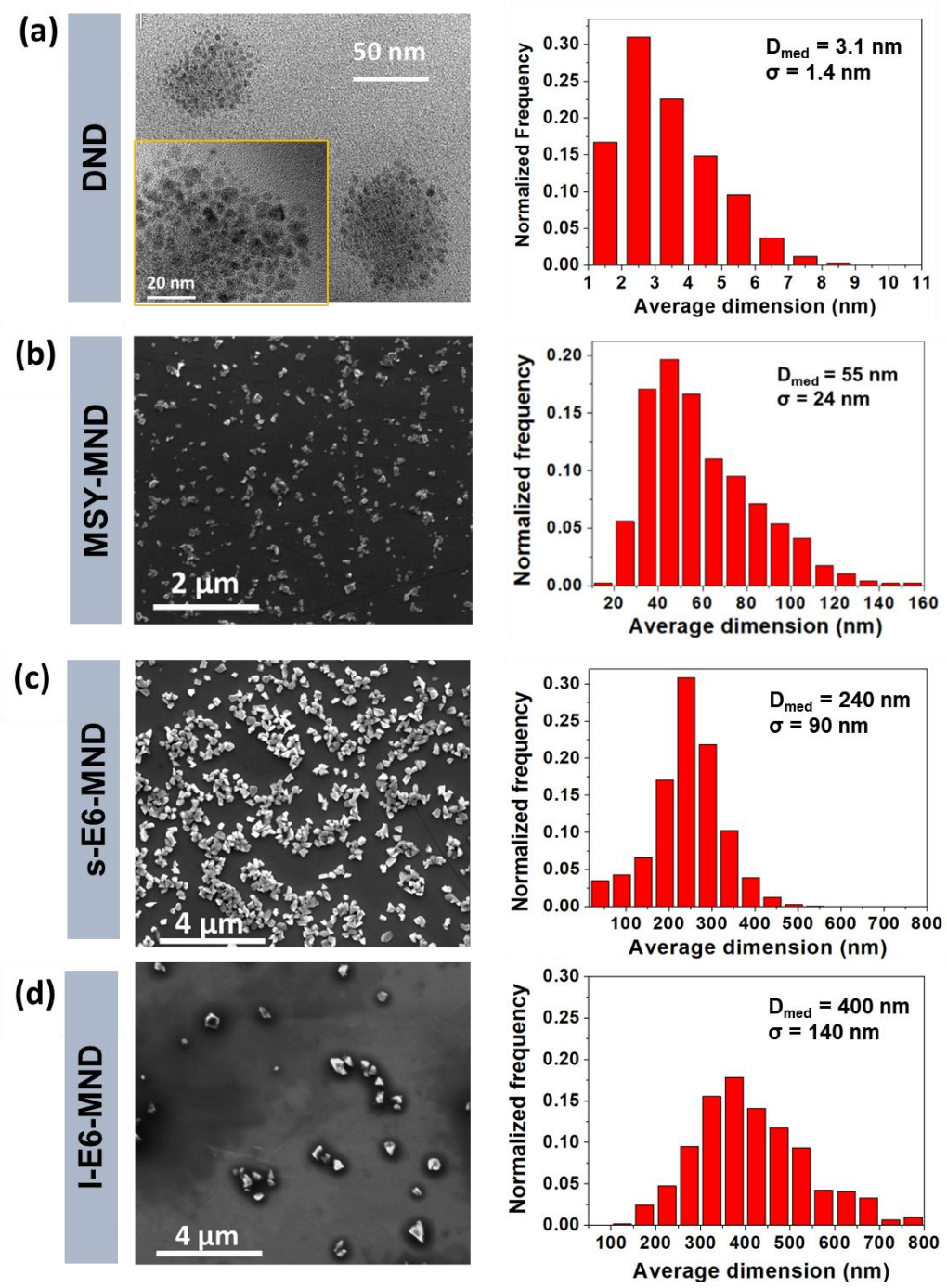

Figure 46: TEM (DND (a)) and SEM (MSY-MND (b), s-E6-MND (c) and l-E6-MND (d)) images and derived size distributions.

The HTTA process was conducted to reorganize the disordered sp^2/sp^3 phases [130] and graphitize the amorphous carbon outer layers while preserving the diamond phase. In addition, the lack of oxygen induces the chemical reduction of the surface of the nanocrystals. The setting of an optimal annealing temperature is of fundamental importance in order to avoid undesired structural and chemical degradation of the ND during the process. On one hand, the nitrogen flux provides an inert environment that prevents the chemical etching of diamond that would occur above 500 °C in presence of oxygen [154]. On the other hand, despite the inert atmosphere, a temperature below 900 °C is necessary to prevent the samples from graphitization [155] and the conversion to carbon onions [156]. Therefore, the HTTA process was performed at 800 °C. Subsequently, to selectively etch the surface graphitic shells and to cover the ND surface with oxygen-containing groups, the air oxidation process was carried out at 450 °C, thus keeping below the diamond degradation temperature. In the following paragraphs Raman/PL spectroscopy, FT-IR analysis and DLS characterization of these samples are presented.

Raman and photoluminescence spectroscopy

Raman/photoluminescence spectrometer was employed to characterize both the structural and the photoluminescence properties of the samples. Figure 47 shows the resulting spectra from DND, MSY-MND, s-E6-MND and l-E6-MND at each processing step. Untreated DND spectra showed two main Raman signals: the D-band around 1360 cm^{-1} and the G-band at 1580 cm^{-1}, suggesting the presence of defective sp^2-like phases. No first-order Raman diamond peak was evident for the untreated and annealed DND, while a small peak was observed in the annealed + oxidized samples. These results are in agreement with the very small size of the DND primary nanoparticles. Indeed, the relevant quantity of sp^2 layers and their higher Raman scattering cross-section (r) with respect to that of diamond phases ($r_{sp3} = 9\times10^{-7}$ cm^{-1} sr^{-1}; $r_{sp2} = 5\times10^{-5}$ cm^{-1} sr^{-1} [46]) should determine a negligible Raman signal from the latter.

MSY-MND still present a weak G-band signal, particularly for annealed samples, while following oxidation it disappears. In these samples, the first-order Raman diamond peak is observed around ~1320 cm^{-1}, downshifted with respect to its theoretical position (1332 cm^{-1}) because of the nanocrystals defectiveness, as well as the already mentioned presence of graphite contaminations which induce heating phenomena during laser irradiation with the Raman spectrometer [82]. Due to their minor defectiveness, for both s- and l-E6-MND samples the first-order diamond Raman peak arises at ~1332 cm^{-1}, while the D- and G-bands are no longer visible. Consistently with their crystal core size, diamond peak intensity follows the order l-E6-MND > s-E6-MND > MSY-MND,

also being related with the surface graphitic contaminations, which are lower in larger-sized nanocrystals in accord with the minor stresses occurred in milder grinding synthesis procedures. The HTTA treatment increases the G-band intensity in DND and MSY-MND samples, due to the graphitization of the amorphous carbon phases surrounding the diamond core of ND. Oppositely, the subsequent air oxidation, by etching such sp^2 shells, determines the almost full disappearance of its Raman signal.

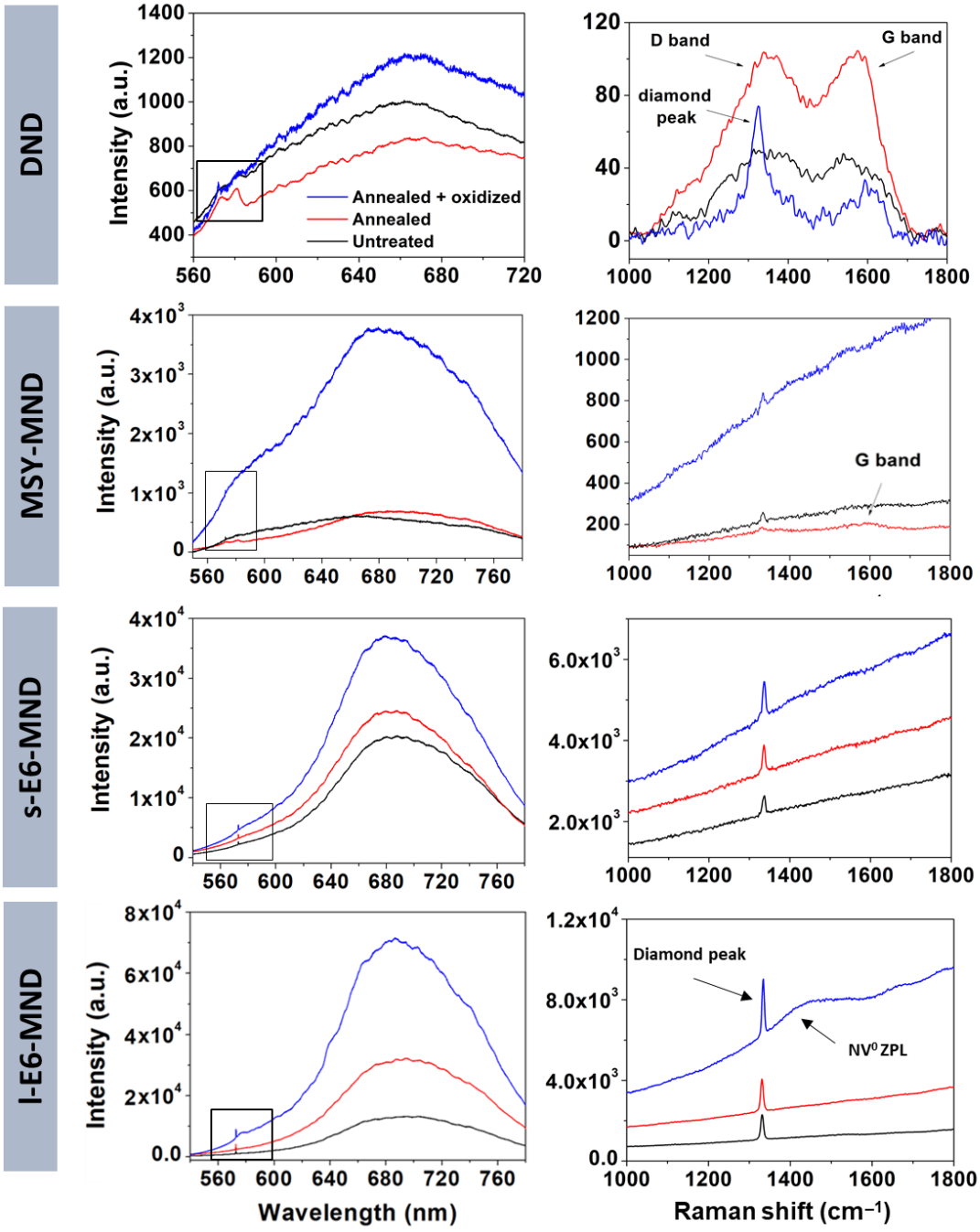

Figure 47: PL (left) and Raman (right) spectra of untreated (black), annealed (red) and annealed + oxidized (blue) DND, MSY-MND, s-E6-MND ad l-E6-MND. Measurements were conducted on compacted ND powders; Obj.: 20×; filter: D1.

The PL emission of NV centers observable between 580 and 780 nm appears very weak in DND samples, without showing significant changes following thermal treatments. Similarly, this fact can be justified with the very low presence of sp^3 diamond phases which can host the color centers. Instead, MSY-, s-E6- and l-E6-MND showed a relevant enhancement in the PL emission following oxidation, with the emersion, in the case of l-E6-MND, of two peaks at ~575 nm and ~638 nm, which corresponds to the ZPL of the NV^0 and NV^- centers, respectively. This observation is consistent with the removal of the quenching effect due to the defective external shells, as suggested in a former study [81].

DLS analysis

Besides the described structural and optical properties, the surface chemistry should significantly differ in the treated samples and can be reflected in the dispersibility and stability of the nanoparticles in aqueous environment. Water solubility of ND is an important condition when willing to interface them with physiological environments, and high hydrophilicity and proper dispersibility are therefore essential. To investigate this issue, the samples were analyzed by means of DLS size and Z-potential measurements. To this scope, 0.5 mM NaCl water solutions were prepared. All ND at the different processing steps were then dispersed in these solutions with a 50 $\mu g\ ml^{-1}$ concentration. The introduction of a minimal quantity of NaCl was necessary for an adequate electric field propagation along with the whole analysis cell during Z-potential analysis [157]. Before each measure, the liquid suspensions were sonicated for 15 minutes with Elmasonic S15H (35 W ultrasonic power). Figure 48a reports the size distributions weighted by number (thus showing an intensity proportional to the relative amount of nanoparticles at each size value). Overall, annealed ND showed higher size values with respect to the other treatments, suggesting an important aggregation level and poorer dispersibility in water with respect to untreated and oxidized samples. Indeed, lower hydrophilicity is expected due to the surface reduction effect of HTTA. Conversely, probably better hydrophilicity of the oxygen-containing chemical groups terminating the surface of untreated and oxidized ND can promote a good solubility and reduce their tendency to aggregation. In general, s-E6-MND and l-E6-MND samples present size distributions consistent with the dimensions of the primary particles as estimated by TEM/SEM techniques. MSY-MND analysis evidenced the presence of a mild agglomeration, while all DND samples showed a severe aggregation level, especially following HTTA. This evidence can be ascribed to the wider interaction surface typical of smaller nanoparticles. In addition, during detonation ND synthesis, the single nanocrystals (with 5 nm primary dimensions) bind to each

other, thus creating strongly bound aggregates of a tenth of nm [158] and furtherly forming large clusters up to 1 micron, which are tough to segregate, particularly in hydrophobic surface conditions.

When studying the Z-potential, it is useful to combine the results with the impact in terms of size distribution mentioned above. Considering in first approximation a spherical geometry of the aggregates, an aggregation parameter was thus defined by dividing the peak value of the diameter distributions by the median diameter value of the ND as calculated from the TEM/SEM images. Z-potential as a function of this parameter is shown in Figure 48b. In general, higher (in absolute value) Z-potentials resulted correlated with higher dispersibility, as a stronger surface charge induces repulsions between the nanoparticles, thus preventing, or at least reducing, aggregation phenomena. Consistently with their better dispersibility, Z-potential of untreated and oxidized ND was stronger than annealed samples. Indeed, the presence of surface oxygen-containing functional groups has been correlated with a higher surface charge in solution [159]. Besides their larger exposed surface, the poor stability in solution of DND samples, especially following HTTA, is thus well explained by the very low surface Z-potential.

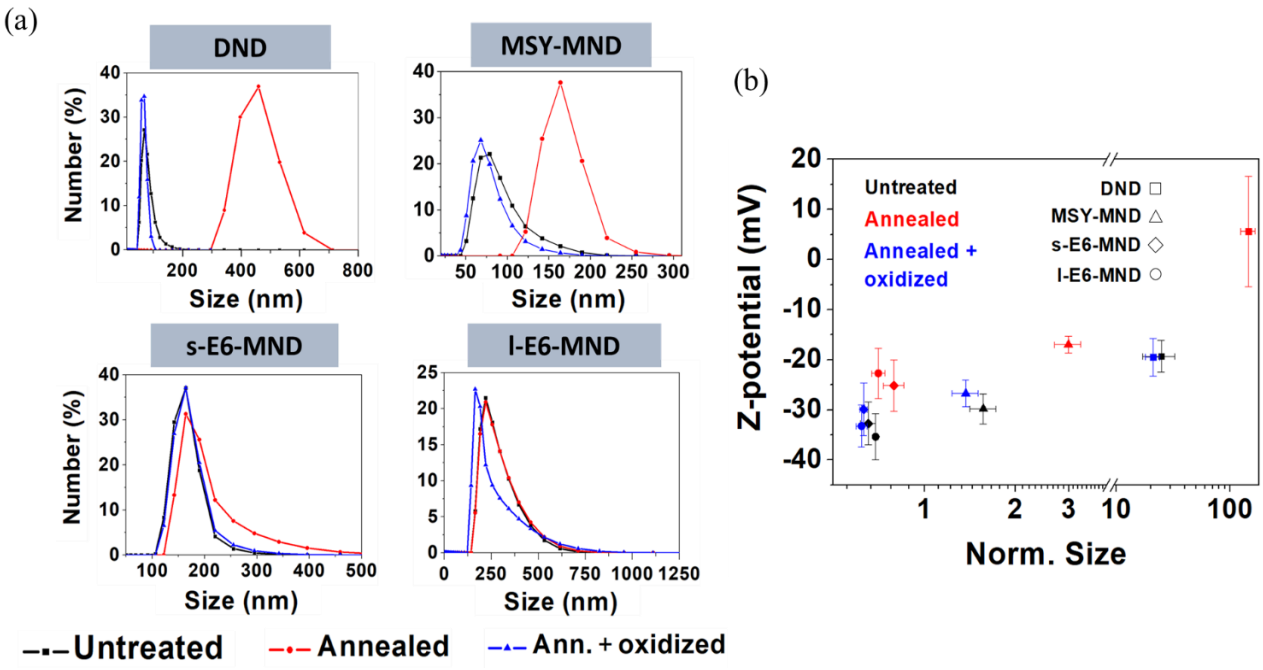

Figure 48: (a) DLS size distributions by number and (b) Z-potential as a function of the normalized size (i.e.: the ratio between the size average from (a) and the median sizes of primary nanoparticles from TEM/SEM analysis).

DRIFT analysis

DRIFT analysis was carried out for a better comprehension of the data obtained by DLS analysis and to provide a detailed understanding of the surface chemistry. Spectra for all the samples (reported in Figure 49) were collected in dry air environment, after 10 minutes of equilibration.

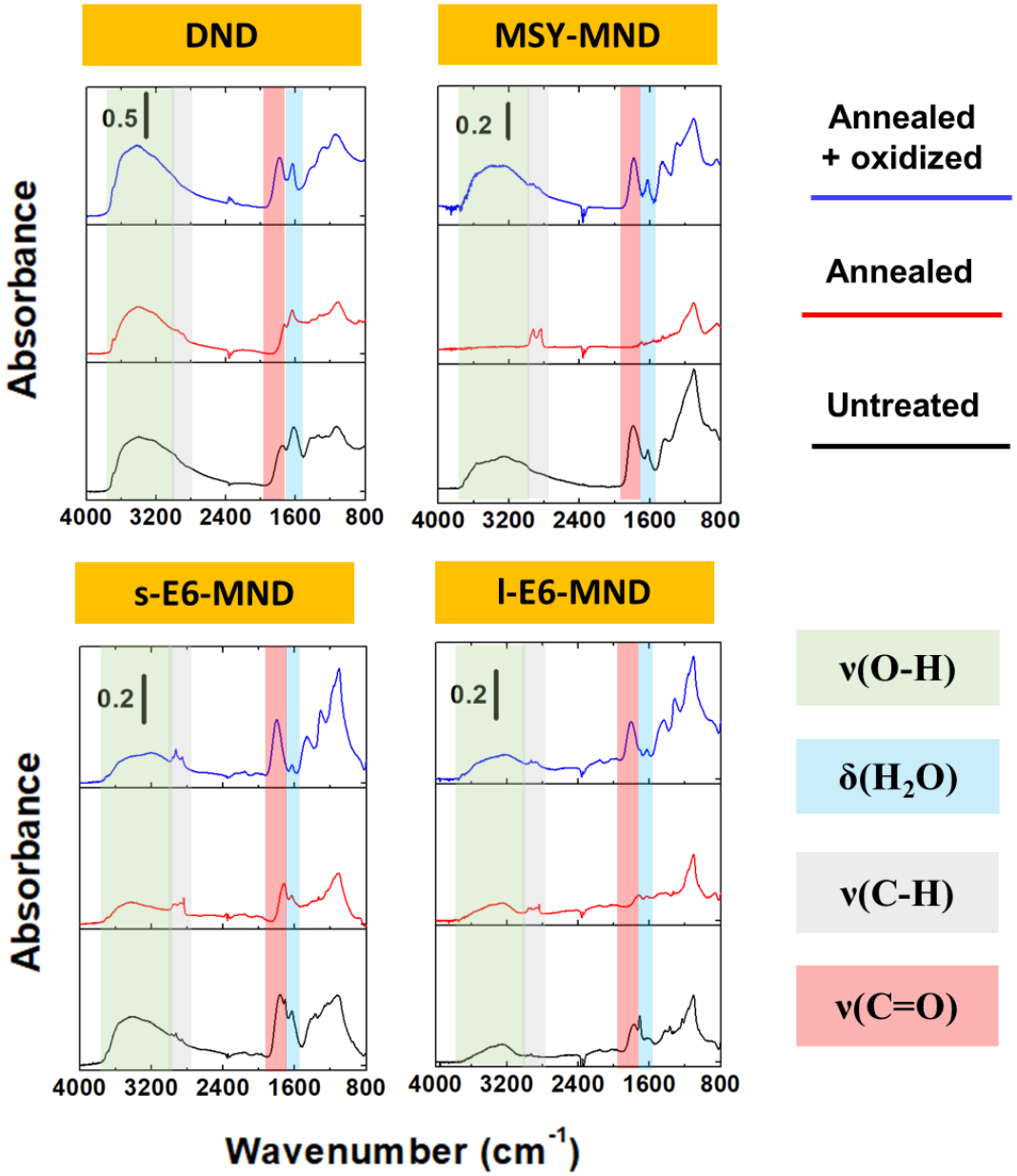

Figure 49: DRIFT spectra for all samples acquired in controlled atmosphere at room temperature.

Untreated ND presented a broad absorption band in the region 3650-3000 cm^{-1}, which can be ascribed to the ν(O-H) stretching modes of hydrogen-bonded water molecules adsorbed on the surface of ND (red band). Their presence is furtherly confirmed by the δ(H_2O) bending mode

observable around 1630 cm^{-1} (light blue band) [160,161]. Low-intensity signals ascribable to ν(C-H) stretching are present in the 3000-2800 cm^{-1} range (grey band), in overlap with the ν(O-H) band. C=O stretching absorption bands are visible in the 1800-1720 cm^{-1} spectral region, which can be ascribed to many different forms such as carboxylic acids, lactones, esters, acid anhydrides, etc. [162]. The spectral region below 1500 cm^{-1}, shows a complex overlap of absorption bands. This IR region is generally of difficult interpretation, as it contains signals arising from a wide variety of functional groups. Nonetheless, these bands can be mostly attributed to ether/ester-like (C–O–C/C–O) groups [162], in particular for the bands between 1200 cm^{-1} and 1000 cm^{-1} [163]. The various ND sizes and the respective aggregation prevents an adequate quantitative analysis of the diffuse reflectance IR spectra. Nonetheless, as a general trend, it can be inferred that the absolute intensity of the IR signals for the different samples is correlated with the nanoparticle sizes (and the respective surface area), following the order DND > MSY-MND > s-E6-MND > l-E6-MND.

In the spectra acquired following HTTA, significant removal of oxygenated groups is suggested by the decrease of the C=O band and by the downshift of its signals toward lower wavenumbers. In parallel, C-H absorption bands resulted increased, as evident by the appearance of two peaks at 2950 cm^{-1} and 2886 cm^{-1}, which are respectively associated with asymmetric and symmetric stretching vibrations of CH_3 groups [164]. After the air oxidation process, the C=O groups contributions rise again, while removing C-H groups, consistently with what was observed in previous studies [160].

As already discussed, surface chemistry has a relevant influence on the hydrophilicity profile. This property can be evaluated by considering the intensity of the δ(H_2O) and ν(O-H) modes, which are generally more intense in the cases of untreated and oxidized samples. For a deeper comprehension of the surface water adsorption mechanism, a DRIFT analysis was conducted exemplarily for DND under controlled atmosphere and following progressive dehydration. More precisely, DRIFT spectra were collected while exposed to air, in vacuum (residual pressure < 10^{-2} mbar) and at increasing temperature up to 400 °C. The set of acquired spectra is shown in Figure 50a. As the temperature increases, δ(H_2O) and ν(O-H) bands gradually decrease, due to the removal of adsorbed water molecules, also allowing for better visibility of C-H signals which become particularly clear in spectra of annealed DND collected at 400 °C. Although O-H stretching band contain the contribution of physiosorbed water, this feature is also associated with possible O-H

surface terminations, thus explaining the significant residual signal still visible at 400 °C (especially for oxidized DND), when almost complete desorption of water is expected. On the contrary, $\delta(H_2O)$ mode around 1630 cm^{-1} is peculiar of water molecules and, for better quantification of the phenomenon, its signal was integrated after proper baseline subtraction. The obtained data are reported in Figure 50b. As can be observed, the hydrophilicity follows the order annealed + oxidized > untreated > annealed DND, in agreement with the more favorable hydrogen bonds formation between water molecules and surfaces richer in oxygenated groups. The results suggest that water molecules, which in environmental conditions form a surface multilayer, are almost completely released around 200 °C.

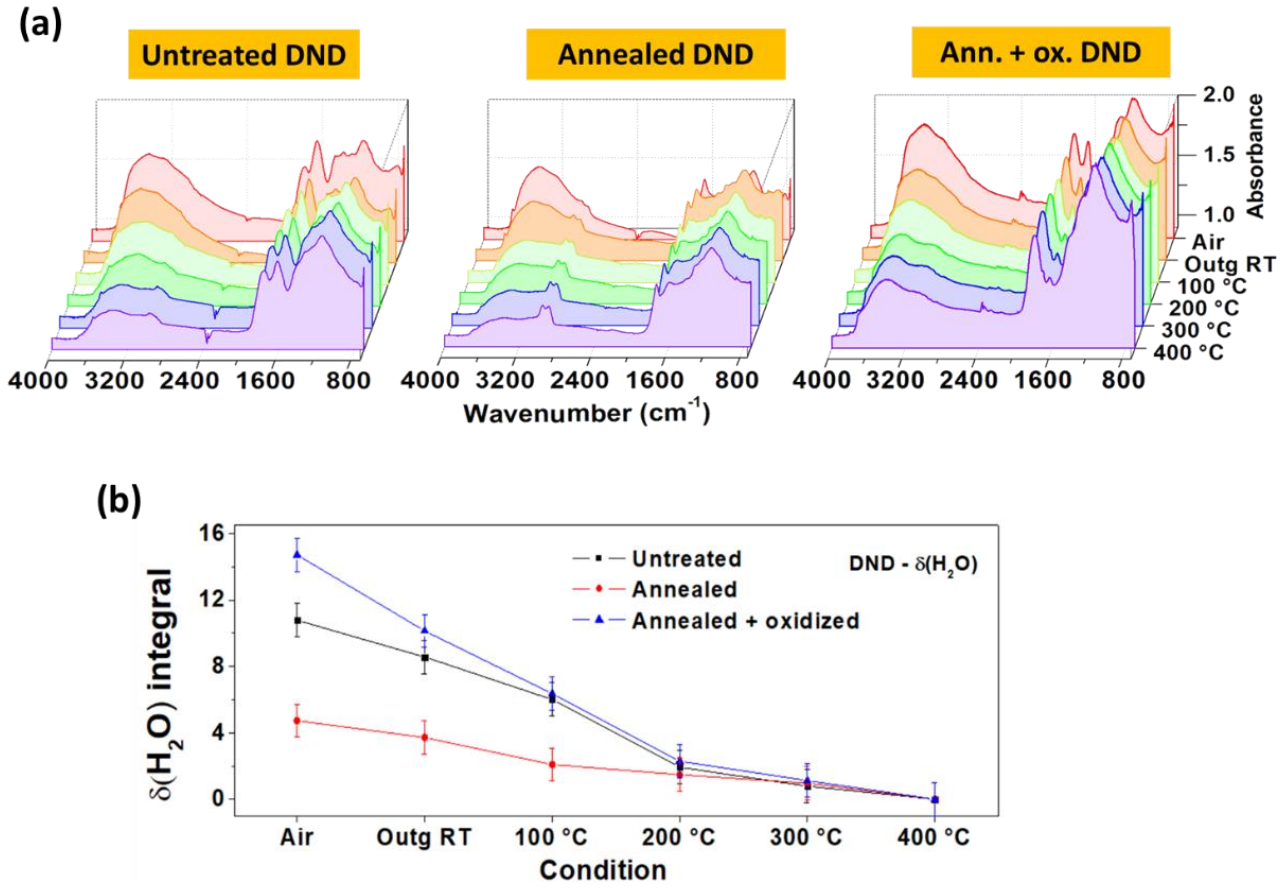

Figure 50: (a) DRIFT spectra for DND acquired in air environment, after outgassing at room temperature (< 2 mbar, ~25 °C) and at increasing temperature (up to 400 °C); (b) integral of H_2O bending signal as a function of the environmental condition.

Overall, the evidence provided by DRIFT analysis is consistent with DLS data, as the low hydrophilicity of annealed samples is responsible for the higher aggregation level in an aqueous environment, while the rich oxygen content of oxidized and untreated samples allows for a higher

surface charge and better dispersibility. Finally, it is also worth focusing the attention on the relationship between surface charge and the DRIFT bands related to oxygenated groups. Concerning the latter, DRIFT spectra of DND clearly presented higher signals with respect to MND samples, while Z-potential resulted more intense in the MND case. Nonetheless, this result is not contradictory, as the DRIFT absorption bands are to be interpreted by considering the wider surface-to-volume ratio of DND. Combining this consideration with the stronger surface Z-potential of MND, a surface denser of oxygen-containing groups is suggested for them with respect to DND [165].

Electrical characterization

As discussed in section 1.6.2, water adsorption determines the surface conductivity of ND. Current-voltage (I–V) characteristics were thus collected to evaluate the effect of the thermal processes on the electrical properties of ND. Firstly, NDs were "reset" to a starting condition by heating them on a thermal plate in air at 120 °C for 15 min, thus allowing the desorption of bonded water molecules. The powders were then exposed to a controlled environment with constant temperature (21 ± 1) °C and two different humidity values (h_1 = (32 ± 2) % or h_2 = (61 ± 2) %). I-V curves were acquired both immediately after heating and 15 hours after the exposure to the above-mentioned conditions. In the first case, all ND did not show any measurable conductance, presenting currents lower than 1 pA at 20 V, thus settling below the sensitivity of the electrometer and suggesting a residual content of water molecules too low to allow conduction. Following the exposure to h_1 conditions for 15 hours, I-V curves were acquired, showing an ohmic behavior in the explored range of voltages (Figure 51a reports exemplarily I-V characteristics for DND). The resistance values of all the samples are shown in Figure 51b. E6-MND powders showed comparable resistances, which ranged between 10^{10}-10^{11} Ω, while MSY-MND and DND presented a higher conductivity. Overall, in accordance with the stronger hydrophilicity evidenced by DRIFT spectra, oxidized and untreated samples showed a lower resistance with respect to the annealed ones. A peculiar exception is observed for oxidized DND, with a resistance value resulting >10^{10} Ω. Under the exposure to the higher humidity condition h_2 (Figure 51c), untreated and annealed DND presented 2 orders of magnitude decrease in resistance. Similar tendencies are obtained for untreated and oxidized MND, whereas annealed E6-MND did not present any enhancement of the Grotthuss mechanism conduction, sticking around resistances of 10^{11} Ω. Unexpectedly, oxidized DND showed a higher resistance with respect to the other DND samples. Nonetheless, they presented the most relevant decrease (~ 3 orders of magnitude) in resistance when passing from ~30% to ~60% relative humidity conditions, suggesting a marked increase in water adsorption at

increasing humidity. This result, coupled with the intense δ(H_2O) absorption signal observed in DRIFT spectra (Figure 50), hints that the reason underlying this issue might be related to structural differences. Raman spectra reported in Figure 47 evidenced for untreated and annealed DND a rich graphitic content, whose high conductivity might have played a crucial role. Oxidized samples, due to the removal of a relevant amount of sp^2 components, have probably lost this contribution, which is then partially compensated by the Grotthuss mechanism in the higher hydration condition.

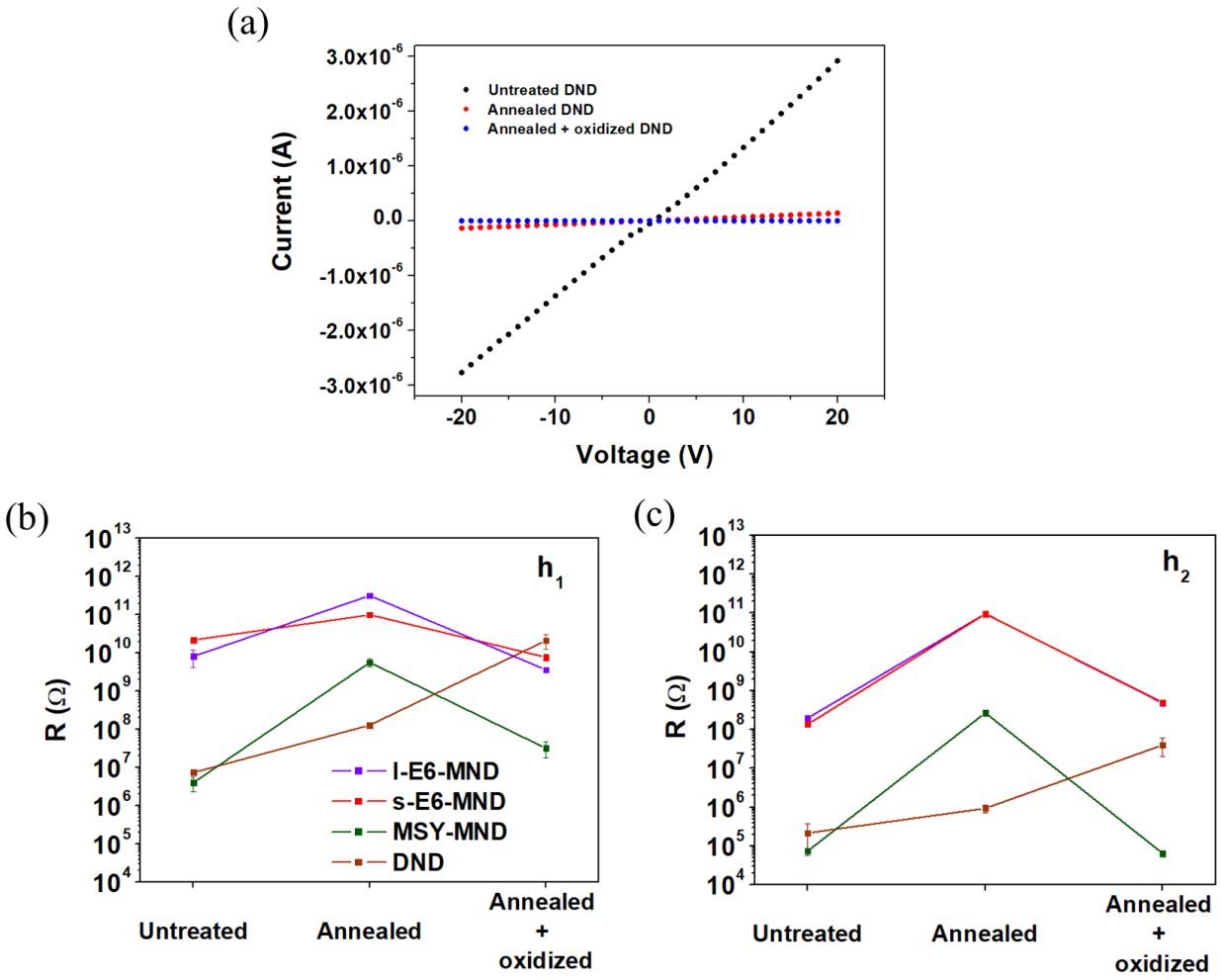

Figure 51: (a) I-V curves reported exemplarily for DND at h_1 conditions; (b) resistances values calculated from I-V curves for all samples at ~30% and (c) ~60% of relative humidity.

3.2.2 Oxidation

In the previous paragraphs, it has been shown how oxidation has positive effects in terms of stability in an aqueous environment, surface purification and fluorescence properties, thus suggesting them as preferable candidates in contexts such as drug delivery and biolabeling. In this section, a more in-depth analysis of the effect of different conditions of air oxidation is presented. Due to their size range of major interest for biomedical applications, MSY-MND were selected for

this investigation. More precisely, along with the activity of the candidate, two campaigns of systematic oxidations and subsequent characterizations were performed:

a) mildly oxidative air thermal processes with temperatures varying between 400 °C, 450 °C and 500 °C and exposure times of 30' and 1 h.
b) aggressive oxidative air thermal processes carried 450 °C, 475 °C, 500 °C and 525 °C with exposure times of 3 h, 6h, 12 h, 24h, 36 h and 48 h.

Before oxidation, in both the above-mentioned cases, MSY-MND were annealed at 800 °C for 2 h in N_2 inert environment.

Mild oxidation

Thanks to the control of temperature and dwell time, air oxidation treatments can be used to tune the oxidizing degree of ND surface. With this purpose, annealed MSY-MND were selected for being subjected to mild oxidative thermal processes varying both the temperature (between 400 °C ad 500 °C) and the exposure time (30' – 1 h). Treated samples were then analyzed by DRIFT spectroscopy, as reported in Figure 52.

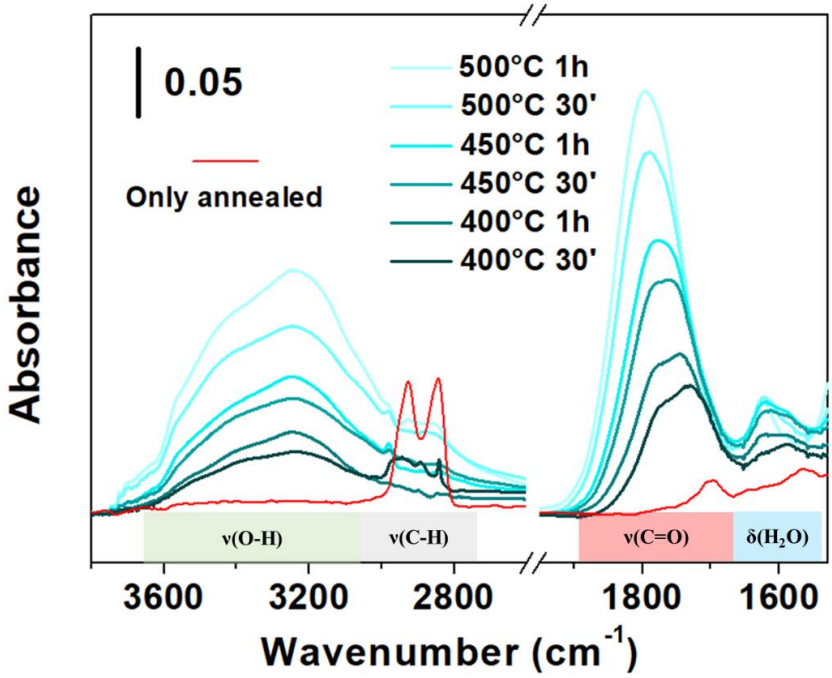

Figure 52: DRIFT spectra for annealing + oxidized samples with different temperature and process time parameters.

O-H and C=O stretching modes resulted gradually enhanced as the temperature and processing time were increased. Similar behavior is observed for $\delta(H_2O)$ mode, confirming the general tendency toward better hydrophilicity at increasing oxidation levels. C-H stretching signals, present in high quantity in annealed samples, were still observable for weak oxidation conditions (400 °C for 30 minutes), while completely disappeared just doubling the oxidation time at the same temperature. It is worth noting how ν(C=O) band at lower oxidation temperatures and times is peaked around 1730 cm^{-1}, while as the oxidation level is increased, the band shift towards 1795 cm^{-1}. These two positions can be related to C=O groups in the form of carboxyl acid/aldehydes groups and lactones/anhydrides terminations, respectively [162]. Figure 53 schematizes a simplified example of the hypothetical process occurring as the oxidation proceeds: at the beginning, the mild oxidations allow the formation of a gradually increasing number of simpler oxygen-containing structures such as carboxylic/aldehydes/esters C=O groups on the surface on ND, giving rise to the peak around 1730 cm^{-1}. As the process becomes more aggressive, the density of these species increases, until condensation reactions between the groups occurs, thus covering the surface with more complex structures such as anhydrides and lactones, whose absorption bands are peaked at higher wavenumbers. In parallel, OH groups (from carboxylic acids or simple hydroxyls) are also formed, determining, together with adsorbed water, the stretching band around 3000 cm^{-1} – 3600 cm^{-1}.

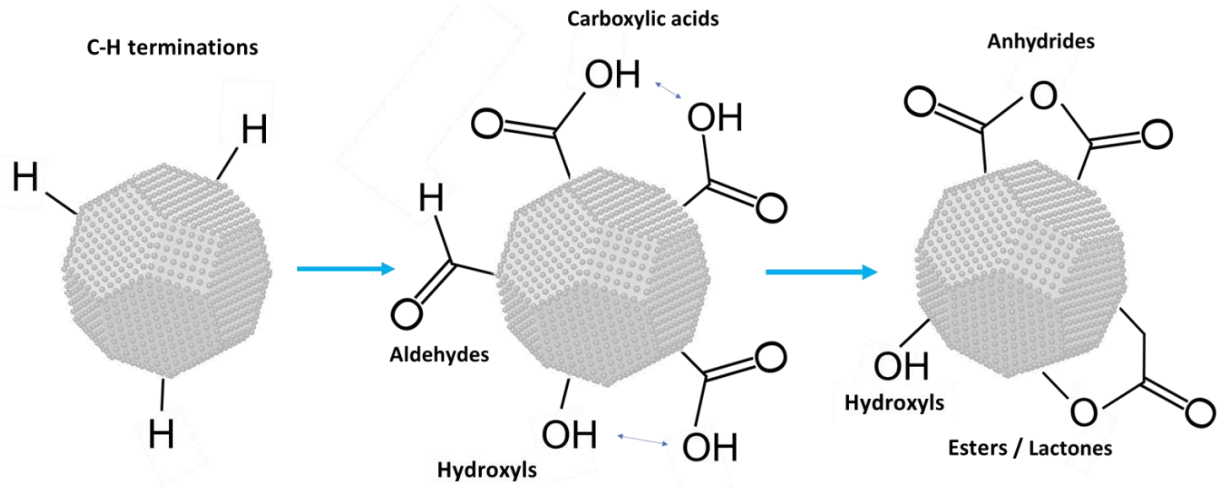

Figure 53: simplified schematic of some of the various possible processes occurring on ND surface upon oxidation. Starting from simpler chemical groups (such as aldehydes and carbonyls), surface functionalities are then converted to carboxylic acids, which in turns, when a high density is reached, condensate to form more complex structures such as anhydrides, esters and lactones. Contemporarily, OH groups are created in increasing quantity (as evidenced by the stretching band from 3000 cm^{-1} to 3600 cm^{-1}).

A more quantitative evaluation of the influence of the different oxidation conditions can be done by comparing the variations in the signal intensities in terms of temperature or time variations. Indeed, from Figure 52 it is noticeable how the increase in temperature of 50 °C determines a stronger increase in the general C=O band with respect to an increase in time of 30 minutes. A similar behavior, although slightly less pronounced, is observed for ν(O-H) vibrations, thus suggesting a more effective influence of temperature in the surface oxidation degree.

To assess the effect of the oxidation treatments also on the structural and fluorescence properties, Raman/PL spectra were acquired at the different oxidation steps (see Figure 54). Similarly to spectra shown in section 3.2.1, the first-order Raman diamond peak is observed at 1320 cm^{-1} (572 nm). The presence of graphitic contaminations, despite the oxidation, is confirmed by the presence of D- and G-bands around 1360 cm^{-1} (573.5 nm) and 1584 cm^{-1} (590 nm), respectively. As already observed for oxidized ND, also for these mild oxidations the intensity of the NV centers emission band, between 580 nm and 780 nm, results enhanced as the oxidation level is increased, again with a more decisive effect of a 50 °C increase in temperature with respect to further 30 minutes of treatment. Nonetheless, the moderate increase in fluorescence and the absence of significant differences in the G-band intensity as the time and temperature of the process increase, suggests that a better surface purification of ND can be achieved with more aggressive oxidation treatments.

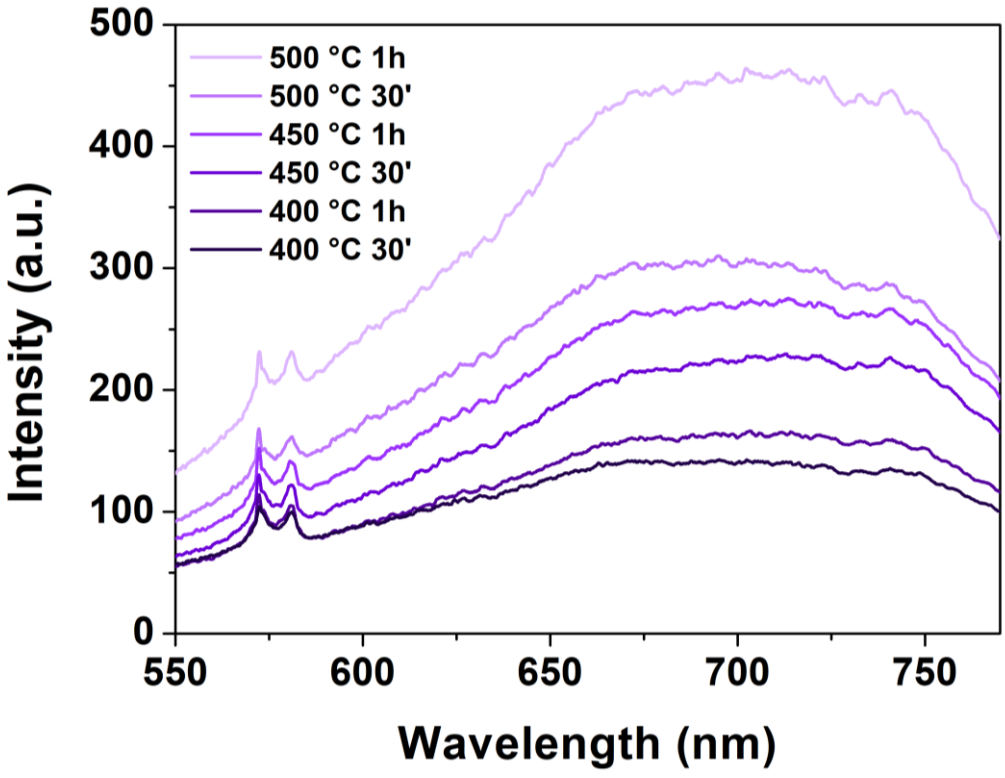

Figure 54: PL spectra of mildly oxidized ND

Aggressive oxidation

In order to explore the influence of more aggressive oxidation treatments on surface properties and to define a protocol that maximizes their PL, a second campaign of processes and characterizations was performed. Therefore, annealed MSY-MND were oxidized in air environment from 3 h up to 48 h, with temperatures ranging between 450 °C and 525 °C.

Once prepared, DRIFT analysis was thus conducted on these samples. A representative selection of the obtained spectra is reported in Figure 54 for treatments of 3 h and 48 h - variable temperature (Figure 55), and at 450 °C and 525 °C - variable process time (Figure 56).

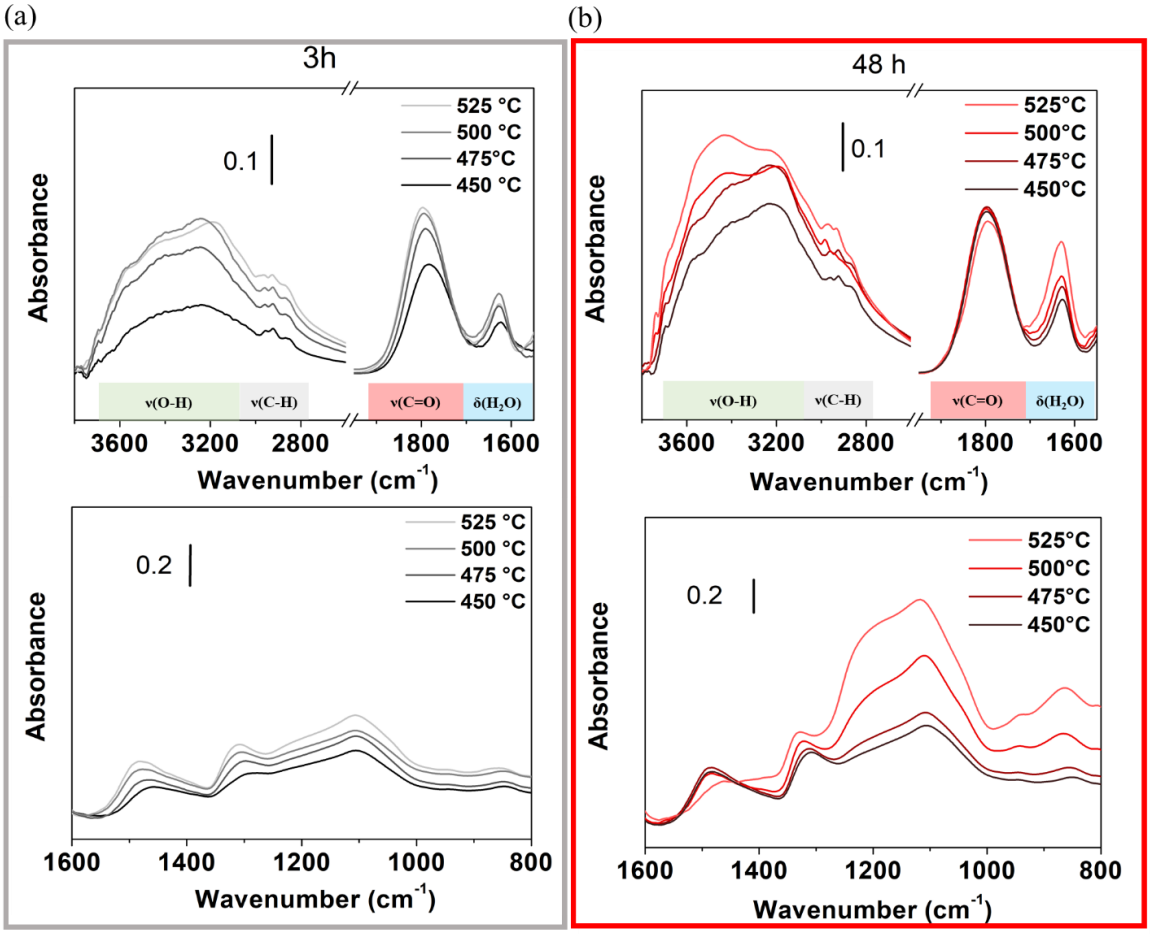

Figure 55: DRIFT spectra of MSY-MND oxidized for 3h (a) and 48h (b) at variable temperatures

As expected, higher temperatures determined a general increase in oxygen-containing functional groups absorption features. At lower processing times (3 h), a gradual enhancement of both C=O and O-H stretching bands is observed, while H_2O bending associated with water adsorption is only weakly increased. Similarly to what was obtained in the previously described mild oxidations, a shift of ν(C=O) towards higher wavenumbers is evident. Oppositely, at 48 h, as the temperature rises no significant differences are observed in C=O vibrations, probably because at long

processing time the maximum functionalization with carboxylic and anhydrides groups is already reached independently of the temperature (in the investigated range). $\delta(H_2O)$ modes are instead gradually increased with temperature also at long treatment times.

Besides a general enhancement of the O-H stretching band, in this region, a progressively higher absorption signal – particularly starting from 500 °C - emerges around 3450 cm^{-1}, which is more specifically ascribable to O-H stretching in water molecules. These observations suggest higher hydrophilicity which occurs mainly at highly aggressive oxidation conditions (high temperature for a long dwell time). Interestingly, C–O vibrational modes between 1300 cm^{-1} and 1000 cm^{-1} showed very similar behavior, thus representing a possible hydrophilic substrate for the observed relevant water adsorption.

Spectra at constant temperature and variable times (Figure 56) provides consistently similar evidence. At low temperature (450 °C), longer oxidation times increased all oxygenated species.

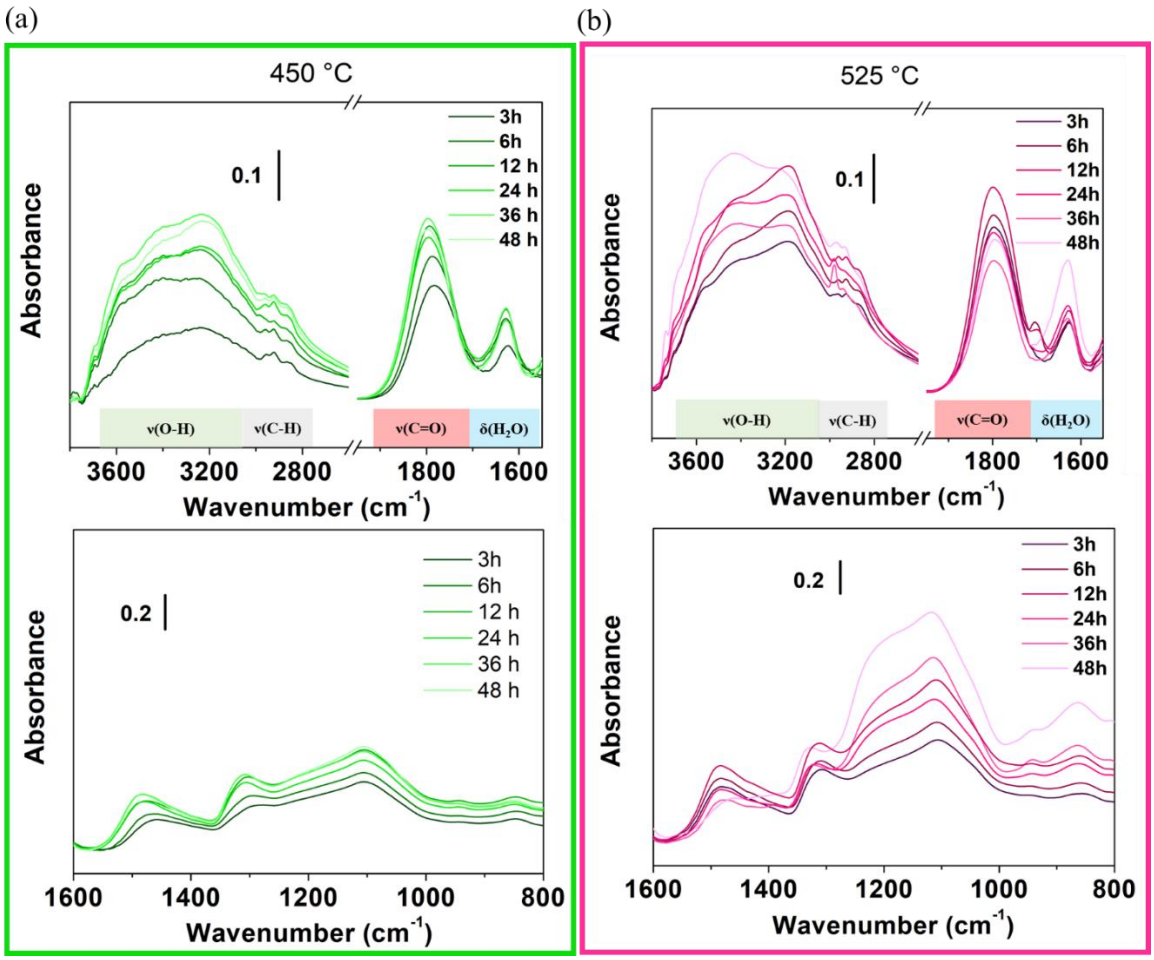

Figure 56: DRIFT spectra of MSY-MND oxidized at 450 °C (a) and 525 °C (b) at variable process times

Also $\delta(H_2O)$ rises, but not the water-related ν(O-H) band at 3450 cm^{-1}, which stands out only after oxidations at temperatures above 500 °C, when also C-O groups are drastically enhanced.

The other spectra following oxidations at 475 °C and 500 °C are reported in Appendix A.

In summary, by combining the information obtained from DRIFT spectra of both mild and aggressive oxidations, it is possible to conclude that:

- low temperatures and process times (see "Mild oxidations" paragraph) determine the formation of surface OH groups and C=O species, particularly in the forms of carboxylic acids, aldehydes and esters. As a consequence, hydrophilicity is gradually enhanced;
- intermediate aggressive conditions further increase carboxylic, and more generally C=O, groups, promoting also the development of anhydrides and lactones;
- since C=O groups have already reached their maximum, high temperatures and process times are mainly effective in increasing ether/ester-like (C–O–C/C–O) groups species, which might have been determining in the instauration of the observed better hydrophilicity.

In the following section, Raman/PL analysis of these samples is presented. As the main purpose was to assess the effect of the oxidation on PL intensity, the NV centers fluorescence band was integrated between 565 nm and 780 nm. Results are reported in Figure 57a.

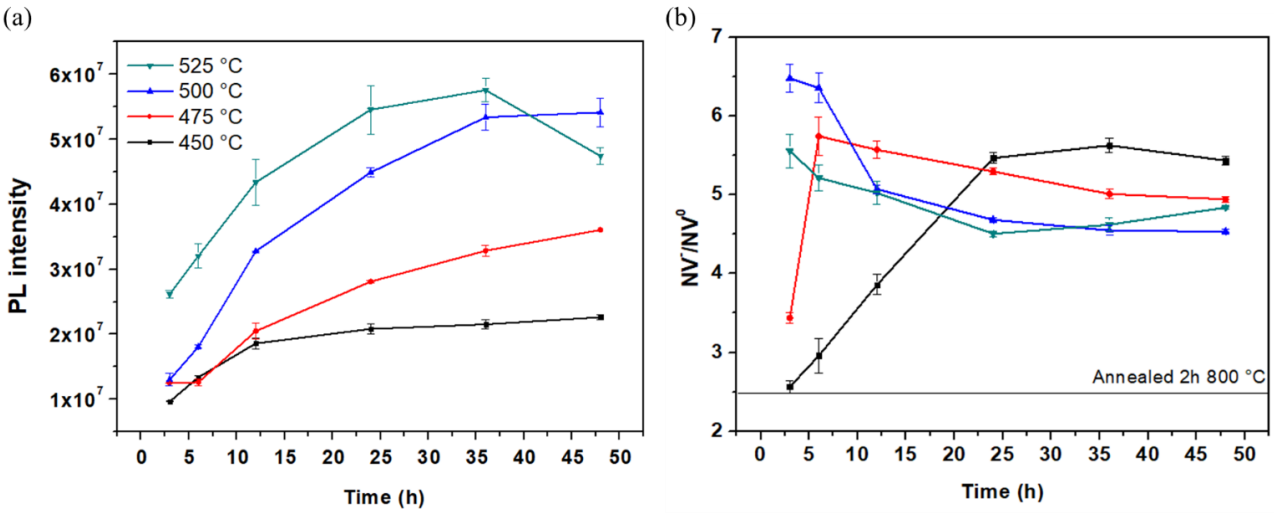

Figure 57: Integral of NV centers PL intensity (a) and NV^-/NV^0 ratio (b) as a function of oxidation temperature and time.

In general, as the oxidation temperature and time increase, the more aggressive purification determine a higher fluorescence yield. When passing from 36 h to 48 h of process, a flattening of the trend is observable at 500 °C, while a slight decrease is registered at 525 °C. Indeed, previous work demonstrated that at temperatures above 500 °C also the diamond phase can be affected and

a sensible reduction in the nanocrystal volume/or mass might have occurred [154]. This fact was confirmed with TEM images acquired on annealed MSY-MND following oxidation for 12h at 450 °C and for 48 h at 525 °C and reported in Appendix B. NV^-/NV^0 ratio was also evaluated by calculating $I_{700\,nm}$ / $I_{575\,nm}$ (in the implicit form of $a\frac{NV^-}{NV^0} + b$, due to the overlap of the two signals) and plotted in Figure 57b. Carefully observing the trends, an increase in the ratio occurs at lighter oxidation conditions (i.e.: at 450 °C as the processing time increases or 475 °C for low process time), in accord with the increase in NV^- centers due to surface oxidation (see section 1.4.4). More precisely, the effect is associated with the positive dipole moment formed between carbon and oxygen atoms, which in the proximity of the surface determines the bending of the level structures, thus favoring NV^- centers. Surprisingly, intermediate oxidations seem to play an opposite role by slightly decreasing this ratio. Although the reason for this phenomenon is not completely clear, a possible explanation can be associated with the progressive formation of a different variety of oxygenated moieties. More precisely, it has been shown before that exactly in correspondence of intermediate oxidation temperatures and process times, the transition from isolated C=O surface groups to more complex and interconnected structures, such as anhydrides and lactones, might occur. As exemplified in Figure 58, due to the possible presence of opposite dipole moments, this kind of chemical groups can present a net dipole that is lower respect to that of single carboxylic acids or carbonyls present in DRIFT spectra of mildly oxidized ND, thus potentially explaining the partial decrease in the NV^-/NV^0 ratio.

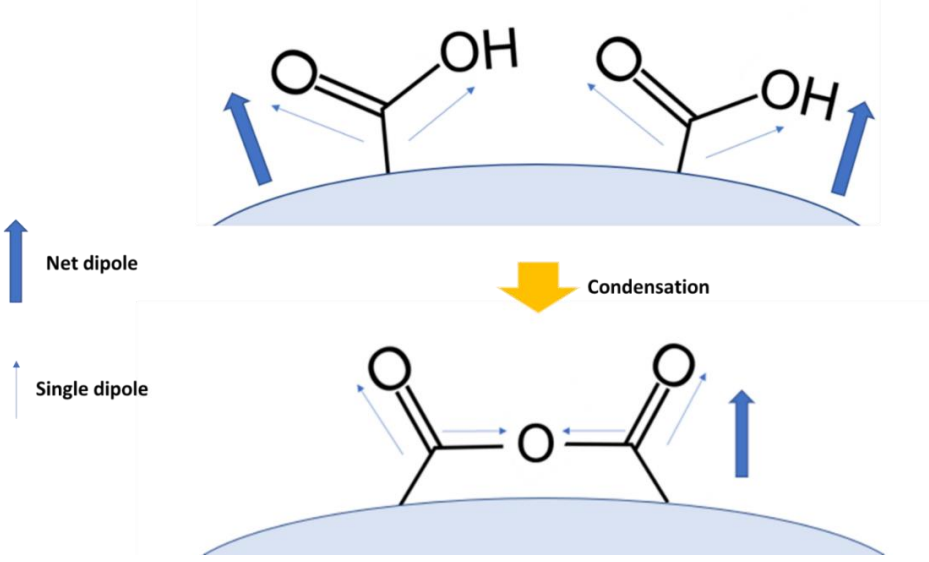

Figure 58: schematics of the dipole moment of surface C=O groups. As can be evinced in this example regarding the condensation of carboxyl acids into anhydrides, the formation of such complex structures can reduce the net dipole moment. Similar phenomena can occur in the formation of lactones or esters.

Other alternative explanations could be attributed to the gradual removal of surface contaminations which might have a quenching effect more pronounced on NV^0 centers with respect to NV^-, or the water interaction with the surface chemical bonds which might also slightly reduce the dipole moment of surface oxygenated groups. Elsewise, the gradual etching of surface graphite, as the oxidation level increased, might have reduced the thermal heating of the ND under laser irradiation during the PL analysis [82], thus decreasing the ratio [166].

Finally, at 525 °C for oxidation time > 24 h, the ratio slightly increases again, probably due to the reduction in the crystals dimension. Consequently, the larger surface area, being oxidized, might favor a further increase in NV^- centers. In addition, the strong increase in C-O species observed in DRIFT spectra at such high temperatures and times, by augmenting the general surface oxidation status, could have promoted a further increase in NV^- centers.

3.2.3 Hydrogenation

In the first chapter, the potential application of hydrogenated ND for the enhancement of free radical generation in radiotherapy has been discussed. Pushed by the promising data already published, the research group decided to start investigating this interesting surface termination.
Since the hydrogenation process on nanodiamonds was never attempted before by the solid-state physics group of the University of Torino, only preliminary data concerning s-E6-MND are shown. Figure 59 summarizes the processes that were carried out. Other comparative samples were prepared to verify the difference in the assessed properties.

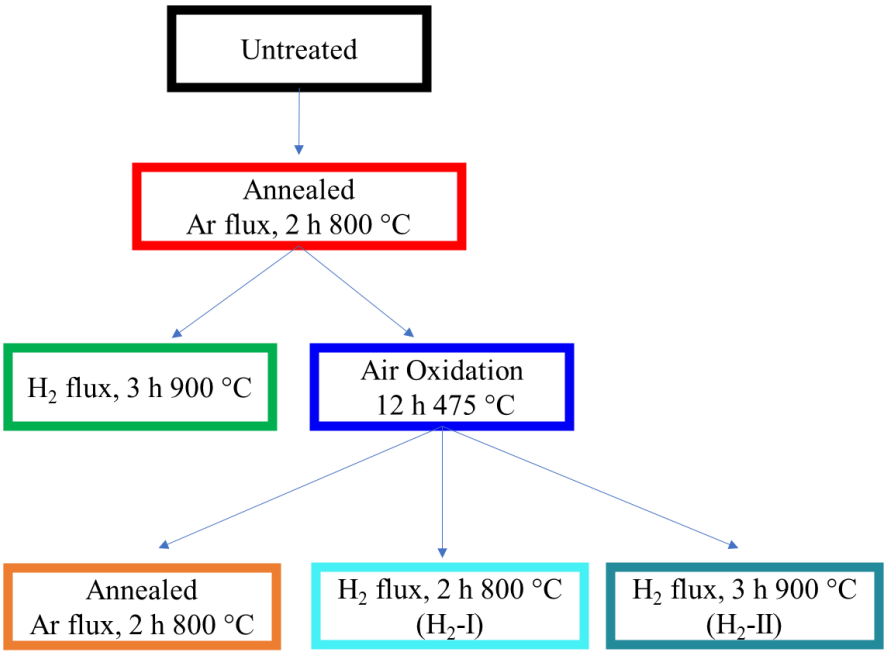

Figure 59: processes carried out on s-E6-MND

All the samples at each treatment step were characterized both with electrical measurements and DRIFT spectroscopy. Similarly to the measurements presented in section 3.2.1, ND powders were firstly heated at ~120°C for 30 minutes allowing the complete desorption of water. Afterwards, the powders were kept at a relative humidity h = (32.6 ± 0.8) % for 18 h. Figure 60 reports the resistance values obtained from the I-V curves. *Untreated* and *ann. + ox.* samples showed similar conductivity, while annealed ones presented slightly higher resistance, in accord with data shown in 3.2.1. Conversely, all hydrogenated ND presented a marked decrease in resistance. The results are thus in line with the expectations discussed in 1.6.2, as the lower resistance of hydrogenated samples can be attributed to the transfer doping mechanism [127]. Due to the previous removal of surface contaminations, the resistance drops more significantly when the hydrogenation process is performed following purification by air oxidation. The successful hydrogenation is also confirmed by the high resistance of *ann.+ ox. + ann.* ND, as the final re-annealing at the same dwell time and temperature conditions (but different gas) determined a completely different effect on the electrical properties.

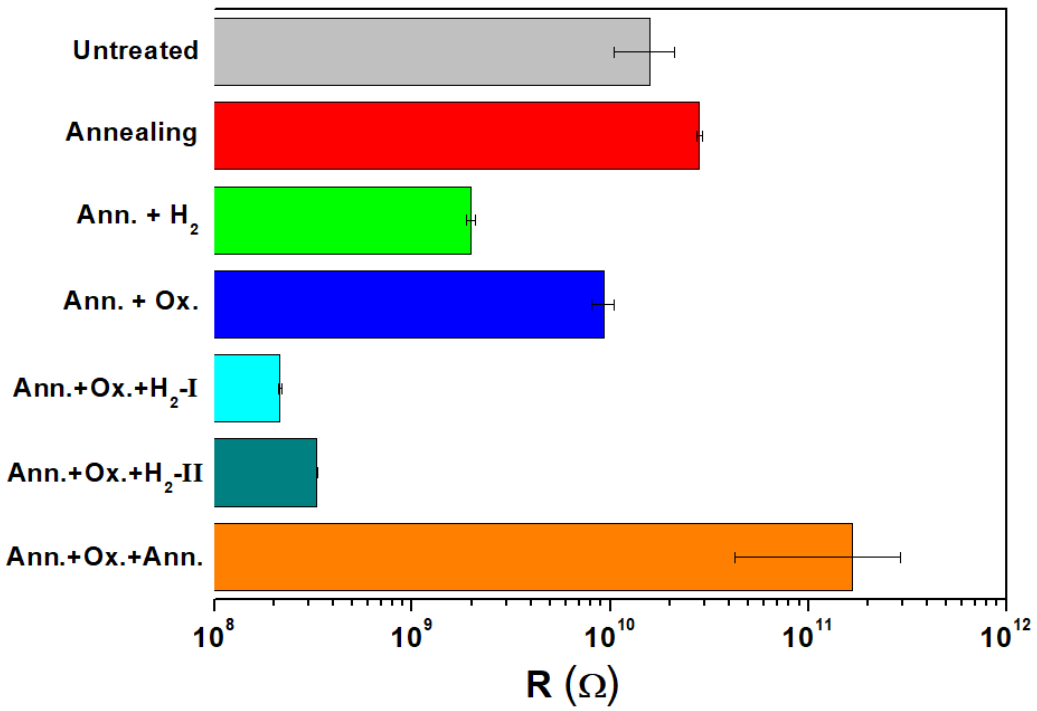

Figure 60: resistance values calculated from I-V curves of s-E6-MND at controlled humidity conditions h= (32.6 ± 0.8) %.

However, as anticipated in the introduction, it is worth recalling how the model of transfer doping is basically referred to bulk diamond. Nonetheless, the presented results, consistently with the observations of a previous work on ND [127], seem to validate this effect also in the case of ND

powders. The transfer doping mechanism is probably directly involved in an easier conduction in the single ND, while, when passing from one ND to the other, indirect effects of this mechanism might occur, such as the increase in the number of electrons present in the surface water layer (see Figure 21) or the movement of electrons (at the basis of holes conduction) between the ND grain borders.

To further confirm the success of the process, DRIFT spectroscopy was carried out to characterize the surface chemistry of ND. Spectra are reported in Figure 61, resulting for untreated, annealed and ann. + ox. samples in line with what was reported in paragraph 3.2.1.

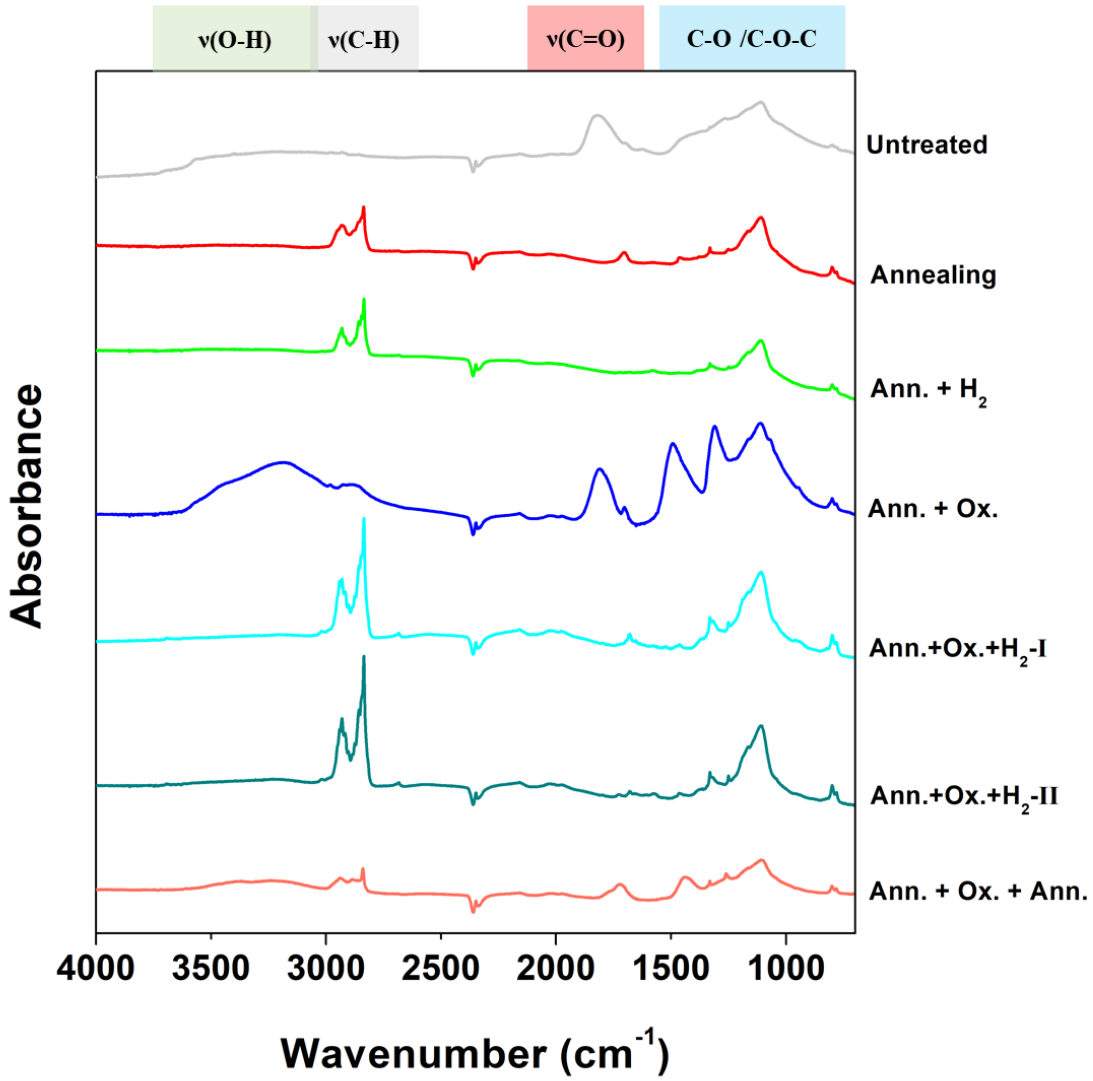

Figure 61: DRIFT spectra of s-E6-MND treated as schematized in Figure 56.

With respect to oxidized ND, in the spectrum of *ann.+ ox. + ann.* ND both ν (C=O) (around 1800 cm^{-1}) and ν(O-H) (3650–3000 cm^{-1}) modes were reduced, while a mild enhancement of

ν(C-H) signal is registered between 2990 cm^{-1} and 2800 cm^{-1}. Also, a decrease of C-O signals at low wavenumbers is observed. Hence, in general, the further annealing of the *ann. + ox.* samples restores the surface termination of the annealed ones, with a consequent hydrophobicity that prevents water adsorption and the occurrence of Grotthuss conduction mechanisms. The success of the hydrogenation process is guaranteed by the emergence of a strong ν(C-H) absorption band in the spectra of *ann. + H_2* and, more markedly, *ann. + ox. + H_2-I* and *ann. + ox. + H_2-II* samples, thus confirming more effective hydrogenation when carried out after oxidation. Other absorption bands signals resulted very similarly to the case of annealed samples, with the general decrease or disappearance of signals related to oxygen-containing groups, with a detrimental effect on surface hydrophilicity. Despite this, even a very thin layer of water can be sufficient to allow the transfer doping mechanism to occur, thus providing the significant resistance drop reported in Figure 60.

3.2.4 Ion implantation of nanodiamonds

Due to their characteristics, MSY-MND were selected for the fluorescence enhancement by means of ion beam techniques. Indeed, these nanocrystals are small enough to be interesting for biolabeling applications and at the same time can guarantee the presence of a sufficiently large crystalline diamond core to contain a good amount of NV centers.

As introduced in section 1.5.2, due to the low number of vacancies naturally occurring in the ND lattice, only a minor fraction of the substitutional nitrogen atoms is coupled with these vacancies forming NV centers. Hence, ion-induced damaging is necessary to increase the vacancy density and consequently, after the thermal activation, the total amount of luminescent NV centers. To this purpose, annealed + oxidized samples (N_2 flux 2h 800 °C + air exposure 8h at 450 °C, as presented in section 3.2.1) were subjected to the ion-implantation process to create new NV centers. After dispersing the ND in isopropyl alcohol obtaining a dense solution, a couple of drops were deposited on a silicon wafer square (~ 1 × 1 cm^2) and dried under a light thermal source. As a result, a compact ~ (33 ± 10) μm thick layer of ND was obtained. The thickness and its variability were evaluated via SEM microscopy (see Figure 62a). The samples were then implanted with a broad (5×5 mm^2) 2 MeV H^+ ion beam at the AN2000 accelerator facility of the INFN National Laboratories of Legnaro (INFN-LNL, see paragraph 2.2), with a beam current varying between 670 - 700 nA. With the purpose of studying the trend of the ND fluorescence at different ion-damage levels, multiple depositions were implanted at different fluences ranging from 1.5×10^{14} cm^{-2} up to 1.5×10^{17} cm^{-2}, thus keeping sufficiently below the graphitization threshold of implanted diamond. The delivered fluence was estimated from the integrated charge collected by a Faraday cup positioned inside the

irradiation chamber. The total delivered charge is then divided by the charge of the proton ($e = 1.6 \times 10^{-19}$ C) and by the beam area.

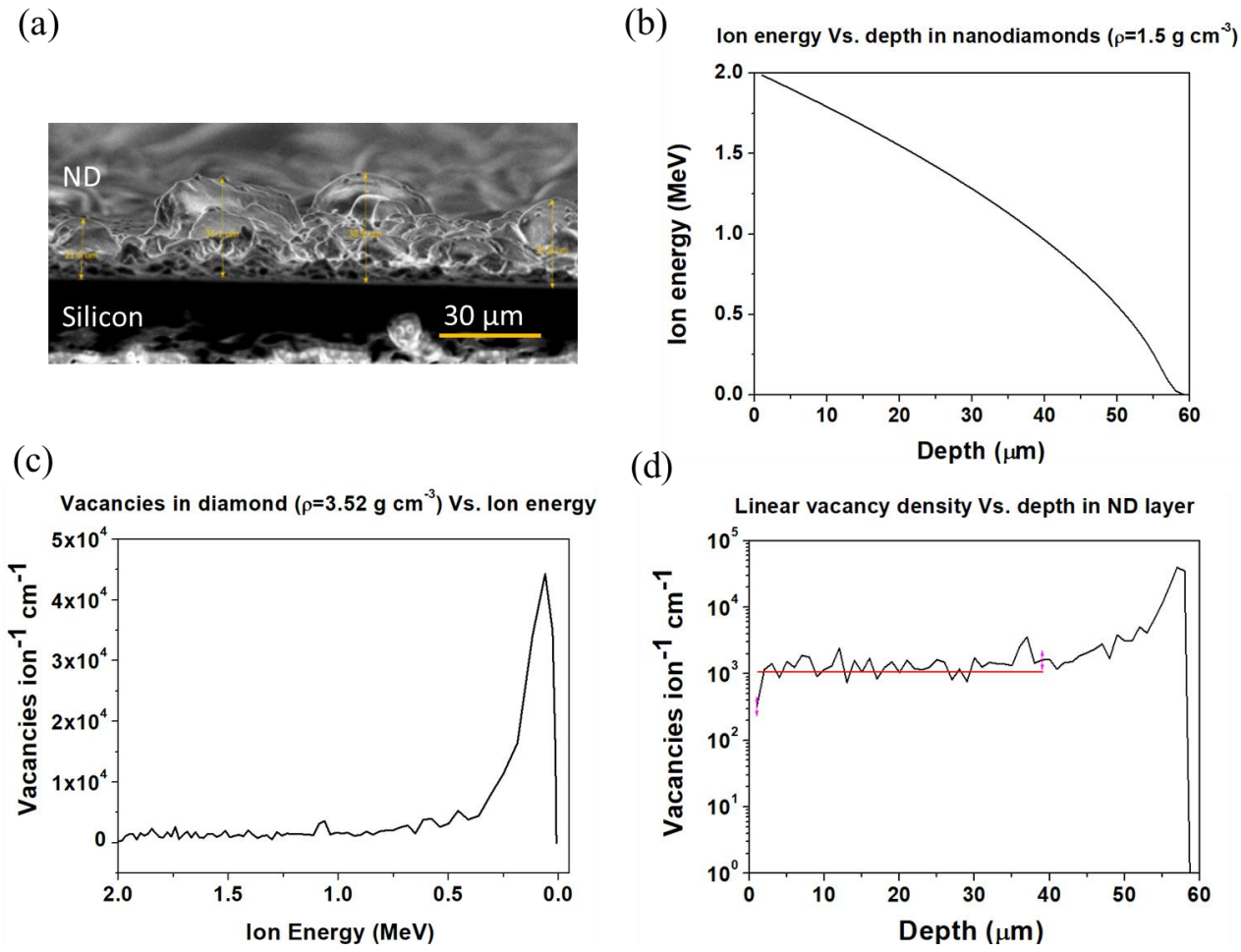

Figure 62: (a) thickness estimation by SEM of the deposited ND layer over the silicon substrate; (b) energy of protons as a function of the depth in the ND layer (simulated with ρ_{powder}=1.5 g cm^{-3}); (c) linear vacancy density per ion of protons in diamond (simulated with ρ_{bulk}=3.52 g cm^{-3}) as a function of their energy; (d) linear vacancy density per ion realized in the ND layer as a function of the depth, obtained by calculating the function interpolated from graph (c) at the energy values of graph (b).

To evaluate the effect of the implantation, a Monte Carlo simulation was carried out using SRIM software. In addition to the implantation parameters already described, in this case the setting of the material density required more attention, since it is important to take into account the powder nature of the sample. For this reason, while the density of bulk diamond is about 3.52 g cm^{-3}, due to the spaces occurring between adjacent nanocrystals, the powder density will necessarily exhibit a lower value. In order to estimate it, a 10 ml graduated cylinder was filled with the compressed powder. Measured the contained mass, an effective density of ~1.5 g cm^{-3} was obtained. Running

the simulation with this value, the energy of the impinging protons as a function of the depth in the ND layer was obtained (Figure 62b). Nonetheless, protons entering each single nanocrystal create a damage level equal to that which would be realized in monocrystalline diamond. The estimation of the linear vacancy density introduced in bulk diamond as a function of the ion energy was thus obtained from a simulation carried out with a target density of 3.52 g cm^{-3} (Figure 62c). In the end, by interpolating data from the latter graph with the relation of Figure 62b, the linear vacancy density realized in the ND layer as a function of the depth was plotted (Figure 62c), hence showing a constant vacancy density profile until ~ 40 µm, being equal to ~ 1×10^3 vacancies ion^{-1} cm^{-1}. Therefore, when considering a ND layer thickness lower than this value, the simulation suggests an almost flat profile along its entire volume, while the Bragg peak (maximum energy release) takes place in the silicon substrate. Finally, by multiplying the delivered fluence with the linear vacancy density, the volume vacancy density can be obtained, resulting for example in the case of F = 5×10^{15} ions cm^{-2} equal to 5×10^{18} vacancies cm^{-3}.

After the proton irradiation, to complete the creation of NV centers by inducing the newly created vacancy to migrate and couple with the nitrogen impurities, a thermal annealing in Ar flux was carried out on all the samples for 2h at 800 °C.

In Figure 63a the PL spectra of MSY-MND before and following the ion implantation in the exemplary case of F = 4.4×10^{16} cm^{-2}, is shown: after the ion irradiation, together with a significant decrease in the PL intensity, the GR1 band appears around 745 nm, which was already found in implanted bulk diamond in sections 3.1.1 and 3.1.2 preceding HTTA. On the contrary, the PL spectrum acquired following the thermal annealing corroborates the coupling of N impurities with the newly generated vacancies by showing a strongly enhanced intensity, the disappearance of the GR1 band and a better outlining of the ZPL of the NV^0 and NV^- centers.

Figure 63b shows the fluorescence intensity from the PL spectra of the samples (integrated from 565 nm to 780 nm) as a function of the delivered fluence, both before (red data) and after (blue data) HTTA. Grey line represents the integrated fluorescence from not-implanted annealed + oxidized MSY-MND. Data were calculated from the average of the integrals of 3-5 spectra acquired for each sample and the error bar is the maximum semidispersion. Due to beam area fluctuations and ion current inhomogeneities during the irradiation, a 20% of error in the fluence values should be also considered.

Before the HTTA process, at low fluences there are no significant variations in PL intensity, while it starts decreasing at higher fluences. This effect can be explained by the quenching effect due to the new vacancies randomly introduced into the lattice by the proton irradiation [167]. After HTTA, the photoluminescence increased at all damage levels, reaching the highest yield at the fluence of

4.4×10^{16} cm^{-2}, which corresponds to a vacancy density of ~ 4×10^{19} cm^{-3}. The latter value is compatible with the damage level at which the maximum fluorescence from NV centers was obtained following He implantation in a previous work for bulk diamond [105]. Once overcome this value, the PL intensity starts decreasing because of the excessive damage.

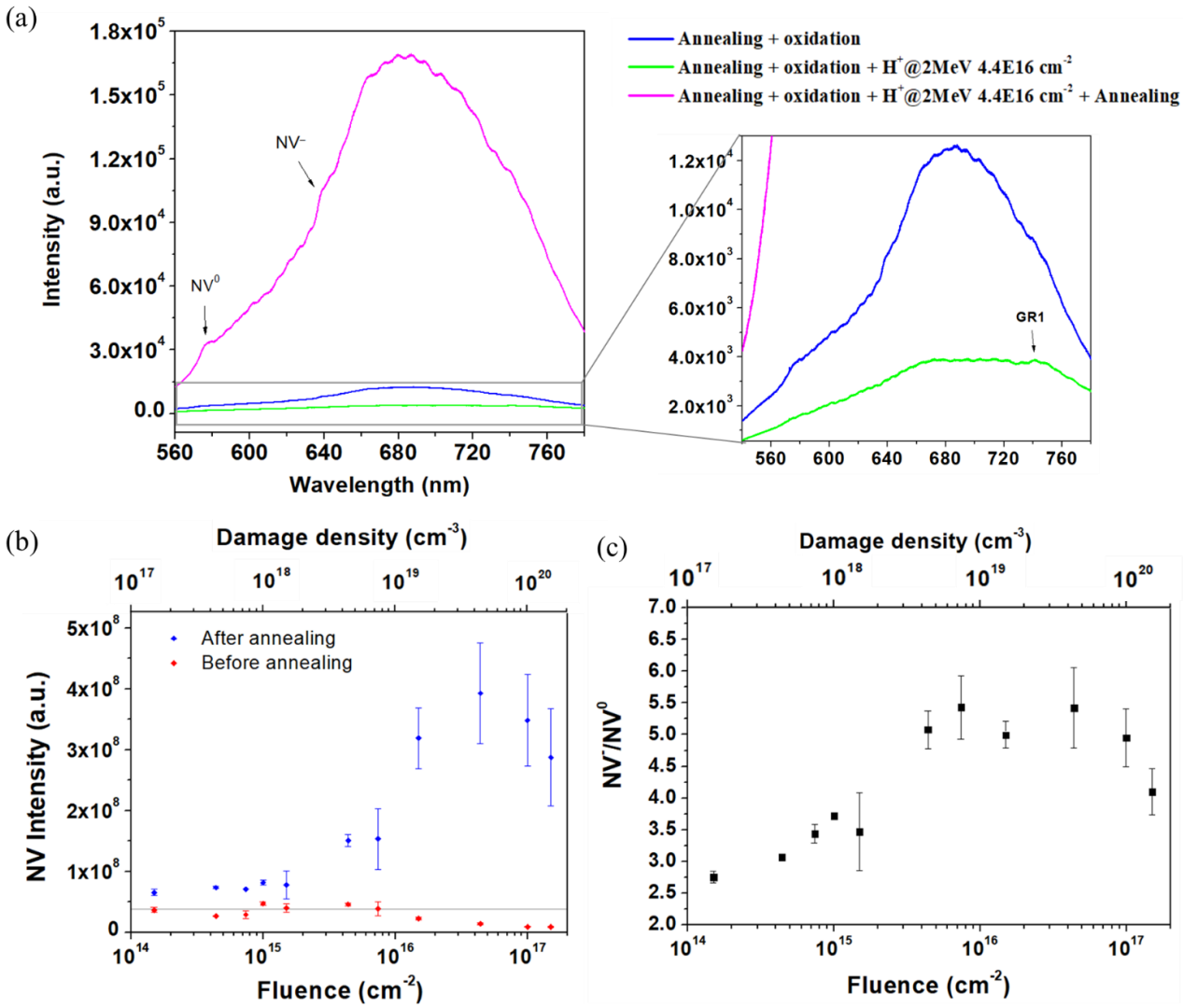

Figure 63: (a) spectra of MSY-MND before and following ion implantation ($F=4.4\times10^{16}$ cm^{-2}) and HTTA; (b) integrated NV PL intensity of MSY-MND as a function of the delivered fluence (or the damage density) before and after HTTA; grey line represents the PL intensity before ion implantation; (c) NV^-/NV^0 ratio as a function of the fluence (or the damage density).

Further analysis was carried out to evaluate the ratio of the PL contribution of the two charge states of the NV centers. In analogy with section 3.2.2, their ratio was estimated by considering $I_{700\ nm}$ / $I_{575\ nm}$. Figure 63c shows its trend as a function of the vacancy density. After a general

increase at lower fluences, at higher damage levels a flattening and finally a decrease (for 1.5×10^{17} cm^{-2}) of the trend is observed. According to a previous work [105], increasing the fluence of implantation, a decrease of the NV^-/NV^0 ratio is expected. In fact, NV centers becomes negatively charged because of the charge transfer from the substitutional nitrogen atoms, which act as donors in the crystal. The higher the implantation fluence the higher will be the number of newly created NV centers; as a result, the number of isolated N atoms capable of transferring electrons to the NV centers is reduced, resulting in the increase of the relative number of NV^0 centers. However, results in [105] were referred only to bulk diamond and the decrease of the ratio was observed only at higher damage levels respect to the case under exam, starting around a damage density of 10^{20} cm^{-3}, which correspond approximately to the maximum fluences reached in the work of the candidate. Nonetheless, while the initial decrease of the ratio in correspondence of the latter point is well explainable as mentioned above, the increase at lower densities is still unclear, but was already observed in ND in another work [168], ascribing the effect to the influence of the oxidized surface. However, the measurements of Figure 63 are conducted following HTTA, thus being essentially depleted of oxygen-containing species and suggesting the need of further future investigation to solve this issue.

In order to better elucidate the mechanism underlying the phenomenon of NV center formation, a simplified theoretical analysis has been carried out. Considering the atomic density of diamond ($\rho_d = 1.77\times10^{23}$ cm^{-3}) and assuming a concentration of nitrogen impurities of the order of 100 ppm (typical of HPHT diamond, see section 1.4.2), the corresponding volume density of nitrogen impurities will be $\rho_0 \sim 1.77\times10^{19}$ cm^{-3}. It is worth noting at this point that the created vacancy density estimated by the simulation in the case of the maximum obtained PL ($F \sim 4\times10^{16}$ $cm^{-2} \rightarrow$ $\rho_{vac} \sim 4\times10^{19}$ cm^{-3}) is comparable with the density of nitrogen atoms, suggesting the explanation for the maximum PL intensity observed at this fluence. With these assumptions, the maximum number of NV centers that can be created is limited around $\sim 10^{19}$ cm^{-3}. Nonetheless, the process of NV center formation is also limited by an efficiency not yet available in literature for the case under exam.

During the formation of NV centers, many variables are to be considered. To describe the phenomenon, a differential equation can be formulated (eq. 10). An infinitesimal variation in the density of created NV centers $d\rho_{NV}$ will be proportional to the infinitesimal variation of vacancy density $d\rho_{vac}$, which in turns can be written as the product of the linear vacancy density ($\lambda = 1\times10^3$ vacancies ion^{-1} cm^{-1}, as estimated from Figure 62d) with the infinitesimal variation in the delivered fluence ($\lambda\, dF$). In addition, $d\rho_{NV}$ is proportional to the instant density of uncoupled

nitrogen impurities ρ_N, since the higher is the density of free nitrogen impurities, the higher will be the probability for a vacancy to couple with them. $d\rho_{NV}$ is also proportional to the volume of migration of the vacancies, as the larger is the volume in which a vacancy can migrate, the higher is the probability of coupling with a nitrogen atom (the whole average volume of a single ND, V = $8.7 \cdot 10^{-17}$ cm^3, was assumed). Finally, a scale parameter η is introduced in the equation.

$$d\rho_{NV} = \eta\, \rho_N\, V\, d\rho_{vac} = \eta\, \rho_N\, V\, \lambda\, dF \tag{10}$$

In turn, the instant density of uncoupled nitrogen atoms ρ_N can be written as the difference between the total density of nitrogen impurities ρ_0 and the density of coupled NV centers ρ_{NV}:

$$d\rho_{NV} = \eta(\rho_0 - \rho_{NV})V\lambda dF \tag{11}$$

Defined $\alpha = \frac{\rho_{NV}}{\rho_0}$ as the fraction of vacancy-coupled N atoms, by integrating the differential equation, the following relation (eq. 12) is obtained:

$$\int_{0.1}^{\alpha} \frac{d\alpha}{1-\alpha} = \int_0^F V\lambda\eta dF \quad \rightarrow \quad \alpha = \frac{\rho_{NV}}{\rho_0} = 1 - 0.9 \cdot e^{-V\lambda\eta F} \tag{12}$$

The integral was calculated assuming an initial value of $\alpha_i \sim 0.1$. This value was extrapolated from Figure 63b, by dividing the PL intensity of ND before the proton implantation (grey line) with the maximum PL obtained at the fluence of 4.4×10^{16} cm^{-2}. A linear relationship between the collected PL signal and the number of NV centers was thus assumed for simplicity.

Figure 64a reports experimental data from Figure 63b after normalization with respect to the maximum PL obtained at 4.4×10^{16} cm^{-2} (black squares). The green curve, obtained from the best fit of eq. 12 with these data, showed a good agreement with the experimental trend, supporting the validity of the model and providing a value of η ~ 0.001 vac^{-1}. The role of this parameter is to define the order of magnitude of vacancies required to create a relevant amount of NV centers.

In light of all these considerations, the maximum value of fluorescence reached at F~ 4.4×10^{16} cm^{-2} might correspond to the fact that most of the N impurities were coupled with vacancies, while further damage results in the formation of isolated vacancies acting as quenching defects (effect not considered in the model), thus determining a decrease in the PL intensity. As a result, at that fluence, a concentration of ~10^{19} NV cm^{-3}, corresponding to ~ 500-1000 NV centers per single ND, can be hypothesized. Nonetheless, although the model is well in line with experimental data, these

results are to be considered in light of a significant chain of simplifications which prevents from precise evaluations.

Further reinforcement of the results can be obtained by comparing them with those of Pezzagna et al. [169]. In this work, the yield of creation of NV centers for single implanted N atom as a function of the ion energy was estimated in the case of N implantation. The yield (i.e.: the probability, given a certain number of vacancies, for an N atom to get coupled with a vacancy) showed an increasing trend with the ion energy, due to the higher amount of vacancies created around the implanted nitrogen in the case of more energetic ions. Data presented in that work were elaborated and combined obtaining the graph of the yield as a function of the vacancies created (see Figure 64b). As expected, the graph showed an almost linear trend, with a slope change at the lower yield values. In first approximation, this slope corresponds to the above-defined scale parameter η and correlates the number of vacancies available with the probability of NV center formation. Both the ND of this thesis and samples investigated in [169] were annealed following ion implantation for 2h at 800 °C. By applying a model from a previous work [170], it can be calculated that, following thermal annealing in these conditions, vacancies can migrate up to d ~ 160 nm (eq. 13):

$$d \sim \sqrt{D_0\, t\, e^{-\frac{E_a}{kT}}} \tag{13}$$

where $D_0 = 3.6 \times 10^{-6}\ \mathrm{cm^2 s^{-1}}$, $E_a = 1.7$ eV is the activation energy for vacancy diffusion, k is the Boltzmann constant, T is the annealing temperature and t the annealing time.

In the experiment of [169], the maximum employed energy of N implanted ions was 20 MeV, and the corresponding Bragg peak in which most of the vacancies are created (simulated with SRIM) presents an half-width of ~200 nm, thus allowing in first approximation to consider all the vacancies created as available to potentially form an NV center with the implanted N atom. When considering the work carried out in this thesis, the number of vacancies to be considered available for the formation of NV centers is defined by the product of the vacancy density and the average volume of the single ND, $V = 8.7 \cdot 10^{-17}\ \mathrm{cm^3}$ (a median diameter of 55 nm and spherical geometry was considered). In the explored values of fluence, this number of vacancies ranges between 10 and 10^3, thus almost overlapping with the range of Figure 64b derived from the work of Pezzagna et al. This consideration allows to apply the slope from the latter graph also in the situation of the present work. Therefore, assuming for simplicity a linear trend, the slope of the graph was evaluated with a linear fit, resulting in $\eta = 0.0066\ \mathrm{vac^{-1}}$. By setting the latter value in

eq. 12, the blue curve of Figure 64a is obtained. Interestingly, the resulting trend was quite similar to that of the experimental normalized PL intensity as a function of the fluence excepted for a slight stretch in the horizontal scale. This little incongruency could be ascribed to the fact that the estimated value of η was considered constant across all the vacancy density range.

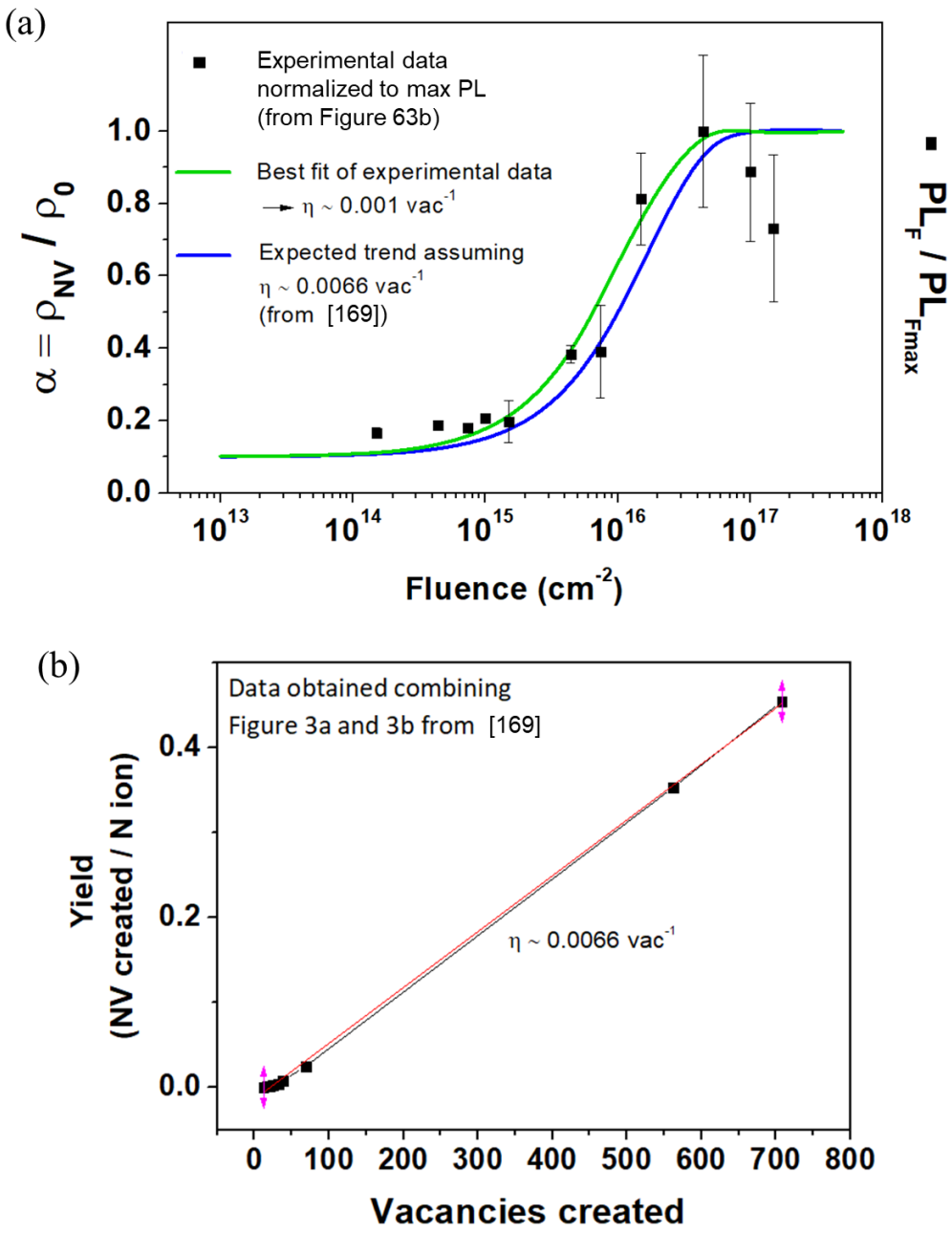

Figure 64: (a) fraction of total N atom involved in the formation of NV centers as a function of the fluence. Green plot refers to the fit of experimental data with eq. 12, while blue plot corresponds to eq. 12 by using η as extrapolated from 64b. Black squares correspond to the measured PL from Figure 63b normalized to the maximum PL at 4.4× 10^{16} cm^{-2}. (b) Yield of creation of NV centers per single N atom as a function of the number of vacancies created by the implanted N, derived from [169].

In a successive ion implantation run carried out following the characterizations presented in section 3.2.2 concerning "aggressive oxidations", both annealed and annealed + oxidized 36 h at 500 °C were chosen for proton irradiation. This oxidation level was selected as ND reached very high fluorescence values, while avoiding excessive degradation that might have occurred at 525 °C. Both types of samples were implanted with fluences of 4.4×10^{16} cm^{-2} (corresponding to the fluence that maximized the PL intensity in the previous run) and 1×10^{16} cm^{-2}. Sample preparation and operations were carried out in total analogy with respect to the previous run.

Following the irradiation, the samples were processed and characterized with Raman/PL spectroscopy. Firstly, the ideal time of re-annealing after ion implantation was investigated. To this scope, annealed + oxidized samples were annealed in 3 successive times in Ar flux for 2 h at 800 °C. Figure 65 summarizes the results in terms of integrated PL intensity. Error bars are obtained from the variability of the acquired spectra in different point of the substrate. As can be evinced, after the second re-annealing, the fluorescence stopped to increase, allowing to conclude that 4 h are sufficient to obtain the maximum NV centers formation, while further prolonging the process could even be counterproductive (mild graphitization can occur).

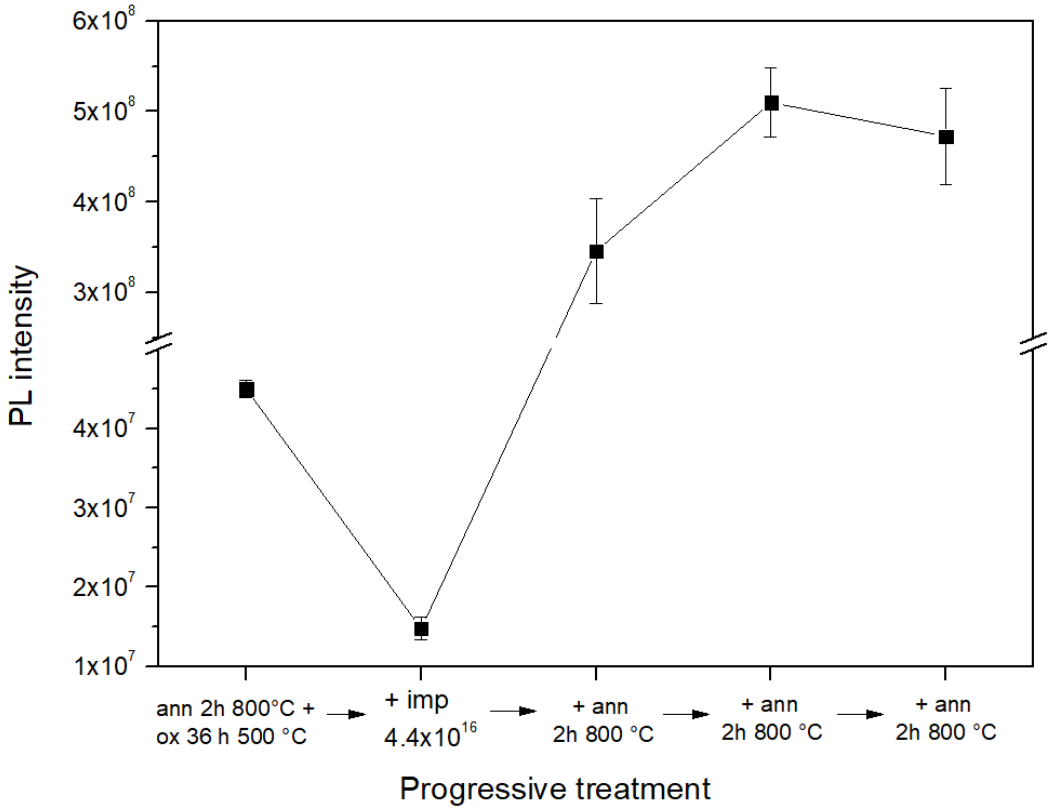

Figure 65: PL intensity of implanted MSY-MND following re-annealing 3 successive times for 2h at 800 °C

Secondly, annealed + implanted and annealed + oxidized + implanted MSY-MND were thus subjected to 4 h HTTA, both showing 1.5 orders of magnitude increase in fluorescence (Figure 66). At this processing step, the two samples only differ for their surface oxidation status, showing 1 order of magnitude of separation. Both samples were then treated with repeated air oxidations for 12 h at 500 °C, finally showing comparable PL intensities. Further oxidation cycles determined only mild enhancements for previously not-oxidized samples (blue line), while a slight detrimental effect occurred in the previously oxidized samples (pink line), as the process probably gets too aggressive. The ratio of the intensity of NV^-/NV^0 for these series are reported in Appendix C, showing results consistent with the trends observed following irradiations and oxidations showed in the previous paragraphs.

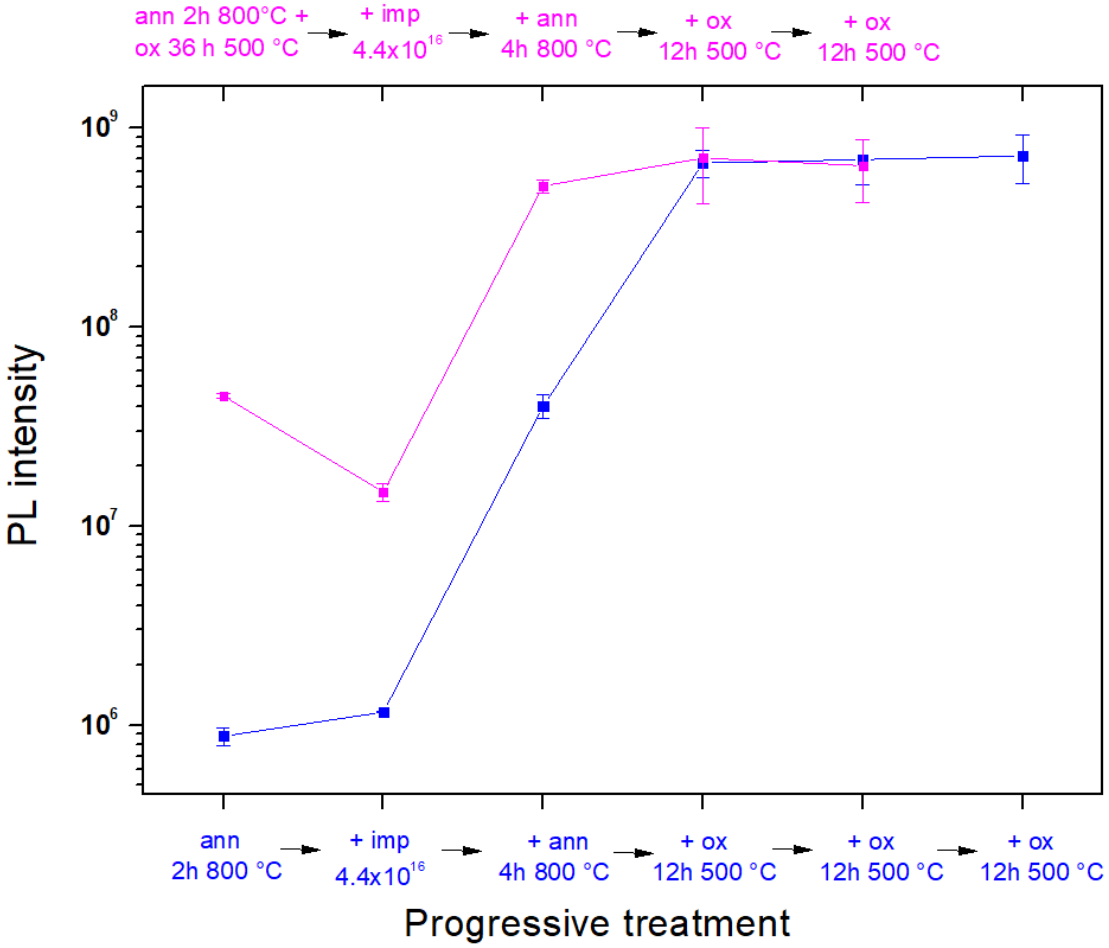

Figure 66: PL intensity at progressive treatments of implantation, HTTA and oxidation for both previously oxidized and not-oxidized MSY-MND.

The mentioned post-processing treatments are carried out without removing the ND from the silicon substrates and thus excessive oxidation negatively affect the amount of deposited powder,

suggesting as more convenient the option of conducting the oxidation before the deposition and the ion implantation.

Finally, in Figure 67 the PL comparison between the processing "path" of oxidized MSY-MND implanted at 1×10^{16} cm^{-2} and 4.4×10^{16} cm^{-2} is shown. In the case of the latter fluence, following ion implantation, a lower fluorescence is obtained, due to the higher damage level. Following HTTA, the trend is inverted, as the major vacancy creation allows the formation of a higher number of NV centers. The result is in accord with data already observed in the first run of ion implantation, where 4.4×10^{16} cm^{-2} determined a superior fluorescence with respect to 1×10^{16} cm^{-2}.

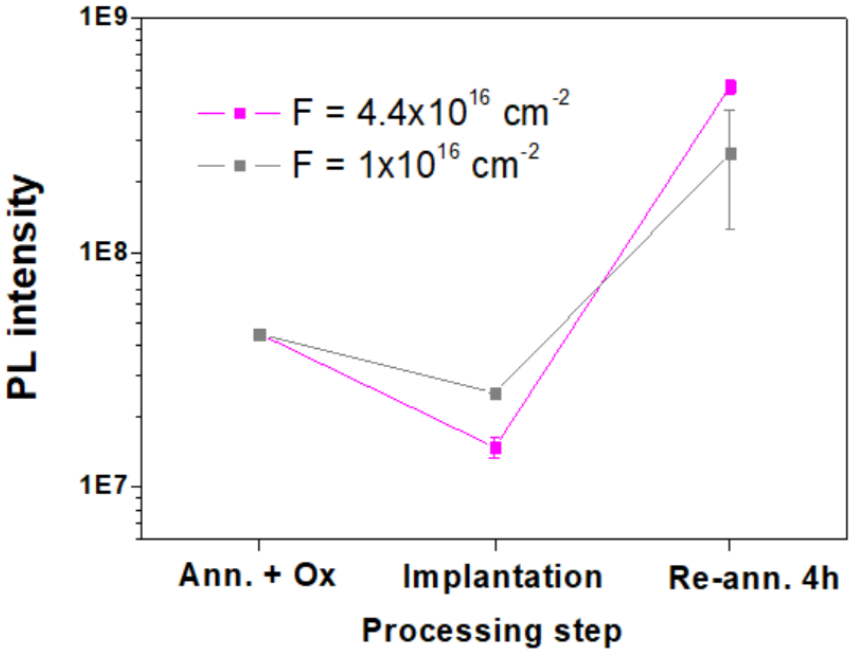

Figure 67: comparison of NV centers PL intensity of oxidized MSY-MND following ion implantation in the cases of $F=1\times10^{16}$ cm^{-2} and $F=4.4\times10^{16}$ cm^{-2}

In summary, up to date, the best processing scheme obtained by the candidate in order to optimize the PL intensity of the investigated ND, suggests:

1) a first thermal treatment (HTTA) to graphitize amorphous carbon components of ND (Ar or N_2 flux, 2 h at 800 °C);
2) an air oxidation to remove the surface quenching phases at temperatures between 475 °C and 500 °C for times ranging from 24 h to 36 h;
3) proton irradiation delivering a fluence of 1×10^{16} cm^{-2} - 5×10^{16} cm^{-2}
4) post-implantation HTTA (Ar or N_2 flux, 4 h at 800 °C);

5) a further mild oxidation to recover from the minor graphitization effects induced by the ion implantation and the subsequent HTTA (see the slight increase in PL in Figure 66 following the further oxidation), as well as promoting an increase in NV^-/NV^0, as NV^- centers are of major interest in quantum and sensing applications.

With this protocol, the integrated fluorescence resulted increased of ~ 3 orders of magnitude with respect to unprocessed MSY-MND.

3.2.5 Biochemical functionalization

As discussed in the introduction, thanks to their biocompatibility combined with fluorescence and magnetic optically active properties, ND are interesting for a wide variety of biomedical purposes. However, specific, uniform and predictable surface functionalization with biomolecules still remains the main task to make these nanosystems suitable for such applications.

Two main functionalization strategies for linking biomolecules on the surface of ND were employed in previous works:

- the exploitation of surface oxygen-containing species (particularly carboxylic groups), by using reactions such as esterification, amidation and etherification with small or large organic molecules / polymers [112,171,172] .
- the involvement of the carbon double bonds in sp^2 graphitic surface layers, which allow the direct linking of organic moieties with coupling [173,174] and cycloaddition reactions (such as Diels-Alder) [82,175,176] .

On this basis, the colleagues of the Department of Drug Science and Technology (DDST) of the University of Torino were supplied with MSY-MND in the following forms:

(1) annealed in N_2 flux for 2h at 800 °C
(2) annealed as in (1) + oxidized 30 minutes at 400 °C
(3) annealed as in (1) + oxidized 1 h at 500 °C

The oxidation conditions correspond to the two extremes of the processes carried out by the candidate and presented in paragraph 3.2.2 for milder oxidations. Starting from these samples (different in graphitic and carboxylic groups surface amount), both Diels-Alder cycloaddition and condensation reactions were performed. As the topic would go beyond the competence and the activity of the candidate, the details of the processes are not reported in this thesis. Nonetheless, a

brief comment concerning the most interesting results represent an important feedback to the work reported in the previous paragraphs. Figure 68 schematizes the two kinds of reaction.

In addition to the thermally oxidized ND, another sample of annealed MSY-MND was functionalized following an aggressive chemical etching with sulfonitric acids mixture, for comparison.

Following the chemical functionalization process, thermogravimetric analysis [114] was conducted to assess the obtained amount of linked molecules. Figure 69 shows, in the case of condensation reactions with COOH groups, a progressive increase in surface conjugation adduct (in terms of mmol of adduct over 100 mg of ND) as the oxidation treatment gets more aggressive. An opposite trend is observed in the case of functionalization reactions involving graphitic components as substrate, due to the gradual etching of these phases by means of the oxidation treatments. ND pre-treatment with sulfonitric mixture proved to be the more efficient in removing graphitic phases and covering the surface of ND with a higher amount of carboxylic groups.

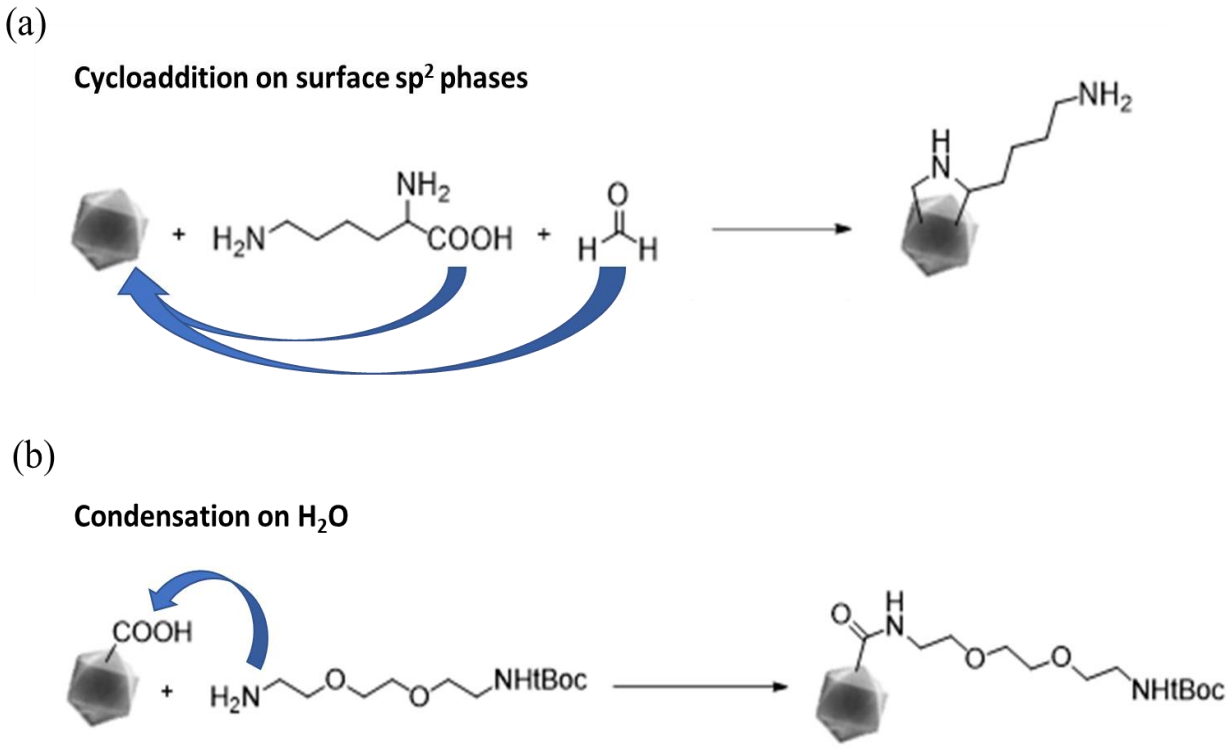

Figure 68: functionalization reactions with demonstrative linking biomolecules by exploiting 1,3-dipolar cycloaddition involving surface graphitic layers (a) and condensation involving carboxylic groups (b).

Nonetheless, it is worth remarking that thermal oxidations performed on the samples were only in the "milder" version (the maximum level was the case of air treatment for 1h at 500 °C). More aggressive thermal oxidations shown in section 3.2.2 showed better removal of graphitic components and higher amounts of oxygenated species on the surface of ND, probably providing more degrees of derivatization in both cycloaddition and condensation reactions. Moreover, differently from the thermal treatment, oxidation with sulfonitric acids is very difficult to reproduce and control in a fine way. With these strategies it is possible to obtain NDs having multiple decorations with heteroatoms in a simple, efficient, reproducible, tunable and versatile manner, tailoring them for many purposes, for instance biomedical applications.

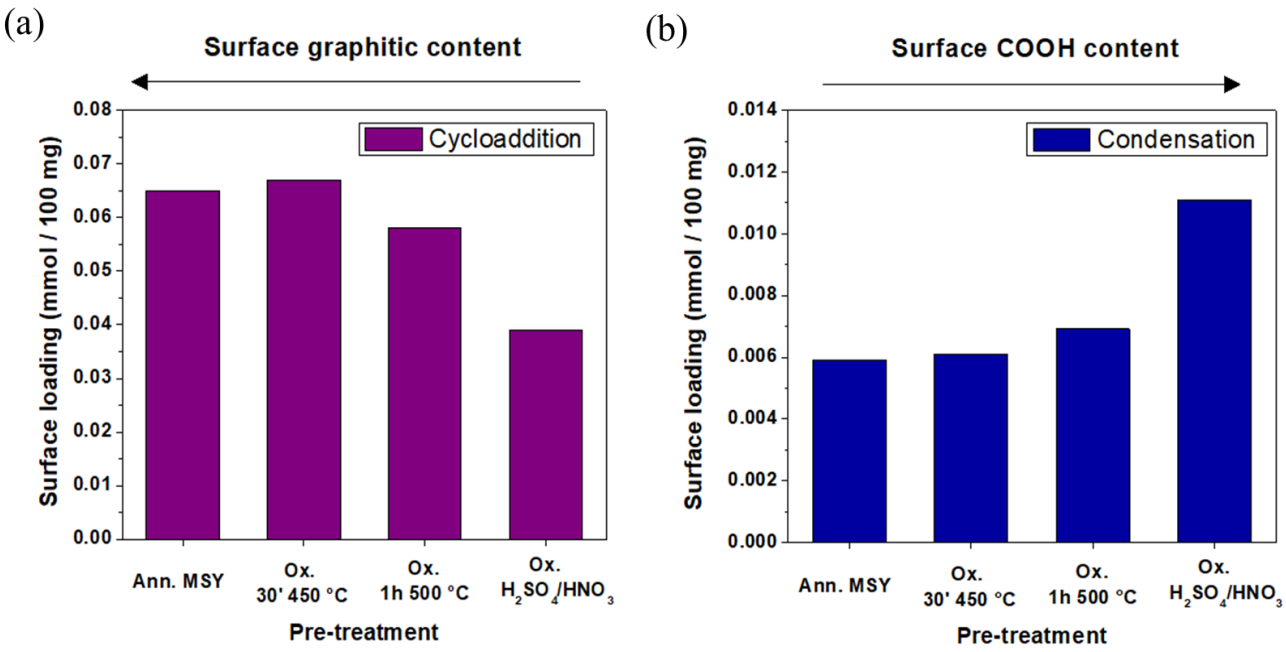

Figure 69: surface loading following functionalization in the case of cycloaddition reaction over graphitic surface phases (a) and carboxylic groups (b) as a function of the previous oxidation treatment. Table listing the processes and the respective values of surface loading (c).

3.2.6 Functionalization with Cetuximab and in-vitro test

In this paragraph, a first attempt of in-vitro test with functionalized ND, performed by the researchers of the DSTF, is reported. In this case annealed + oxidized (8 h at 450 °C) s-E6-MND were functionalized with cetuximab, which is a specific monoclonal antibody that interacts selectively with Epidermal Growth Factor Receptor (EGFR). The EGFR, in fact, is overexpressed on the membrane of different types of cancer cells (e.g. colon, head and neck cancer) and the signal transduction pathways associated are involved in the control of cell survival, cell cycle progression,

angiogenesis, migration and invasion, mechanisms typically altered in tumor tissues. Cetuximab selectively binds to EGFR with an extremely high affinity and inhibits the function of the receptor itself (Figure 70). In many cases, the presence of an activating mutation in KRAS, a protein involved in the EGFR signaling pathway, is responsible of the onset of resistance to cetuximab. The latter, after interacting with the EGFR, induces its internalization by endocytosis, thus behaving as a vehicular agent in the drug delivery function, and a possible approach to overcome the resistance linked to onset of mutations in the EGFR pathway, e.g. KRAS, BRAF, PI3K.

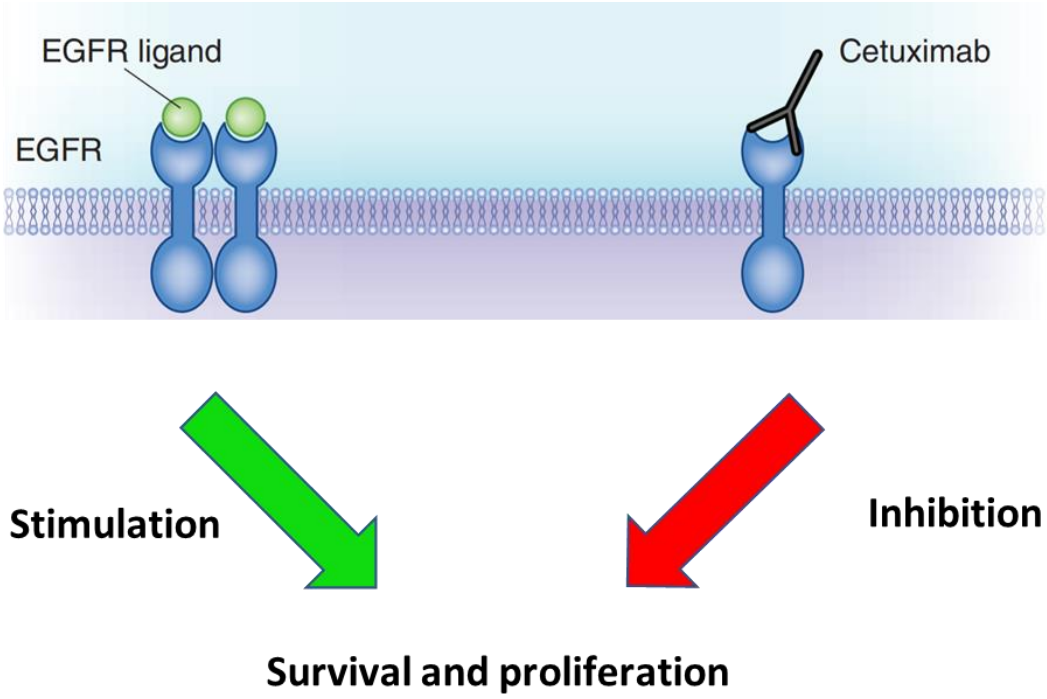

Figure 70: simplified scheme of the action of cetuximab. The block of the EGFR cetuximab-mediated, is responsible of inhibition of the intracellular pathway and of the induction of apoptosis [177].

In brief, cetuximab was grafted to ND surface (NDs-Ctx) exploiting a chain molecule acting as a "bridge", covalently linked to the surface by means of a condensation reaction with carboxylic groups. After proper dilution in the cellular medium, a colon-rectal cancer cell line (DiFi) was incubated with ND at a concentration of 100 μg ml^{-1} and left in incubation for 24 h. After this time, cells were washed, labelled with CellTracker™ Green CMFDA, (green emission) and fixed in paraformaldehyde (4%). At this point, the interaction with the cell membrane and/or the internalization degree (compared to a control sample of not-functionalized ND) were evaluated with an inverted confocal Leica SP8 microscope. Images of ND fluorescence were acquired in the range of the maximum emission of NV centers (640 nm – 720 nm), while cells were imaged by exploiting the green labelling under 488 nm laser excitation.

Figure 71 reports the acquired confocal microscopy images, coupled with the respective optical images. The fluorescence images are the result of the overlap of two images acquired at 488 nm (green cells fluorescence) and at 561 nm (red ND fluorescence). From the result, a higher interaction level of ND with the cells is observed in the plate of NDs-Ctx treated DiFi cells, while weak or no ND fluorescence signal was assessable inside the cells in the case of unmodified ND administration, suggesting a successful linking, and partial internalization, of ND-Ctx with the DiFi cancer cells.

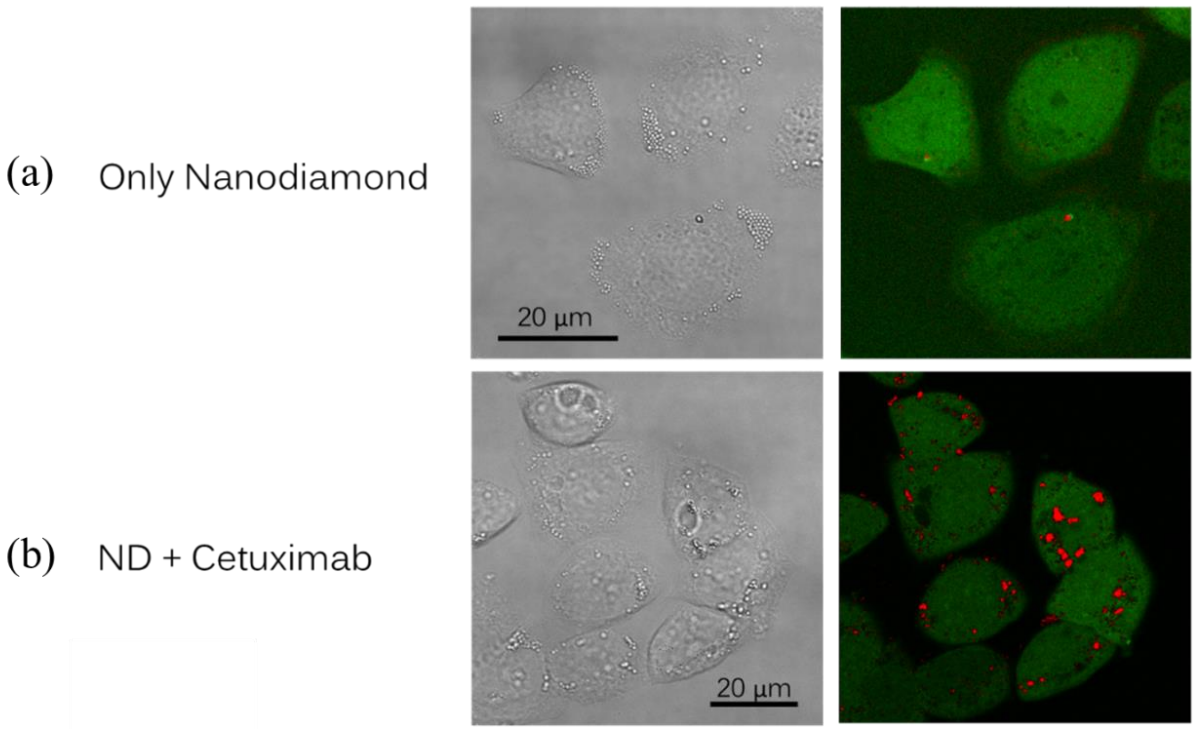

Figure 71: optical and confocal images of ND administered to DiFi cells in the case of not-functionalized (a) and cetuximab-conjugated s-E6-MND (b)

4 Conclusions and future developments

This section is meant to summarize the result obtained in the thesis. The general purpose of the work was to characterize and modify both bulk diamond and nanodiamond with thermal processes and ion beam-based techniques, with a focus on its further application in biomedical context.

Firstly, an optical-grade type IIa monocrystalline diamond sample was characterized by AFM and Raman spectroscopy following implantation with a focused 8 MeV ^{11}B ion beam at multiple fluences ranging between 1×10^{15} cm^{-2} and 4.4×10^{16} cm^{-2}.

AFM results showed the presence of the well-known swelling effect, together with an edge "lip" still scarcely investigated in previous works. The measured lip geometry was compared with previous theoretical prediction developed with analytical methods, resulting only partially compatible with the expectations. The differences are probably ascribable to the fact that the applied model was based on the characteristics of a post-annealing sample with uniform regions in terms of mechanical properties. Indeed, following HTTA, due to the sharp conversion of the phases below and above the graphitization threshold, the embedded structure possesses more defined edges with respect to the situation before the treatment.

Concerning Raman characterization, first order diamond peak was analyzed in terms of intensity, width and position at the different delivered fluences, showing results consistent with previous works and confirming an agreement with what expected by the formalism of Kramers-Kronig relationships.

The characterization after HTTA allowed the identification of the graphitization threshold in correspondence of a fluence of 5×10^{15} cm^{-2}, which corresponds to a vacancy density of ~4.4×10^{22} vacancies cm^{-3}, in agreement with the range estimated by previous studies. Moreover, an estimation of the thickness of the graphitic layers was performed by combining this result with SRIM simulations, providing results consistent with the evaluated trend of the intensity of the Raman G band at the different fluences. Finally, the characterization conducted on the areas irradiated at a fixed fluence and variable ion beam current suggested the use of higher currents when willing to limit damage during this doping procedure.

Aside from providing to the scientific community these integrative and systematic data with the publication in [130], the above-mentioned studies allowed the candidate to become familiar with

the impact of ion-beam techniques on the modification of diamond, as well as the use of Raman spectroscopy in its characterization.

In section 3.2.2, the realization of biosensing multi-electrode arrays for the detection of action potentials and exocytotic events from excitable cells was presented. Ion beam lithography with He ions was employed for the realization of the graphitic microchannels into the diamond matrix. The choice of this material was considered due to the promising combination of both the properties of diamond (biocompatibility, chemical inertness) employed as a growth substrate and of graphite (electrical conduction) at the basis of the sensing microelectrodes interfacing with cells.

One electrode of the realized device was characterized by means of Raman spectroscopy, providing maps of the integrated first order diamond peak and graphite-related G-band signals which evidenced its emersion to the surface and allowed the identification of its structural properties. Also the Raman map of the diamond peak shift was reconstructed, providing information about the mechanical stress induced by the presence of the embedded electrode in the diamond matrix.

In addition, electrical measurements allowed the estimation of the electrodes resistance and eventually, by applying the geometrical parameters, the resistivity, which resulted compatible with that of nanocrystalline graphite.

Some examples of in-vitro measurements from cultured neurons and sinoatrial node from cardiac tissue was also reported, demonstrating the proper functioning of the device for both potentiometric action potential analysis and amperometric exocytosis detection. Results were comparable with those obtained with conventional commercial instrumentation, with the main advantage, provided by the μG-D-MEA, of performing both measurements with the same device. Presented data concerning this topic where published in [101].

The larger part of the work was then focused on the processing and characterization of nanodiamonds. Systematic analyses were carried out on differently sized as-received ND (both DND and MND), as well as before and after annealing in a nitrogen environment and subsequent thermal oxidation in air. As a result, the following general conclusions were established:

- higher fluorescence and lower graphitic content are observed in Raman spectra of oxidized samples, especially MND, due to the partial removal of surface contaminations; oxidized MND samples are thus more suitable when planning to applicate them for in-vitro bio-labelling experiments;

- hydrophilicity, and thus dispersibility, of the samples, as evidenced from DRIFT spectra and DLS data, followed the general order oxidized > untreated >annealed, thus relating with the amount of surface oxygen-containing groups; MNDs resulted easily dispersible in water solutions, while DNDs presented a strong aggregation level and weak surface potential, thus being less suitable for drug delivery and biomedical applications, where proper stability and disaggregation in solution are essential;
- electrical measurements, in correlation with the other techniques, showed increased conductivity in ND presenting a higher hydrophilicity profile, due to the occurrence of the Grotthuss mechanism. Untreated DND can be considered when a low electrical resistance is required, taking advantage of both the external graphitic phases and the relevant surface water adsorption due to their hydrophilicity, while annealed MNDs should be preferred when willing to avoid both these effects and to guarantee an insulating interface.

Two campaigns of systematic oxidations and characterization were then conducted on MSY-MND in order to study the evolution in terms of surface chemistry (DRIFT spectroscopy) and photoluminescence deriving from NV centers (PL spectroscopy). In general, higher oxidation levels resulted correlated with a higher number of oxygen-containing chemical groups and enhanced NV fluorescence. Regarding the first, mild oxidations determined the appearance of mainly carboxylic and hydroxyl groups, intermediate levels a further increase of these species together with the appearance of anhydrides/lactones and finally at highly aggressive conditions a strong increase of mainly C-O groups and of surface hydrophilicity. Regarding PL analysis, a tendency to a saturation was observed at the highest oxidation degrees, probably due to the almost complete removal of surface quenching phases. Moreover, excessive oxidation resulted in a slight decrease in fluorescence, as also the diamond core phases could have been affected. NV^-/NV^0 ratio showed the highest value in the mildly oxidized samples, thus suggesting them as preferable when a high concentration of NV^-, for applications such as thermo-magnetometry, is required.

Hydrogenation of s-E6-MND was successfully conducted with a thermal process at temperatures above 800 °C in H_2 flux, as confirmed by DRIFT spectra. Also electrical measurements showed a significant increase in conductivity after hydrogenation with respect to the other treatments.

Ion implantation techniques, in the specific case with 2 MeV proton beams, resulted effective in drastically increasing the PL emission of NV centers from MSY-MND. In the explored values, a fluence of 4.4×10^{16} cm^{-2}, corresponding to a damage level of 4×10^{19} vacancies cm^{-3}, provided the highest fluorescence yield, by determining about 1 order of magnitude with respect to

unirradiated samples (after HTTA). Starting from untreated samples, the combination of thermal processes with ion implantation allowed to reach, in the best cases, about 3 orders of magnitude increase in PL.

Overall, the results provided useful insight into the connection between ND surface chemistry, hydrophilicity, dispersibility and fluorescence, which are essential starting points for future ND applications. Part of these presented data were published in [178]. Preliminary results were also provided concerning the surface functionalization with demonstrative molecules, by evidencing the possibility of finely tuning their amount by selectively controlling the degree of graphite and / or carboxylic groups on the surface.

Future activities will be planned as follows:

- the acquisition of more detailed information about the ND surface chemistry, clarifying the still unclear issues described in the previous pages, such as the real mechanisms occurring at the different oxidation degrees and their effect on NV centers;
- in terms of dispersibility, it will be important in perspective of biomedical applications the performing of DLS measurements in culture medium;
- the successful hydrogenation of s-E6-MND will allow to proceed with ROS generation experiments under ionizing radiation and the performing of in-vitro assays. Regarding this, a collaboration with ENEA institute (Casaccia, RM) has been established. Due to their more suitable dimensions, the transfer of the same treatment on MSY-MND will be carried out;
- ion implantation of ND with 2 MeV proton beams is limited by the small amount of material irradiated in a single shift. To solve this issue and obtain higher quantities (required for biochemical functionalization and biological experiments), the access to higher ion energy facilities (possessing higher penetration depth and thus a higher achievable volume) will be considered;
- further functionalization processes will be carried out by supplying the colleagues of the DSTF with ND oxidized at more aggressive levels, thus widening the range of tunability of the surface derivatization degree;
- further in-vitro experiments with/without functionalization will be performed with ion implanted and oxidized MSY-MND, to observe in real biolabeling experiments the effectiveness of the efforts made to increase PL.

Appendix A

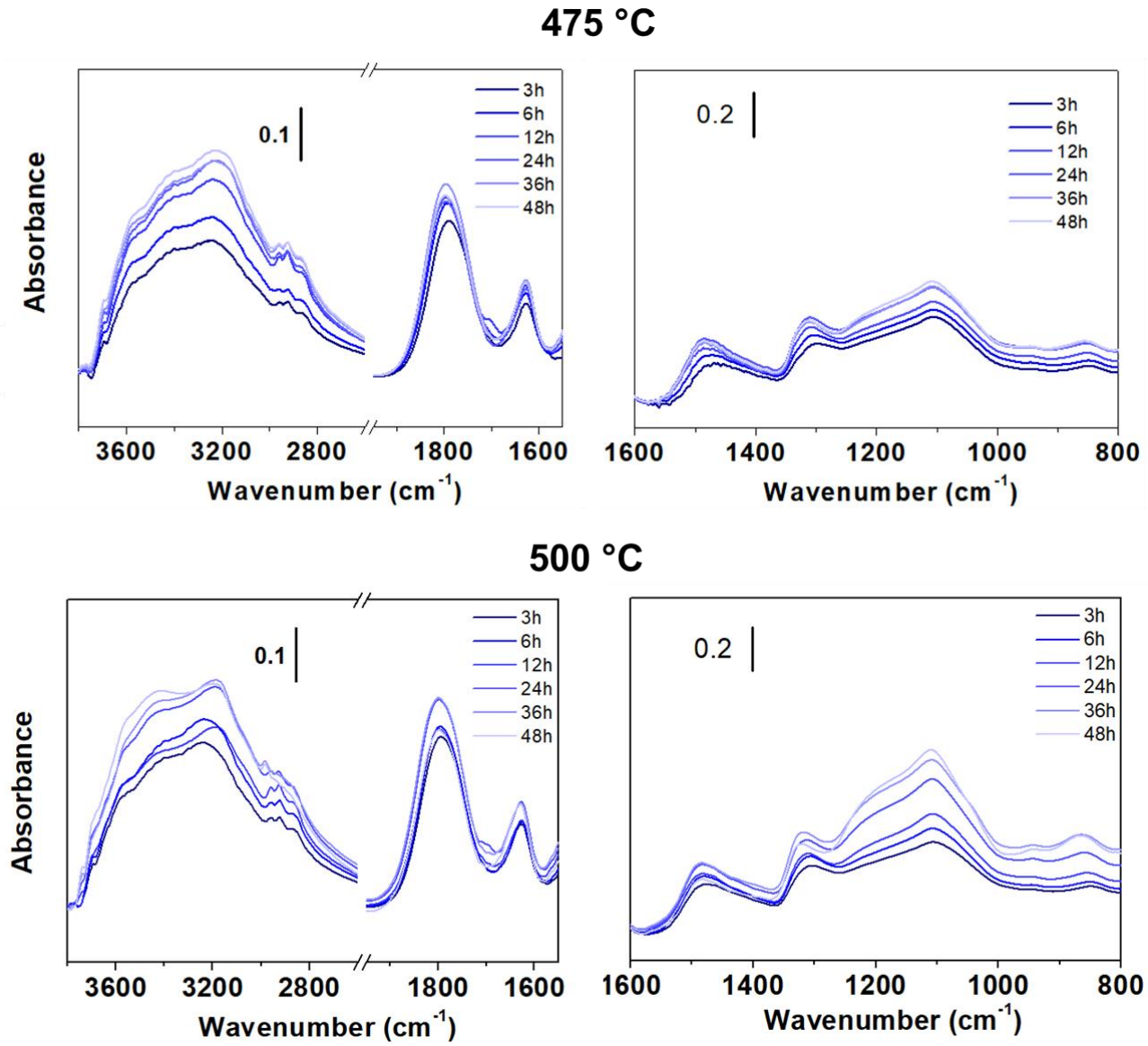

Figure A: DRIFT spectra of MSY-MND oxidized at 475 °C (a) and 500 °C (b) at variable process times

Appendix B

This appendix reports TEM images of MSY-MND oxidized at 450 °C for 3h (Figure Aa) and at 525 °C for 48 h (Figure A2b). Unfortunately, excepted for rare cases, the diffuse overlap of the ND did not allow a proper recognition of the single ND outlines, preventing the acquisition of a sufficient statistics for a size distribution assessment. Nonetheless, it is possible to observe how in general ND oxidized at the strongest oxidation level (b) resulted smaller and with a more "rounded" outline with respect to the sharp edges of case (a). This observation reinforces the effects of photoluminescence deterioration and NV^-/NV^0 ratio increase at the strongest oxidation levels. In addition, together with the increase in C-O/C-O-C surface species, the lower size might have been crucial also in the increase in water adsorption and hydrophilicity observed in DRIFT spectra.

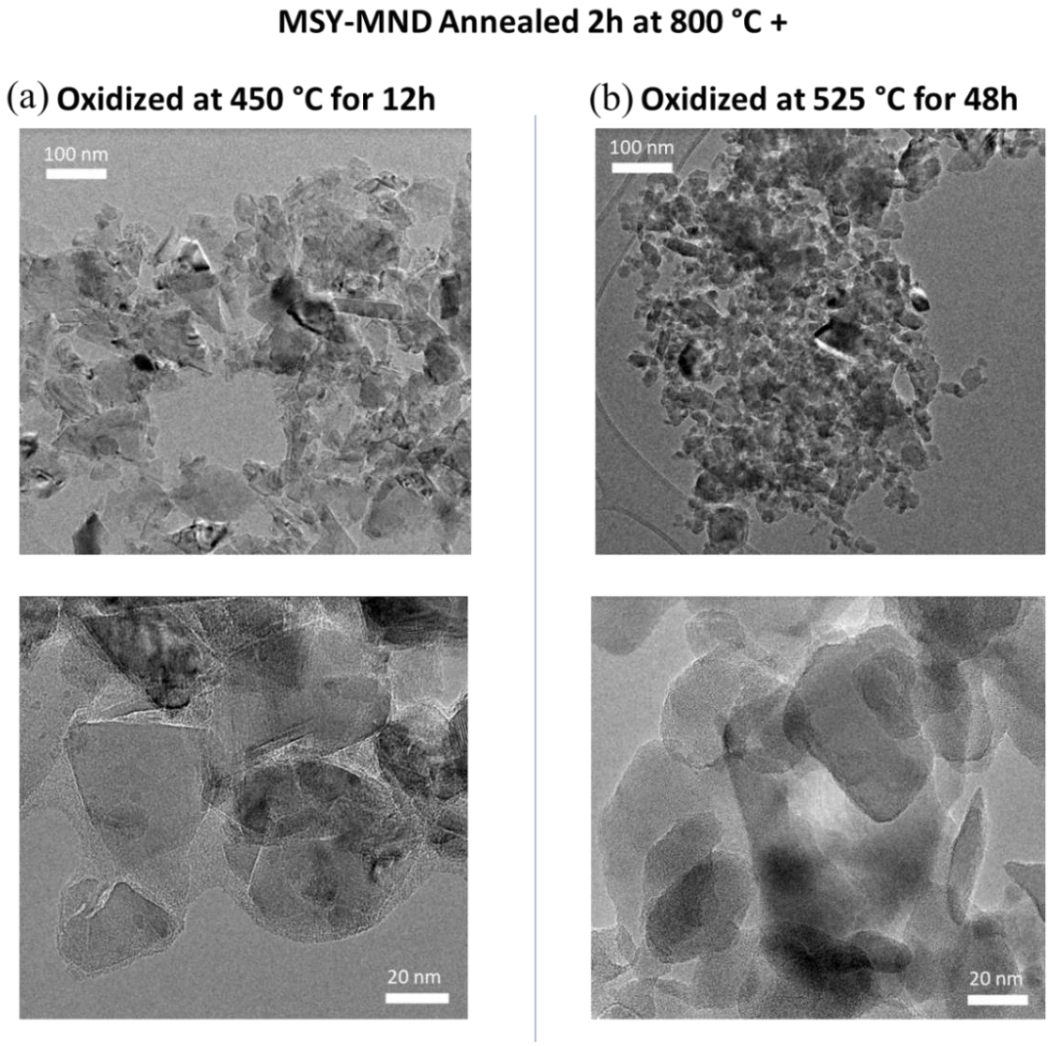

Figure B: TEM images of annealed MSY-MND following oxidation at 450 °C for 12 h (a) and at 525 °C for 48 h.

Appendix C

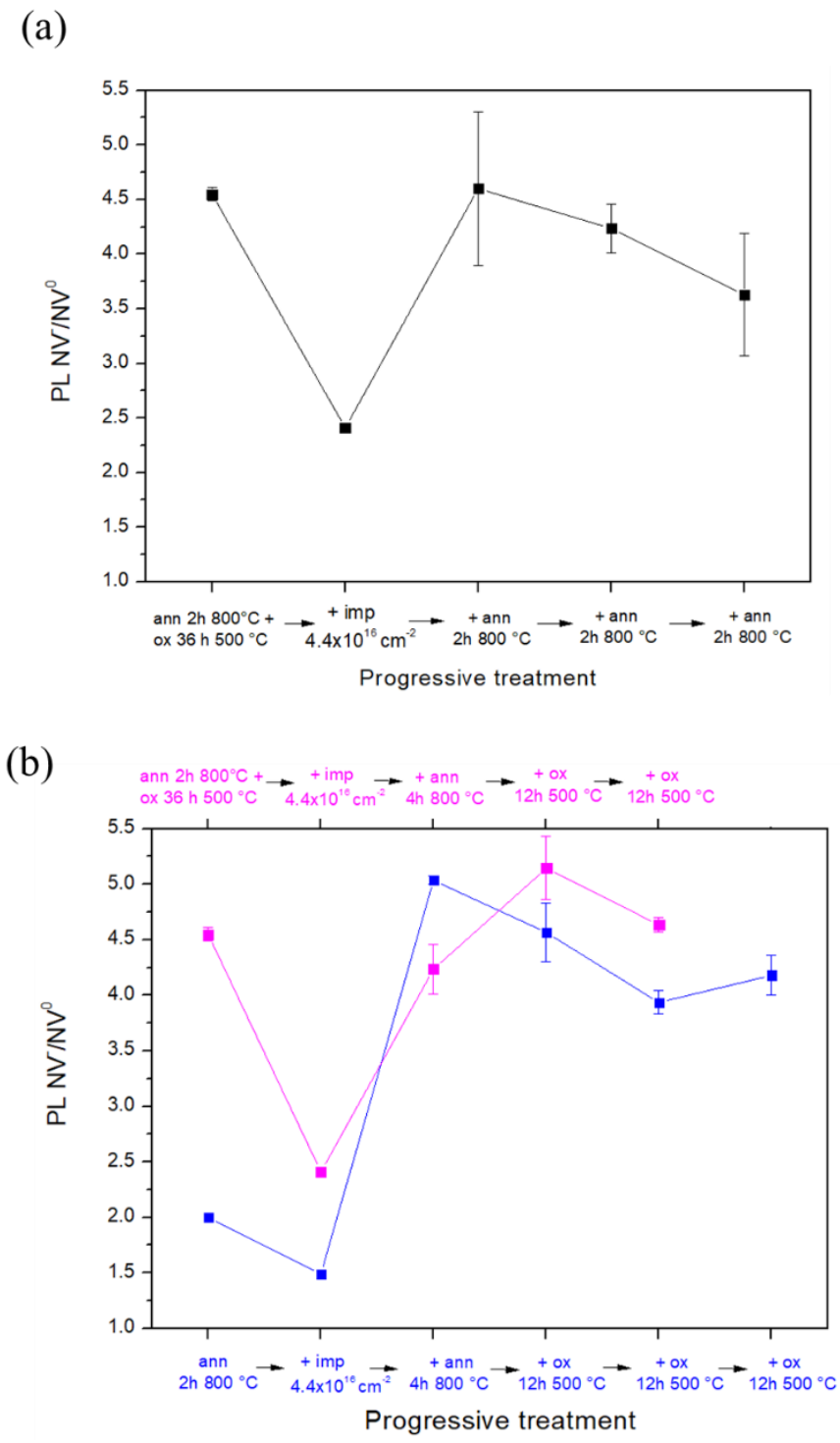

Figure C: NV^-/NV^0 PL ratio of implanted MSY-MND following re-annealing 3 successive times for 2h at 800 °C (a) and following progressive treatments of implantation, HTTA and oxidation for both previously oxidized and not-oxidized MSY-MND (b)

Appendix D

In this appendix a preliminary assessment of ODMR measures with implanted MSY-MND is presented. Data were acquired by researchers of the National Institute of Metrological Research INRiM (Torino).

As introduced in section 1.4.4, the peculiar electronic level structure of the NV^- center can be exploited to measure weak magnetic fields and small temperature variations, with interesting applications also in biosensing [65–67,79,179]. Figure D1 reports the electronic level structure of the NV^- center is reported. The ground state ($^3A_2$) and the excited state (^3E) are spin triplets (letters identify the type of orbitals symmetry). In the ground state, 3 spin configurations are possible. The state with $m_s = 0$, and the two states with $m_s = \pm 1$ (which degenerate in the absence of an external magnetic field). Due to the spin-orbit interaction, there is an energy difference between the state with $m_s = 0$ and the $m_s = \pm 1$ states. The latter are situations with an energy higher than the state $m_s = 0$ by a frequency value equal to $D_f = 2.87$ GHz. The same happens also with the excited states (^3E) with a frequency difference equal to $D_e = 1.42$ GHz.

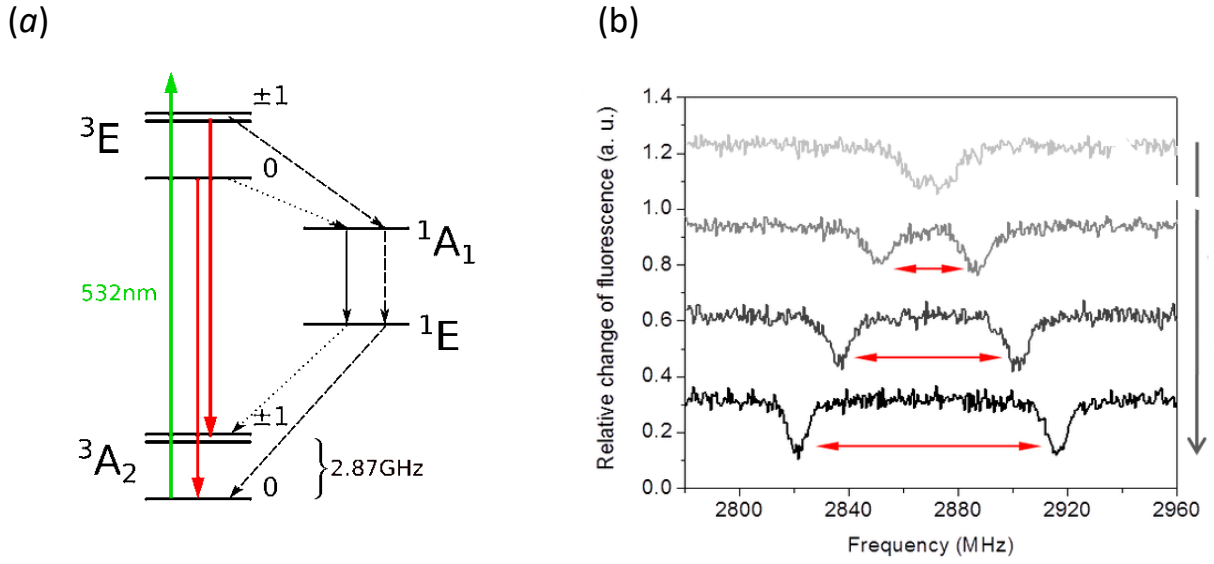

Figure D1: (a) level structure of the NV^- center [69]*; (b) examples of ODMR spectra with different applied magnetic fields* [70].

When exciting the center with a green laser source (typical wavelength of 532 nm), the system transits to the excited level while preserving its spin state. The relaxation to the ground state can occur through several channels, depending on its m_s spin state. The case $m_s = \pm 1$ presents two

possible relaxation channels. The first is through a radiative transition, which relaxes the system directly to the ground state while preserving the spin. This transition corresponds to a wavelength of 637 nm. The second relaxation channel occurs with 30% of probability through a non-radiative transition between ^3E and ^1A, a subsequent transition from state ^1A to state ^1E which emits infrared radiation at $\lambda = 1043$ nm, and finally another non-radiative path to the fundamental level, but with $m_s = 0$ (inter-system-crossing). If the excitation starts from the ground state $m_s = 0$ (and therefore the excited state is characterized by the same spin) the system has a very low probability of a non-radiative decay through the metastable states, and the relaxation occurs from the excited level ^3E directly to the fundamental level, emitting radiation at a wavelength of 637 nm. Therefore, given that $m_s = 0$ states are brighter than $m_s = \pm 1$ states, by exciting the system with a laser source and measuring the intensity of the emitted radiation, the electronic spin state in which the system is located can be inferred.

The NV^- center electronic structure can be perturbated by a magnetic field, through the Zeeman effect. This phenomenon occurs in presence of a magnetic field component parallel to the direction of the magnetic moment of the NV^- center (typically referred to as the z direction) [65]. In particular, the separation between the two states $m_s = +1$ and $m_s = -1$ is:

$$h\Delta\nu = 2g_e\mu_B B_z \tag{14}$$

where $g_e = 2.002;\ \mu_B = 9.27 \cdot 10^{-24} J;\ h = 6.626 \cdot 10^{-34} J\ s$

Thanks to these peculiar properties, by means of the Optically Detected Magnetic Resonance (ODMR) technique it is possible to measure the spin state of the NV^- system. In this technique, the NV^- center is continuously excited with a 532 nm laser source and a microwave field. The photoluminescence is measured as a function of the frequency of the microwaves applied to the sample. When the resonant frequency D = 2.87 GHz is reached, electrons are induced to transit from ground state $m_s = 0$ to $m_s = \pm 1$ states. Thus, the laser excitation will determine mostly transitions to excited $m_s = \pm 1$ states which relax in 30% of the cases through non-radiative paths. Therefore, in correspondence with the resonant frequency, the emission of the NV^- center decreases. Adding an external magnetic field, this "dark" state $m_s = \pm 1$ is split into two sub-level states. In this case, the ODMR measurement shows two dips (figure 13b) corresponding to the resonant frequencies of the system due to the transitions $m_s = 0 \rightarrow 1$ and $m_s = 0 \rightarrow -1$. The higher is the applied magnetic field, the larger will be the separation between those frequencies.

The intensity of the ODMR spectrum as a function of the frequency ν can be expressed as:

$$I(\nu) = R\left[1 - Cf\left(\frac{\nu-\nu_0}{\Delta\nu}\right)\right] \quad (15)$$

where R is the emission rate of the incident photons, C is the contrast (i.e.: the difference in the emission rate between the state $m_s = 0$ and the states $m_s = \pm 1$, corresponding to the resonant frequency), f is the function that fits best to the profile of the curve (Lorentzian curve), Δν is the peak width (FWHM), and ν_0 is the resonant frequency.

In addition to the magnetic field measurement, also temperature variations can be measured with this technique, due to their influence on NV complex spin levels [179]. Indeed, a higher local temperature results in a larger lattice spacing of the NV center, thus reducing the spin–spin interaction. As a result, while upon ambient conditions D_f is ~ 2.87 GHz, when temperature changes, the D_f parameter follows $\gamma = \frac{dD_f}{dT} \sim -74\ kHz\ K^{-1}$ [180]. Experimentally, the measurement is assessed by evaluating the frequency shift of the dips (towards higher frequency in the case of lower temperature and vice versa in the case of a higher temperature). Although theoretically the measure can be performed in the case of degenerate m_s level (single dip), possible internal strain (especially in ND) and the presence of the Earth's magnetic field determines a slight split in two undistinguishable dips whose convolution results in a larger dip which prevents a proper assessment of the measurement. Consequently, an external magnetic field is generally applied to completely separate the spin levels.

Measurements were conducted on MSY-MND following the subsequent treatments, selected from ND processed as described in sections 3.2.2 and 3.2.4:

S1: HTTA 2 h 800 °C (N_2) + air oxidation 36 h 500 °C + implantation H^+ 2 MeV F = 4.4×10^{16} cm^{-2} + HTTA 4 h 800 °C (N_2) + oxidation 12 h 500 °C

S2: HTTA 2 h 800 °C (N_2) + air oxidation 36 h 500 °C

Samples were dispersed in isopropyl alcohol, sonicated, deposited on a silicon substrate, dried and finally analyzed. The experimental setup included an excitation light (80 mW optical power) at 532 nm that was obtained from the second harmonic of a Nd:YAG laser with high power stability (Coherent Prometheus 100NE). The light was focused close to the bottom surface of the nanodiamond sample through an air objective (Olympus UPLANFL) with Numerical Aperture NA = 0.67. The diameter of the spot of the focused laser beam was ~ (10 × 10) μm^2. The power of the excitation light was attenuated down to 1 mW using a Neutral Density filter. An Acousto Optic

Modulator after the laser source was exploited to switch on and off the laser illumination on the sample. This solution allows to shine the laser on the sample only during the measurement time, reducing the total amount of light energy delivered to the sample. This is of key importance in biological applications. The microwave control was obtained by a commercial microwave generator (Keysight N5172B). The photoluminescence (PL) emission was spectrally filtered with a notch filter centered at 532 nm and a long-pass filter centered at 650 nm, and finally collected and detected by a single-photon avalanche detector (SPAD, SPCM-AQR 15, Perkin Elmer). The signal from the SPAD was used for the ODMR spectrum acquisition. Spatial resolution of the acquisition was within 1 μm^2, thus not allowing to ensure a measurement from a single ND.

Figure D2 shows examples of ODMR spectra acquired for samples S1 (a) and S2 (b). Starting from the latter, differential spectra were calculated (Figure D2 (c) and (d)) and the slope s in correspondence of the frequency of the first dip (differential signal = 0) was estimated.

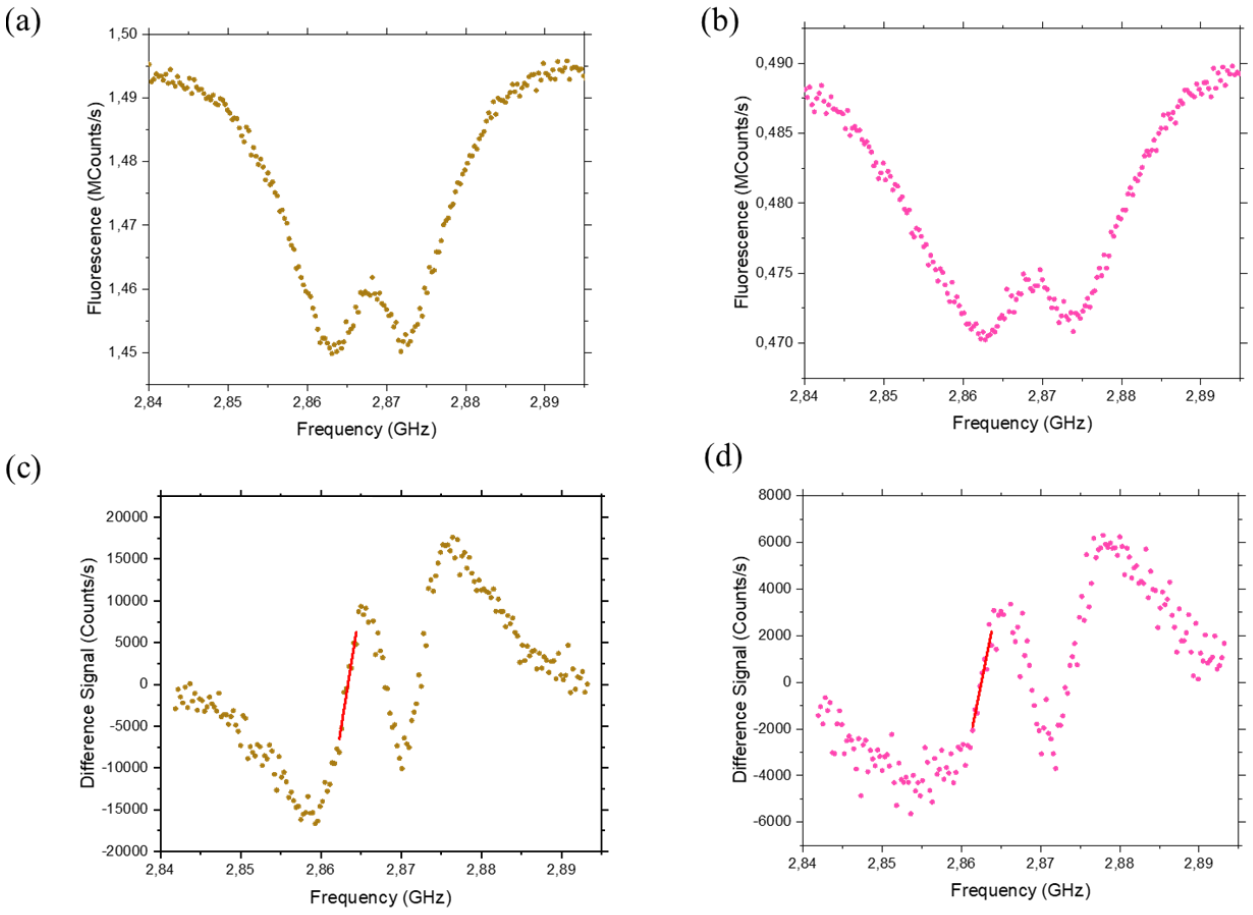

Figure D2: ODMR spectra of S1 (a) and S2 (b) MSY-MND and their respective differential spectra (c) and (d).

By repeating more times (at unchanged conditions) the measurement of the differential signal at this specific frequency, a distribution and the corresponding standard deviation $\sigma_{\Delta Fdiff}$ were obtained (temperature was kept constant at 26 °C with an incubator). The latter is then converted in $\sigma_{\Delta T} = \frac{\sigma_{\Delta F_{diff}}}{\gamma s}$, which corresponds to the minimum assessable temperature variation. It is worth noting that the standard deviation $\sigma_{\Delta Fdiff}$ (and thus $\sigma_{\Delta T}$) is proportional to $\frac{1}{\sqrt{N}} \alpha \frac{1}{\sqrt{\Delta t}}$, where N is the number of acquisitions and Δt the integration time. Therefore, the higher is the integration time, the lower will be $\sigma_{\Delta T}$. In order to define a parameter independent from the duration of the measurement, the sensitivity is defined as $\eta = \delta T_{min}\sqrt{\Delta t} = \sigma_{\Delta T}\sqrt{\Delta t}$.

As a preliminary assessment of the sensitivity of the processed ND, only 3 measurements from 3 different spots were performed for each sample, resulting in $\eta_{S1} = (5.5 \pm 0.6)\, K\, Hz^{-1/2}$ and $\eta_{S2} = (10.8 \pm 1.4)\, K\, Hz^{-1/2}$. Ion implanted samples showed a better sensitivity with respect to not-implanted ones, probably due to the higher amount of NV centers (and consequently NV^- centers) in each nanocrystal. Further analysis will be conducted in the future with larger statistics and other samples to verify which irradiation fluence and post-implantation processing better optimizes the sensitivity.

Appendix E

Filter	Mag.	Effective power (mW)
No Filter	10×	21
	20×	17,1
	50×	8,13
	100×	4,11
D1	10×	2,07
	20×	1,69
	50×	0,73
	100×	0,48
D2	10×	0,21
	20×	0,178
	50×	0,085
	100×	0,048
D3	10×	0,023
	20×	0,0196
	50×	0,0147
	100×	0,0165
D4	10×	0,021
	20×	0,02
	50×	0,0218
	100×	0,021

Table 2: actual laser power impinging on the sample as a function of the applied filter and objective, when acquiring Raman/photoluminescence spectra with Raman spectrometer Horiba JobinYvon HR800

Publications

ISI publications

1. G. Tomagra[§], P. Aprà[§], A. Battiato, C. Collà Ruvolo, A. Pasquarelli, A. Marcantoni, E. Carbone, V. Carabelli, P. Olivero, F. Picollo, "Micro graphite-patterned diamond sensors: “Towards the simultaneous in vitro detection of molecular release and action potentials generation from excitable cells", Carbon 152, 424-433 (2019)

   [§] these authors equally contributed to this work

2. L. Guidorzi, A. Re, F. Picollo, P. Aprà, F. Fantino, L. Martire, G. Artioli, L. Peruzzo, S. Boesso, V. Rigato, L. La Torre, A. Lo Giudice, “Multi-technique study of He+ micro-irradiation effects on natural quartz crystals contained in archaeological pottery”, Nuclear Instruments and Methods in Physics Research Section B: Beam Interactions with Materials and Atoms 479 (2020) 143-149

3. P. Aprà, J. Ripoll-Sau, J. Manzano-Santamaria, C. Munuera, J. Forneris, S. Ditalia Tchernij, P. Olivero, F. Picollo, E. Vittone, M.D. Ynsa, “Structural characterization of 8 MeV 11B implanted diamond”, Diamond & Related Materials 104 (2020) 107770

4. F. Gorrini, C. Dorigoni, D. Olivares-Postigo, R. Giri, P. Aprà, F. Picollo, A. Bifone, “Long-Lived Ensembles of Shallow NV^- Centers in Flat and Nanostructured Diamonds by Photoconversion”, ACS Applied Materials & Interfaces 13 (2021) 43221 − 43232

5. S. Ditalia Tchernij, T. Luehmann, E. Corte, F. Sardi, F. Picollo, P. Traina, M. Brajkovic, A. Crnjac, S. Pezzagna, Z Pastuovic, I.P. Degiovanni, E. Moreva, P. Aprà, P. Olivero, Z. Siketic, J. Meijer, M. Genovese, J. Forneris, "Fluorine-based color centers in diamond", Scientific Reports 10 (2020) 21537

6. P. Aprà, L. Mino, A. Battiato, P. Olivero, S. Sturari, M.C. Valsania, V. Varzi, F. Picollo, "Interaction of nanodiamonds with water: impact of surface chemistry on hydrophilicity, aggregation and electrical properties", Nanomaterials 11 (2021) 2740

Other publications

1. P. Aprà, A. Battiato, S. Ditalia Tchernij, J. Forneris, L. La Torre, L. Mino, V. Rigato, P. Olivero, F. Picollo, “Proton Beam Induced Fluorescence in 5 nm Detonation Nanodiamond” Laboratori Nazionali di Legnaro Annual Report 2017 (2017) 100-101

2. G. Peroni, L. Pacher, V. De Nadal, M. Campostrini, P. Aprà, A. Re, A. Lo Giudice, L. Guidorzi, P. Olivero, R. Cherubini, N. Cartiglia, V. Rigato, F. Picollo, “Fabrication and characterization of DIACELL diamond-based detectors for in vitro cellular radiobiology” ", Laboratori Nazionali di Legnaro Annual Report 2019 (2020) 126-127

3. P. Aprà, G. Tomagra, A. Battiato, S. Ditalia Tchernij, J. Forneris, D. Carlucci, L. La Torre, A. Marcantoni, V. Rigato, P. Olivero, V. Carabelli, F. Picollo, "MeV ion beam fabrication of diamond biosensors for action potentials detection", Laboratori Nazionali di Legnaro Annual Report 2018, (2019) 159-160

4. S. Ditalia Tchernij, G. Andrini, P. Aprà, M. Campostrini, D. Carlucci, E. Corte, I. Degiovanni, M. Genovese, L. La Torre, C. Marinelli, E. Moreva, V. Prestopino, V. Rigato, P. Traina, V. Varzi, G. Verona, C. Verona Rinati, P. Olivero, J. Forneris, F. Picollo, "Ion Beam Fabrication of Graphitic Structures in Single-Crystal Diamond for Electrically-Stimulated Luminescence”, Laboratori Nazionali di Legnaro Annual Report 2020, (2021) 79-80

Acknowledgements

Last, but not least, I would like to thank all the people who accompanied me during these years.

I thank my supervisor Prof. Ettore Vittone and my co-supervisor Dr. Federico Picollo for following me with enormous patience and availability, guiding me step by step in the development of the work.

I thank all the companions (and friends) of the bio-diamond group, namely Adam, Giulia T., Nour-Hanne, Sofia and Veronica for helping and supporting me in the daily activities and for filling the days with cheerfulness. A special thank to our head of the diamond group, Prof. Paolo Olivero, for the help in many data interpretation issues. I thank also Dr. Lorenzo Mino for his essential assistance in the chemical aspects of the work and in DRIFT spectroscopy, Dr. Giulia Petrini for theODMR measurements, Dr. Mirko Sacco and Prof. Alessandro Barge for their precious collaboration in the functionalization of ND, Dr. Valentina Boscaro and Prof. Margherita Gallicchio for the time generously dedicated performing the first in-vitro tests of the processed samples.

I thank all the other components/ex-components of the Solid-State Physics group, especially Alfio, Ale Re, Andrea A., Andrea M., Cecilia, Cristina, Elena, Elisa, Emilio, Fabio S. M., Fabio P., Fulvio, Giulia Per., Giulia Pet., Giusi, Greta, Jacopo, Laura, Leila, Marco, Selene, Slava and Valentina for the assistance in all daily works and for making our laboratory a happy environment.

I also want to thank all my family and friends for their priceless support, always sustaining me and ameliorating the hard days.

Finally, the most special thank goes to my beloved mother and father and my true angels looking from up there, Saetta and Rex.

Bibliography

1. Chan, J.M.; Xu, C. *Perspectives in Micro- and Nanotechnology for Biomedical Applications*; IMPERIAL COLLEGE PRESS, 2016; ISBN 978-1-78326-960-0.
2. McPhee, G.; Dalby, M.J.; Riehle, M.; Yin, H. Can common adhesion molecules and microtopography affect cellular elasticity? A combined atomic force microscopy and optical study. *Med. Biol. Eng. Comput.* **2010**, *48*, 1043–1053, doi:10.1007/s11517-010-0657-3.
3. Huang, S.; Ingber, D.E. Cell tension, matrix mechanics, and cancer development. *Cancer Cell* **2005**, *8*, 175–176, doi:10.1016/j.ccr.2005.08.009.
4. Alenghat, F.J.; Ingber, D.E. Mechanotransduction: All Signals Point to Cytoskeleton, Matrix, and Integrins. *Sci. STKE* **2002**, *2002*, doi:10.1126/stke.2002.119.pe6.
5. Qian, T.; Wang, Y. Micro/nano-fabrication technologies for cell biology. *Med. Biol. Eng. Comput.* **2010**, *48*, 1023–1032, doi:10.1007/s11517-010-0632-z.
6. Lim, C.T.; Han, J.; Guck, J.; Espinosa, H. Micro and nanotechnology for biological and biomedical applications. *Med. Biol. Eng. Comput.* **2010**, *48*, 941–943, doi:10.1007/s11517-010-0677-z.
7. Hosseini, S.; Espinosa-Hernandez, M.A.; Garcia-Ramirez, R.; Cerda-Kipper, A.S.; Reveles-Huizar, S.; Acosta-Soto, L. *BioMEMS*; Lecture Notes in Bioengineering; Springer Singapore: Singapore, 2021; ISBN 978-981-15-6381-2.
8. Mauritz, J.M.A.; Esposito, A.; Tiffert, T.; Skepper, J.N.; Warley, A.; Yoon, Y.-Z.; Cicuta, P.; Lew, V.L.; Guck, J.R.; Kaminski, C.F. Biophotonic techniques for the study of malaria-infected red blood cells. *Med. Biol. Eng. Comput.* **2010**, *48*, 1055–1063, doi:10.1007/s11517-010-0668-0.
9. Nanoparticles in biomedicine Available online: https://www.wichlab.com/nanometer-scale-comparison-nanoparticle-size-comparison-nanotechnology-chart-ruler-2/.
10. Tiwari, G.; Tiwari, R.; Sriwastawa, B.; Bhati, L.; Pandey, S.; Pandey, P.; Bannerjee, S.K. Drug delivery systems: An updated review. *Int. J. Pharm. Investig.* **2012**, *2*, 2–11, doi:10.4103/2230-973X.96920.
11. Ma, N.; Ma, C.; Li, C.; Wang, T.; Tang, Y.; Wang, H.; Mou, X.; Chen, Z.; He, N. Influence of Nanoparticle Shape, Size, and Surface Functionalization on Cellular Uptake. *J. Nanosci. Nanotechnol.* **2013**, *13*, 6485–6498, doi:10.1166/jnn.2013.7525.
12. Buschmann, M.D.; Carrasco, M.J.; Alishetty, S.; Paige, M.; Alameh, M.G.; Weissman, D. Nanomaterial Delivery Systems for mRNA Vaccines. *Vaccines* **2021**, *9*, 65, doi:10.3390/vaccines9010065.
13. Soppimath, K.S.; Aminabhavi, T.M.; Kulkarni, A.R.; Rudzinski, W.E. Biodegradable polymeric nanoparticles as drug delivery devices. *J. Control. Release* **2001**, *70*, 1–20.
14. Thakor, A.S.; Gambhir, S.S. Nanooncology: the future of cancer diagnosis and therapy. *CA. Cancer J. Clin. 63*, 395–418, doi:10.3322/caac.21199.

15. Maeda, H. The enhanced permeability and retention (EPR) effect in tumor vasculature: the key role of tumor-selective macromolecular drug targeting. *Adv. Enzyme Regul.* **2001**, *41*, 189–207.

16. Wicki, A.; Witzigmann, D.; Balasubramanian, V.; Huwyler, J. Nanomedicine in cancer therapy: challenges, opportunities, and clinical applications. *J. Control. Release* **2015**, *200*, 138–57, doi:10.1016/j.jconrel.2014.12.030.

17. Cho, K.; Wang, X.; Nie, S.; Chen, Z.G.; Shin, D.M. Therapeutic nanoparticles for drug delivery in cancer. *Clin. Cancer Res.* **2008**, *14*, 1310–6, doi:10.1158/1078-0432.CCR-07-1441.

18. Silva, F.; Cabral Campello, M.P.; Paulo, A. Radiolabeled Gold Nanoparticles for Imaging and Therapy of Cancer. *Materials (Basel).* **2020**, *14*, 4, doi:10.3390/ma14010004.

19. Kuncic, Z.; Lacombe, S. Nanoparticle radio-enhancement: Principles, progress and application to cancer treatment. *Phys. Med. Biol.* **2018**, *63*, doi:10.1088/1361-6560/aa99ce.

20. Wang, H.; Mu, X.; He, H.; Zhang, X.D. Cancer Radiosensitizers. *Trends Pharmacol. Sci.* **2018**, *39*, 24–48, doi:10.1016/j.tips.2017.11.003.

21. Zhang, X.D.; Luo, Z.; Chen, J.; Song, S.; Yuan, X.; Shen, X.; Wang, H.; Sun, Y.; Gao, K.; Zhang, L.; et al. Ultrasmall glutathione-protected gold nanoclusters as next generation radiotherapy sensitizers with high tumor uptake and high renal clearance. *Sci. Rep.* **2015**, *5*, 1–7, doi:10.1038/srep08669.

22. Goodman, C.M.; McCusker, C.D.; Yilmaz, T.; Rotello, V.M. Toxicity of gold nanoparticles functionalized with cationic and anionic side chains. *Bioconjug. Chem.* **2004**, *15*, 897–900, doi:10.1021/bc049951i.

23. Stefan, M.; Melnig, V.; Pricop, D.; Neagu, A.; Mihasan, M.; Tartau, L.; Hritcu, L. Attenuated effects of chitosan-capped gold nanoparticles on LPS-induced toxicity in laboratory rats. *Mater. Sci. Eng. C* **2013**, *33*, 550–556, doi:10.1016/j.msec.2012.09.031.

24. Murthy, S.K. Nanoparticles in modern medicine: state of the art and future challenges. *Int. J. Nanomedicine* **2007**, *2*, 129–41.

25. Kreuter, J.; Ramge, P.; Petrov, V.; Hamm, S.; Gelperina, S.E.; Engelhardt, B.; Alyautdin, R.; Von Briesen, H.; Begley, D.J. Direct evidence that polysorbate-80-coated poly(butylcyanoacrylate) nanoparticles deliver drugs to the CNS via specific mechanisms requiring prior binding of drug to the nanoparticles. *Pharm. Res.* **2003**, *20*, 409–416, doi:10.1023/A:1022604120952.

26. NAD project Web Page Available online: http://www.nadproject.eu/.

27. A Frazer, R. Use of Silver Nanoparticles in HIV Treatment Protocols: A Research Proposal. *J. Nanomed. Nanotechnol.* **2011**, *03*, doi:10.4172/2157-7439.1000127.

28. Elechiguerra, J.L.; Burt, J.L.; Morones, J.R.; Camacho-Bragado, A.; Gao, X.; Lara, H.H.; Yacaman, M.J. Interaction of silver nanoparticles with HIV-1. *J. Nanobiotechnology* **2005**, *3*, 6, doi:10.1186/1477-3155-3-6.

29. Shen, Z.; Wu, A.; Chen, X. Iron Oxide Nanoparticle Based Contrast Agents for Magnetic Resonance Imaging. *Mol. Pharm.* **2017**, *14*, 1352–1364, doi:10.1021/acs.molpharmaceut.6b00839.

30. Bauer, L.M.; Situ, S.F.; Griswold, M.A.; Samia, A.C.S. High-performance iron oxide

nanoparticles for magnetic particle imaging – guided hyperthermia (hMPI). *Nanoscale* **2016**, *8*, 12162–12169, doi:10.1039/C6NR01877G.

31. GFP Sigma Aldrich. Available at: https://www.sigmaaldrich.com/IT/it/product/sigma/cll1031

32. Quantum dots size-dependent fluorescence. Available at: https://news.samsung.com/global/why-are-quantum-dot-displays-so-good

33. Ibnaouf, K.H.; Prasad, S.; Hamdan, A.; AlSalhi, M.; Aldwayyan, A.S.; Zaman, M.B.; Masilamani, V. Photoluminescence spectra of CdSe/ZnS quantum dots in solution. *Spectrochim. Acta Part A Mol. Biomol. Spectrosc.* **2014**, *121*, 339–345, doi:10.1016/j.saa.2013.10.089.

34. Chen, N.; He, Y.; Su, Y.; Li, X.; Huang, Q.; Wang, H.; Zhang, X.; Tai, R.; Fan, C. The cytotoxicity of cadmium-based quantum dots. *Biomaterials* **2012**, *33*, 1238–1244, doi:10.1016/j.biomaterials.2011.10.070.

35. Nistor, P.A.; May, P.W.; Tamagnini, F.; Randall, A.D.; Caldwell, M.A. Long-term culture of pluripotent stem-cell-derived human neurons on diamond – A substrate for neurodegeneration research and therapy. *Biomaterials* **2015**, *61*, 139–149, doi:10.1016/j.biomaterials.2015.04.050.

36. Tang, L.; Tsai, C.; Gerberich, W.W.; Kruckeberg, L.; Kania, D.R. Biocompatibility of chemical-vapour-deposited diamond. *Biomaterials* **1995**, *16*, 483–488, doi:10.1016/0142-9612(95)98822-V.

37. Alcaide, M.; Taylor, A.; Fjorback, M.; Zachar, V.; Pennisi, C.P. Boron-Doped Nanocrystalline Diamond Electrodes for Neural Interfaces: In vivo Biocompatibility Evaluation. *Front. Neurosci.* **2016**, *10*, doi:10.3389/fnins.2016.00087.

38. Vogel, T.; Meijer, J.; Zaitsev, A. Highly effective p-type doping of diamond by MeV-ion implantation of boron. *Diam. Relat. Mater.* **2004**, *13*, 1822–1825, doi:10.1016/j.diamond.2004.04.005.

39. Lühmann, T.; Wunderlich, R.; Schmidt-Grund, R.; Barzola-Quiquia, J.; Esquinazi, P.; Grundmann, M.; Meijer, J. Investigation of the graphitization process of ion-beam irradiated diamond using ellipsometry, Raman spectroscopy and electrical transport measurements. *Carbon N. Y.* **2017**, *121*, 512–517, doi:10.1016/j.carbon.2017.05.093.

40. Picollo, F.; Olivero, P.; Bellotti, F.; Pastuović, Ž.; Skukan, N.; Giudice, A. Lo; Amato, G.; Jakšić, M.; Vittone, E. Formation of buried conductive micro-channels in single crystal diamond with MeV C and He implantation. *Diam. Relat. Mater.* **2010**, *19*, 466–469, doi:10.1016/j.diamond.2010.01.005.

41. Olivero, P.; Amato, G.; Bellotti, F.; Budnyk, O.; Colombo, E.; Jakšić, M.; Manfredotti, C.; Pastuović, Ž.; Picollo, F.; Skukan, N.; et al. Direct fabrication of three-dimensional buried conductive channels in single crystal diamond with ion microbeam induced graphitization. *Diam. Relat. Mater.* **2009**, *18*, 870–876, doi:10.1016/j.diamond.2008.10.068.

42. Zazula, J. On Graphite Transformations at High Temperature and Pressure Induced by Absorption of the LHC Beam. *LHC Proj. Note n.78* **1997**.

43. Carbon allotropes Available online: https://www.cd-bioparticles.com/support/synthesis-of-carbon-allotropes.html.

44. Pierson, H.O. Handbook of Carbon, Graphite, Diamond and Fullerenes. *Handb. Carbon, Graph. Diam. Fullerenes* **1993**, 25–69, doi:http://dx.doi.org/10.1016/B978-0-8155-1339-1.50008-6.

45. Diamond lattice cell Available online: https://tex.stackexchange.com/questions/141363/draw-realistic-3d-crystal-structures-diamond.

46. Zaitsev, A.M. *Optical Properties of Diamond*; Springer Berlin Heidelberg: Berlin, Heidelberg, 2001; ISBN 978-3-642-08585-7.

47. Auciello, O.; Aslam, D.M. Review on advances in microcrystalline, nanocrystalline and ultrananocrystalline diamond films-based micro/nano-electromechanical systems technologies. *J. Mater. Sci.* **2021**, *56*, 7171–7230, doi:10.1007/s10853-020-05699-9.

48. Zaitzev, A.M. Optical Properties of Diamond. **2001**, 508, doi:10.1007/978-3-662-04548-0.

49. Akaishi, M.; Kanda, H.; Yamaoka, S. Synthesis of diamond from graphite-carbonate system under very high temperature and pressure. *J. Cryst. Growth* **1990**, *104*, 578–581, doi:10.1016/0022-0248(90)90159-I.

50. Nor, R.M.; Bakar, S.A.; Thandavan, T.M.; Rusop, M. Diamond: Synthesis, Characterisation and Applications. In; 2010; pp. 195–217.

51. Butler, J.E.; Windischmann, H. Developments in CVD-Diamond Synthesis During the Past Decade. *MRS Bull.* **1998**, *23*, 22–27, doi:10.1557/S0883769400029316.

52. Mochalin, V.N.; Shenderova, O.; Ho, D.; Gogotsi, Y. The properties and applications of nanodiamonds. *Nat. Nanotechnol.* **2012**, *7*, 11–23, doi:10.1038/nnano.2011.209.

53. Burns, R.C.; Chumakov, A.I.; Connell, S.H.; Dube, D.; Godfried, H.P.; Hansen, J.O.; Härtwig, J.; Hoszowska, J.; Masiello, F.; Mkhonza, L.; et al. HPHT growth and x-ray characterization of high-quality type IIa diamond. *J. Phys. Condens. Matter* **2009**, *21*, doi:10.1088/0953-8984/21/36/364224.

54. Smit, J. Theory of Raman Scattering in Solids. *Phys. Rev. B* **1971**, *3*, 4330–4337, doi:10.1103/PhysRevB.3.4330.

55. Shih, W.-C.; Bechtel, K.B.; Feld, M.S. Noninvasive glucose sensing with Raman spectroscopy. *Anal. Chem. vivo glucose Meas. Hoboken, NJ John Wiley \& Sons* **2009**, 391–419.

56. Cantarero, A. *Raman Scattering Applied to Materials Science*; 2015; Vol. 9;.

57. Becker, J.N.; Neu, E. The silicon vacancy center in diamond. In; 2020; pp. 201–235.

58. Iwasaki, T.; Ishibashi, F.; Miyamoto, Y.; Doi, Y.; Kobayashi, S.; Miyazaki, T.; Tahara, K.; Jahnke, K.D.; Rogers, L.J.; Naydenov, B.; et al. Germanium-Vacancy Single Color Centers in Diamond. *Sci. Rep.* **2015**, *5*, 12882, doi:10.1038/srep12882.

59. Iwasaki, T.; Miyamoto, Y.; Taniguchi, T.; Siyushev, P.; Metsch, M.H.; Jelezko, F.; Hatano, M. Tin-Vacancy Quantum Emitters in Diamond. *Phys. Rev. Lett.* **2017**, *119*, 253601, doi:10.1103/PhysRevLett.119.253601.

60. Ditalia Tchernij, S.; Lühmann, T.; Herzig, T.; Küpper, J.; Damin, A.; Santonocito, S.; Signorile, M.; Traina, P.; Moreva, E.; Celegato, F.; et al. Single-Photon Emitters in Lead-Implanted Single-Crystal Diamond. *ACS Photonics* **2018**, *5*, 4864–4871,

doi:10.1021/acsphotonics.8b01013.

61. Doherty, M.W.; Manson, N.B.; Delaney, P.; Jelezko, F.; Wrachtrup, J.; Hollenberg, L.C.L. The nitrogen-vacancy colour centre in diamond. *Phys. Rep.* **2013**, *528*, 1–45, doi:10.1016/j.physrep.2013.02.001.

62. Jelezko, J.W. and F. Processing quantum information in diamond. *J. Phys. Condens. Matter* **2006**, *18*, S807.

63. Hui, Y.Y.; Cheng, C.-A.; Chen, O.Y.; Chang, H.-C. Bioimaging and Quantum Sensing Using NV Centers in Diamond Nanoparticles. In; 2016; pp. 109–137.

64. Petráková, V.; Taylor, A.; Kratochvílová, I.; Fendrych, F.; Vacík, J.; Kučka, J.; Štursa, J.; Cígler, P.; Ledvina, M.; Fišerová, A.; et al. Luminescence of Nanodiamond Driven by Atomic Functionalization: Towards Novel Detection Principles. *Adv. Funct. Mater.* **2012**, *22*, 812–819, doi:10.1002/adfm.201101936.

65. Schirhagl, R.; Chang, K.; Loretz, M.; Degen, C.L. Nitrogen-Vacancy Centers in Diamond: Nanoscale Sensors for Physics and Biology. *Annu. Rev. Phys. Chem.* **2014**, *65*, 83–105, doi:10.1146/annurev-physchem-040513-103659.

66. Kucsko, G.; Maurer, P.C.; Yao, N.Y.; Kubo, M.; Noh, H.J.; Lo, P.K.; Park, H.; Lukin, M.D. Nanometre-scale thermometry in a living cell. *Nature* **2013**, *500*, 54–58, doi:10.1038/nature12373.

67. Barry, J.F.; Turner, M.J.; Schloss, J.M.; Glenn, D.R.; Song, Y.; Lukin, M.D.; Park, H.; Walsworth, R.L. Optical magnetic detection of single-neuron action potentials using quantum defects in diamond. *Proc. Natl. Acad. Sci.* **2016**, *113*, 14133–14138, doi:10.1073/pnas.1601513113.

68. Hemelaar, S.R.; de Boer, P.; Chipaux, M.; Zuidema, W.; Hamoh, T.; Martinez, F.P.; Nagl, A.; Hoogenboom, J.P.; Giepmans, B.N.G.; Schirhagl, R. Nanodiamonds as multi-purpose labels for microscopy. *Sci. Rep.* **2017**, *7*, 720, doi:10.1038/s41598-017-00797-2.

69. Magnetometry with Single NV centers in diamond Available online: https://www.qolah.org/research/nv_v2/nv_v2.html.

70. Nanodiamonds for high-resolution sensing, Prof M. Tobar's group at University of Western Australia.

71. Danilenko, V. V. On the history of the discovery of nanodiamond synthesis. *Phys. Solid State* **2004**, *46*, 595–599, doi:10.1134/1.1711431.

72. Boudou, J.-P.; Curmi, P.A.; Jelezko, F.; Wrachtrup, J.; Aubert, P.; Sennour, M.; Balasubramanian, G.; Reuter, R.; Thorel, A.; Gaffet, E. High yield fabrication of fluorescent nanodiamonds. *Nanotechnology* **2009**, *20*, 235602, doi:10.1088/0957-4484/20/23/235602.

73. Frenklach, M.; Howard, W.; Huang, D.; Yuan, J.; Spear, K.E.; Koba, R. Induced nucleation of diamond powder. *Appl. Phys. Lett.* **1991**, *59*, 546–548, doi:10.1063/1.105434.

74. Yang, G.-W.; Wang, J.-B.; Liu, Q.-X. Preparation of nano-crystalline diamonds using pulsed laser induced reactive quenching. *J. Phys. Condens. Matter* **1998**, *10*, 7923–7927, doi:10.1088/0953-8984/10/35/024.

75. Datta, A.; Kirca, M.; Fu, Y.; To, A.C. Surface structure and properties of functionalized

nanodiamonds: a first-principles study. *Nanotechnology* **2011**, *22*, 065706, doi:10.1088/0957-4484/22/6/065706.

76. Guarina, L.; Calorio, C.; Gavello, D.; Moreva, E.; Traina, P.; Battiato, A.; Tchernij, S.D.; Forneris, J.; Gai, M.; Picollo, F.; et al. Nanodiamonds-induced effects on neuronal firing of mouse hippocampal microcircuits. *arXiv* **2018**.

77. McGuinness, L.P.; Yan, Y.; Stacey, A.; Simpson, D.A.; Hall, L.T.; Maclaurin, D.; Prawer, S.; Mulvaney, P.; Wrachtrup, J.; Caruso, F.; et al. Quantum measurement and orientation tracking of fluorescent nanodiamonds inside living cells. *Nat. Nanotechnol.* **2011**, *6*, 358–363, doi:10.1038/nnano.2011.64.

78. Hui, Y.Y.; Cheng, C.-L.; Chang, H.-C. Nanodiamonds for optical bioimaging. *J. Phys. D. Appl. Phys.* **2010**, *43*, 374021, doi:10.1088/0022-3727/43/37/374021.

79. Chipaux, M.; van der Laan, K.J.; Hemelaar, S.R.; Hasani, M.; Zheng, T.; Schirhagl, R. Nanodiamonds and Their Applications in Cells. *Small* **2018**, *14*, 1704263, doi:10.1002/smll.201704263.

80. Guarina, L.; Calorio, C.; Gavello, D.; Moreva, E.; Traina, P.; Battiato, A.; Ditalia Tchernij, S.; Forneris, J.; Gai, M.; Picollo, F.; et al. Nanodiamonds-induced effects on neuronal firing of mouse hippocampal microcircuits. *Sci. Rep.* **2018**, *8*, 1–14, doi:10.1038/s41598-018-20528-5.

81. Smith, B.R.; Gruber, D.; Plakhotnik, T. The effects of surface oxidation on luminescence of nano diamonds. *Diam. Relat. Mater.* **2010**, *19*, 314–318, doi:10.1016/j.diamond.2009.12.009.

82. Picollo, F.; Mino, L.; Battiato, A.; Ditalia Tchernij, S.; Forneris, J.; Martina, K.; Sacco, M.; Tagliapietra, S.; Vittone, E.; Olivero, P.; et al. Synthesis and characterization of porphyrin functionalized nanodiamonds. *Diam. Relat. Mater.* **2019**, *91*, 22–28, doi:10.1016/j.diamond.2018.11.001.

83. Chung, P.-H.; Perevedentseva, E.; Tu, J.-S.; Chang, C.C.; Cheng, C.-L. Spectroscopic study of bio-functionalized nanodiamonds. *Diam. Relat. Mater.* **2006**, *15*, 622–625, doi:10.1016/j.diamond.2005.11.019.

84. Merz, V.; Lenhart, J.; Vonhausen, Y.; Ortiz-Soto, M.E.; Seibel, J.; Krueger, A. Zwitterion-Functionalized Detonation Nanodiamond with Superior Protein Repulsion and Colloidal Stability in Physiological Media. *Small* **2019**, *15*, 1901551, doi:10.1002/smll.201901551.

85. Meinhardt, T.; Lang, D.; Dill, H.; Krueger, A. Pushing the Functionality of Diamond Nanoparticles to New Horizons: Orthogonally Functionalized Nanodiamond Using Click Chemistry. *Adv. Funct. Mater.* **2011**, *21*, 494–500, doi:10.1002/adfm.201001219.

86. Li, X.; Shao, J.; Qin, Y.; Shao, C.; Zheng, T.; Ye, L. TAT-conjugated nanodiamond for the enhanced delivery of doxorubicin. *J. Mater. Chem.* **2011**, *21*, 7966, doi:10.1039/c1jm10653h.

87. van der Laan, K.; Hasani, M.; Zheng, T.; Schirhagl, R. Nanodiamonds for In Vivo Applications. *Small* **2018**, *14*, 1703838, doi:10.1002/smll.201703838.

88. Leo, W.R. *Techniques for Nuclear and Particle Physics Experiments*; Springer Berlin Heidelberg: Berlin, Heidelberg, 1994; ISBN 978-3-540-57280-0.

89. Ziegler, J.F.; Ziegler, M.D.; Biersack, J.P. SRIM – The stopping and range of ions in

matter (2010). *Nucl. Instruments Methods Phys. Res. Sect. B Beam Interact. with Mater. Atoms* **2010**, *268*, 1818–1823, doi:10.1016/j.nimb.2010.02.091.

90. Uzan-Saguy, C.; Cytermann, C.; Brener, R.; Richter, V.; Shaanan, M.; Kalish, R. Damage threshold for ion-beam induced graphitization of diamond. *Appl. Phys. Lett.* **1995**, *67*, 1194–1196, doi:10.1063/1.115004.

91. Battiato, A.; Lorusso, M.; Bernardi, E.; Picollo, F.; Bosia, F.; Ugues, D.; Zelferino, A.; Damin, A.; Baima, J.; Pugno, N.M.; et al. Softening the ultra-stiff: Controlled variation of Young's modulus in single-crystal diamond by ion implantation. *Acta Mater.* **2016**, *116*, 95–103, doi:10.1016/j.actamat.2016.06.019.

92. Hickey, D.P.; Jones, K.S.; Elliman, R.G. Amorphization and graphitization of single-crystal diamond — A transmission electron microscopy study. *Diam. Relat. Mater.* **2009**, *18*, 1353–1359, doi:10.1016/j.diamond.2009.08.012.

93. Gippius, A.A.; Khmelnitskiy, R.A.; Dravin, V.A.; Tkachenko, S.D. Formation and characterization of graphitized layers in ion-implanted diamond. *Diam. Relat. Mater.* **1999**, *8*, 1631–1634, doi:10.1016/S0925-9635(99)00047-3.

94. Prins, J.F. Onset of hopping conduction in carbon-ion-implanted diamond. *Phys. Rev. B* **1985**, *31*, 2472–2478, doi:10.1103/PhysRevB.31.2472.

95. Olivero, P.; Rubanov, S.; Reichart, P.; Gibson, B.C.; Huntington, S.T.; Rabeau, J.R.; Greentree, A.D.; Salzman, J.; Moore, D.; Jamieson, D.N.; et al. Characterization of three-dimensional microstructures in single-crystal diamond. *Diam. Relat. Mater.* **2006**, *15*, 1614–1621, doi:10.1016/j.diamond.2006.01.018.

96. Bosia, F.; Argiolas, N.; Bazzan, M.; Olivero, P.; Picollo, F.; Sordini, A.; Vannoni, M.; Vittone, E. Modification of the structure of diamond with MeV ion implantation. *Diam. Relat. Mater.* **2011**, *20*, 774–778, doi:10.1016/j.diamond.2011.03.025.

97. Picollo, F.; Battiato, A.; Bernardi, E.; Plaitano, M.; Franchino, C.; Gosso, S.; Pasquarelli, A.; Carbone, E.; Olivero, P.; Carabelli, V. All-carbon multi-electrode array for real-time in vitro measurements of oxidizable neurotransmitters. *Sci. Rep.* **2016**, *6*, 20682, doi:10.1038/srep20682.

98. Picollo, F.; Battiato, A.; Bernardi, E.; Marcantoni, A.; Pasquarelli, A.; Carbone, E.; Olivero, P.; Carabelli, V. Microelectrode Arrays of Diamond-Insulated Graphitic Channels for Real-Time Detection of Exocytotic Events from Cultured Chromaffin Cells and Slices of Adrenal Glands. *Anal. Chem.* **2016**, *88*, 7493–7499, doi:10.1021/acs.analchem.5b04449.

99. Suzuki, I.; Fukuda, M.; Shirakawa, K.; Jiko, H.; Gotoh, M. Carbon nanotube multi-electrode array chips for noninvasive real-time measurement of dopamine, action potentials, and postsynaptic potentials. *Biosens. Bioelectron.* **2013**, *49*, 270–275, doi:10.1016/j.bios.2013.05.023.

100. Picollo, F.; Gosso, S.; Vittone, E.; Pasquarelli, A.; Carbone, E.; Olivero, P.; Carabelli, V. A New Diamond Biosensor with Integrated Graphitic Microchannels for Detecting Quantal Exocytic Events from Chromaffin Cells. *Adv. Mater.* **2013**, *25*, 4696–4700, doi:10.1002/adma.201300710.

101. Tomagra, G.; Aprà, P.; Battiato, A.; Collà Ruvolo, C.; Pasquarelli, A.; Marcantoni, A.; Carbone, E.; Carabelli, V.; Olivero, P.; Picollo, F. Micro graphite-patterned diamond sensors: Towards the simultaneous in vitro detection of molecular release and action

potentials generation from excitable cells. *Carbon N. Y.* **2019**, *152*, doi:10.1016/j.carbon.2019.06.035.

102. Meijer, J.; Burchard, B.; Domhan, M.; Wittmann, C.; Gaebel, T.; Popa, I.; Jelezko, F.; Wrachtrup, J. Generation of single color centers by focused nitrogen implantation. *Appl. Phys. Lett.* **2005**, *87*, 261909, doi:10.1063/1.2103389.

103. Bogdanov, S.A.; Gorbachev, A.M.; Radishev, D.B.; Vikharev, A.L.; Lobaev, M.A.; Gusev, S.A.; Tatarsky, D.A.; Bolshedvorskii, S. V.; Akimov, A. V.; Chernov, V. V. Creation of Localized NV Center Ensembles in CVD Diamond by Electron Beam Irradiation. *Tech. Phys. Lett.* **2019**, *45*, 281–284, doi:10.1134/S1063785019030222.

104. Nöbauer, T.; Buczak, K.; Angerer, A.; Putz, S.; Steinhauser, G.; Akbarzadeh, J.; Peterlik, H.; Majer, J.; Schmiedmayer, J.; Trupke, M. Creation of ensembles of nitrogen-vacancy centers in diamond by neutron and electron irradiation. **2013**, 1–12.

105. Waldermann, F.C.; Olivero, P.; Nunn, J.; Surmacz, K.; Wang, Z.Y.; Jaksch, D.; Taylor, R.A.; Walmsley, I.A.; Draganski, M.; Reichart, P.; et al. Creating diamond color centers for quantum optical applications. *Diam. Relat. Mater.* **2007**, *16*, 1887–1895, doi:10.1016/j.diamond.2007.09.009.

106. Aprà, P.; Battiato, A.; Tchernij, S.D.; Forneris, J. Proton Beam Induced Fluorescence in 5 nm Detonation Nanodiamond. 5–6.

107. Wu, W.; Fahy, S. Molecular-dynamics study of single-atom radiation damage in diamond. *Phys. Rev. B* **1994**, *49*, 3030–3035, doi:10.1103/PhysRevB.49.3030.

108. Pezzagna, S.; Rogalla, D.; Wildanger, D.; Meijer, J.; Zaitsev, A. Creation and nature of optical centres in diamond for single-photon emission—overview and critical remarks. *New J. Phys.* **2011**, *13*, 035024, doi:10.1088/1367-2630/13/3/035024.

109. Davies, G.; Hamer, M.F. Optical Studies of the 1.945 eV Vibronic Band in Diamond. *Proc. R. Soc. A Math. Phys. Eng. Sci.* **1976**, *348*, 285–298, doi:10.1098/rspa.1976.0039.

110. De La Puente, G.; Pis, J.J.; Menéndez, J.A.; Grange, P. Thermal stability of oxygenated functions in activated carbons. *J. Anal. Appl. Pyrolysis* **1997**, *43*, 125–138, doi:10.1016/S0165-2370(97)00060-0.

111. Osswald, S.; Yushin, G.; Mochalin, V.; Kucheyev, S.O.; Gogotsi, Y. Control of sp 2 /sp 3 Carbon Ratio and Surface Chemistry of Nanodiamond Powders by Selective Oxidation in Air. *J. Am. Chem. Soc.* **2006**, *128*, 11635–11642, doi:10.1021/ja063303n.

112. Shenderova, O.; Koscheev, A.; Zaripov, N.; Petrov, I.; Skryabin, Y.; Detkov, P.; Turner, S.; Van Tendeloo, G. Surface Chemistry and Properties of Ozone-Purified Detonation Nanodiamonds. *J. Phys. Chem. C* **2011**, *115*, 9827–9837, doi:10.1021/jp1102466.

113. Stehlik, S.; Varga, M.; Ledinsky, M.; Jirasek, V.; Artemenko, A.; Kozak, H.; Ondic, L.; Skakalova, V.; Argentero, G.; Pennycook, T.; et al. Size and Purity Control of HPHT Nanodiamonds down to 1 nm. *J. Phys. Chem. C* **2015**, *119*, 27708–27720, doi:10.1021/acs.jpcc.5b05259.

114. Jarre, G.; Heyer, S.; Memmel, E.; Meinhardt, T.; Krueger, A. Synthesis of nanodiamond derivatives carrying amino functions and quantification by a modified Kaiser test. *Beilstein J. Org. Chem.* **2014**, *10*, 2729–2737, doi:10.3762/bjoc.10.288.

115. Kozak, H.; Artemenko, A.; Čermák, J.; Švrček, V.; Kromka, A.; Rezek, B. Oxidation and

reduction of nanodiamond particles in colloidal solutions by laser irradiation or radio-frequency plasma treatment. *Vib. Spectrosc.* **2016**, *83*, 108–114, doi:10.1016/j.vibspec.2016.01.010.

116. Krueger, A. New Carbon Materials: Biological Applications of Functionalized Nanodiamond Materials. *Chem. - A Eur. J.* **2008**, *14*, 1382–1390, doi:10.1002/chem.200700987.

117. Ristein, J. The Physics of Hydrogen-Terminated Diamond Surfaces. In Proceedings of the AIP Conference Proceedings; AIP, 2005; Vol. 772, pp. 377–380.

118. Maier, F.; Ristein, J.; Ley, L. Electron affinity of plasma-hydrogenated and chemically oxidized diamond (100) surfaces. *Phys. Rev. B - Condens. Matter Mater. Phys.* **2001**, *64*, 1–7, doi:10.1103/PhysRevB.64.165411.

119. Ristein, J. Diamond surfaces: Familiar and amazing. *Appl. Phys. A Mater. Sci. Process.* **2006**, *82*, 377–384, doi:10.1007/s00339-005-3363-5.

120. Maier, F.; Riedel, M.; Mantel, B.; Ristein, J.; Ley, L. Origin of Surface Conductivity in Diamond. *Phys. Rev. Lett.* **2000**, *85*, 3472–3475.

121. Ostrovskaya, L.; Perevertailo, V.; Ralchenko, V.; Dementjev, A.; Loginova, O. Wettability and surface energy of oxidized and hydrogen plasma-treated diamond films. *Diam. Relat. Mater.* **2002**, *11*, 845–850, doi:10.1016/S0925-9635(01)00636-7.

122. Kaibara, Y.; Sugata, K.; Tachiki, M.; Umezawa, H.; Kawarada, H. Control wettability of the hydrogen-terminated diamond surface and the oxidized diamond surface using an atomic force microscope. *Diam. Relat. Mater.* **2003**, *12*, 560–564, doi:10.1016/S0925-9635(02)00373-4.

123. Seshan, V.; Ullien, D.; Castellanos-Gomez, A.; Sachdeva, S.; Murthy, D.H.K.; Savenije, T.J.; Ahmad, H.A.; Nunney, T.S.; Janssens, S.D.; Haenen, K.; et al. Hydrogen termination of CVD diamond films by high-temperature annealing at atmospheric pressure. *J. Chem. Phys.* **2013**, *138*, doi:10.1063/1.4810866.

124. Petit, T.; Girard, H.A.; Combis-Schlumberger, M.; Grall, R.; Delic, J.; Morel-Altmeyer, S.; Bergonzo, P.; Chevillard, S.; Arnault, J.C. Nanodiamond as a multimodal platform for drug delivery and radiosensitization of tumor cells. In Proceedings of the Proceedings of the 13th IEEE Conference on Nanotechnology, Beijing, China, August 5-8, 2013; 2013; pp. 174–178.

125. Grall, R.; Girard, H.; Saad, L.; Petit, T.; Gesset, C.; Combis-Schlumberger, M.; Paget, V.; Delic, J.; Arnault, J.C.; Chevillard, S. Impairing the radioresistance of cancer cells by hydrogenated nanodiamonds. *Biomaterials* **2015**, *61*, 290–298, doi:10.1016/j.biomaterials.2015.05.034.

126. Kurzyp, M.; Girard, H.A.; Cheref, Y.; Brun, E.; Sicard-Roselli, C.; Saada, S.; Arnault, J.C. Hydroxyl radical production induced by plasma hydrogenated nanodiamonds under X-ray irradiation. *Chem. Commun.* **2017**, *53*, 1237–1240, doi:10.1039/c6cc08895c.

127. Kondo, T.; Neitzel, I.; Mochalin, V.N.; Urai, J.; Yuasa, M.; Gogotsi, Y. Electrical conductivity of thermally hydrogenated nanodiamond powders. *J. Appl. Phys.* **2013**, *113*, 10–15, doi:10.1063/1.4809549.

128. Denisov, S.A.; Sokolina, G.A.; Bogatyreva, G.P.; Grankina, T.Y.; Krasil'nikova, O.K.; Plotnikova, E. V.; Spitsyn, B. V. Adsorption and electrical properties of nanodiamond

powders in the presence of water vapor. *Prot. Met. Phys. Chem. Surfaces* **2013**, *49*, 286–291, doi:10.1134/S2070205113030088.

129. Piña-Salazar, E.-Z.; Sagisaka, K.; Hattori, Y.; Sakai, T.; Futamura, R.; Ōsawa, E.; Kaneko, K. Electrical conductivity changes of water-adsorbed nanodiamonds with thermal treatment. *Chem. Phys. Lett. X* **2019**, *2*, 100018, doi:10.1016/j.cpletx.2019.100018.

130. Aprà, P.; Ripoll-Sau, J.; Manzano-Santamaría, J.; Munuera, C.; Forneris, J.; Ditalia Tchernij, S.; Olivero, P.; Picollo, F.; Vittone, E.; Ynsa, M.D. Structural characterization of 8 MeV 11B implanted diamond. *Diam. Relat. Mater.* **2020**, *104*, 107770, doi:10.1016/j.diamond.2020.107770.

131. Created by Mike jones - https://creativecommons.org/licenses/by-sa/3.0/.

132. Modified and converted to SVG by Mjones1984. Original work by Larryisgood - https://creativecommons.org/licenses/by-sa/3.0/.

133. Zeta potential: An Introduction in 30 minutes. *Zetasizer Nano Serles Tech. Note. MRK654-01* **2011**, *2*, 1–6.

134. Measuring Zeta Potential – Laser Doppler Electrophoresis. *Malvern Guid.* **2015**, 1–2.

135. Malvern Panalytical Ltd Measuring zeta potential using phase analysis light scattering (PALS). *Malvern Guid.* **2014**, 1–3.

136. Yan, X.; Wei, J.; An, K.; Liu, J.; Chen, L.; Zheng, Y.; Zhang, X.; Li, C. High temperature surface graphitization of CVD diamond films and analysis of the kinetics mechanism. *Diam. Relat. Mater.* **2021**, *120*, 108647, doi:10.1016/j.diamond.2021.108647.

137. Piccardo, M.; Bosia, F.; Olivero, P.; Pugno, N. An analytical model for the mechanical deformation of locally graphitized diamond. *Diam. Relat. Mater.* **2014**, *48*, 73–81, doi:10.1016/j.diamond.2014.07.006.

138. García, G.; Preda, I.; Díaz-Híjar, M.; Tormo-Márquez, V.; Peña-Rodríguez, O.; Olivares, J.; Bosia, F.; Pugno, N.M.; Picollo, F.; Giuntini, L.; et al. Micro and nano-patterning of single-crystal diamond by swift heavy ion irradiation. *Diam. Relat. Mater.* **2016**, *69*, 1–7, doi:10.1016/j.diamond.2016.06.015.

139. Bosia, F.; Calusi, S.; Giuntini, L.; Lagomarsino, S.; Lo Giudice, A.; Massi, M.; Olivero, P.; Picollo, F.; Sciortino, S.; Sordini, A.; et al. Finite element analysis of ion-implanted diamond surface swelling. *Nucl. Instruments Methods Phys. Res. Sect. B Beam Interact. with Mater. Atoms* **2010**, *268*, 2991–2995, doi:10.1016/j.nimb.2010.05.025.

140. Amekura, H.; Kishimoto, N. Effects of high-fluence ion implantation on colorless diamond self-standing films. *J. Appl. Phys.* **2008**, *104*, 063509, doi:10.1063/1.2978215.

141. Born, M.; Wolf, E. *Principles of optics: electromagnetic theory of propagation, interference and diffraction of light*; Elsevier, 2013;

142. Battiato, A.; Bosia, F.; Ferrari, S.; Olivero, P.; Sytchkova, A.; Vittone, E. Spectroscopic measurement of the refractive index of ion-implanted diamond. *Opt. Lett.* **2012**, *37*, 671, doi:10.1364/OL.37.000671.

143. Orwa, J.O.; Nugent, K.W.; Jamieson, D.N.; Prawer, S. Raman investigation of damage caused by deep ion implantation in diamond. *Phys. Rev. B* **2000**, *62*, 5461–5472, doi:10.1103/PhysRevB.62.5461.

144. Liu, M.S.; Bursill, L.A.; Prawer, S.; Beserman, R. Temperature dependence of the first-order Raman phonon line of diamond. *Phys. Rev. B* **2000**, *61*, 3391–3395, doi:10.1103/PhysRevB.61.3391.

145. Rigato, V. Interdisciplinary physics with small accelerators at LNL: Status and perspectives.; 2013; pp. 29–34.

146. Hepp, C.; Müller, T.; Waselowski, V.; Becker, J.N.; Pingault, B.; Sternschulte, H.; Steinmüller-Nethl, D.; Gali, A.; Maze, J.R.; Atatüre, M.; et al. Electronic Structure of the Silicon Vacancy Color Center in Diamond. *Phys. Rev. Lett.* **2014**, *112*, 036405, doi:10.1103/PhysRevLett.112.036405.

147. Prestopino, G.; Marinelli, M.; Milani, E.; Verona, C.; Verona-Rinati, G.; Traina, P.; Moreva, E.; Degiovanni, I.P.; Genovese, M.; Ditalia Tchernij, S.; et al. Photo-physical properties of He-related color centers in diamond. *Appl. Phys. Lett.* **2017**, *111*, 111105, doi:10.1063/1.4996825.

148. Forneris, J.; Tengattini, A.; Tchernij, S.D.; Picollo, F.; Battiato, A.; Traina, P.; Degiovanni, I.P.; Moreva, E.; Brida, G.; Grilj, V.; et al. Creation and characterization of He-related color centers in diamond. *J. Lumin.* **2016**, *179*, 59–63, doi:10.1016/j.jlumin.2016.06.039.

149. Prawer, S.; Nemanich, R.J. Raman spectroscopy of diamond and doped diamond. *Philos. Trans. R. Soc. London. Ser. A Math. Phys. Eng. Sci.* **2004**, *362*, 2537–2565, doi:10.1098/rsta.2004.1451.

150. Olivero, P.; Bosia, F.; Fairchild, B.A.; Gibson, B.C.; Greentree, A.D.; Spizzirri, P.; Prawer, S. Splitting of photoluminescent emission from nitrogen–vacancy centers in diamond induced by ion-damage-induced stress. *New J. Phys.* **2013**, *15*, 043027, doi:10.1088/1367-2630/15/4/043027.

151. Picollo, F.; Gatto Monticone, D.; Olivero, P.; Fairchild, B.A.; Rubanov, S.; Prawer, S.; Vittone, E. Fabrication and electrical characterization of three-dimensional graphitic microchannels in single crystal diamond. *New J. Phys.* **2012**, *14*, 053011, doi:10.1088/1367-2630/14/5/053011.

152. Pierson, H.O. Graphite Structure and Properties. In *Handbook of Carbon, Graphite, Diamonds and Fullerenes*; Elsevier, 1993; pp. 43–69.

153. Brocher, J. The BioVoxxel Image Processing and Analysis Toolbox 2015.

154. Tyurnina, A. V.; Apolonskaya, I.A.; Kulakova, I.I.; Kopylov, P.G.; Obraztsov, A.N. Thermal purification of detonation diamond. *J. Surf. Investig. X-ray, Synchrotron Neutron Tech.* **2010**, *4*, 458–463, doi:10.1134/S102745101003016X.

155. Stelmakh, S.; Skrobas, K.; Gierlotka, S.; Palosz, B. Atomic structure of nanodiamond and its evolution upon annealing up to 1200 °C: Real space neutron diffraction analysis supported by MD simulations. *Diam. Relat. Mater.* **2019**, *93*, 139–149, doi:10.1016/j.diamond.2019.02.004.

156. Krueger, A.; Lang, D. Functionality is Key: Recent Progress in the Surface Modification of Nanodiamond. *Adv. Funct. Mater.* **2012**, *22*, 890–906, doi:10.1002/adfm.201102670.

157. Lowry, G. V.; Hill, R.J.; Harper, S.; Rawle, A.F.; Hendren, C.O.; Klaessig, F.; Nobbmann, U.; Sayre, P.; Rumble, J. Guidance to improve the scientific value of zeta-potential measurements in nanoEHS. *Environ. Sci. Nano* **2016**, *3*, 953–965, doi:10.1039/C6EN00136J.

158. Spitsyn, B.V.; Davidson, J.L.; Gradoboev, M.N.; Galushko, T.B.; Serebryakova, N.V.; Karpukhina, T.A.; Kulakova, I.I.; Melnik, N.N. Inroad to modification of detonation nanodiamond. *Diam. Relat. Mater.* **2006**, *15*, 296–299, doi:10.1016/j.diamond.2005.07.033.

159. Stehlik, S.; Petit, T.; Girard, H.A.; Arnault, J.-C.; Kromka, A.; Rezek, B. Nanoparticles Assume Electrical Potential According to Substrate, Size, and Surface Termination. *Langmuir* **2013**, *29*, 1634–1641, doi:10.1021/la304472w.

160. Ji, S.; Jiang, T.; Xu, K.; Li, S. FTIR study of the adsorption of water on ultradispersed diamond powder surface. *Appl. Surf. Sci.* **1998**, *133*, 231–238, doi:10.1016/S0169-4332(98)00209-8.

161. Mino, L.; Negri, C.; Santalucia, R.; Cerrato, G.; Spoto, G.; Martra, G. Morphology, Surface Structure and Water Adsorption Properties of TiO2 Nanoparticles: A Comparison of Different Commercial Samples. *Molecules* **2020**, *25*, 4605, doi:10.3390/molecules25204605.

162. Petit, T.; Puskar, L. FTIR spectroscopy of nanodiamonds: Methods and interpretation. *Diam. Relat. Mater.* **2018**, *89*, 52–66, doi:10.1016/j.diamond.2018.08.005.

163. Shenderova, O.; Panich, A.M.; Moseenkov, S.; Hens, S.C.; Kuznetsov, V.; Vieth, H.-M. Hydroxylated Detonation Nanodiamond: FTIR, XPS, and NMR Studies. *J. Phys. Chem. C* **2011**, *115*, 19005–19011, doi:10.1021/jp205389m.

164. Mino, L.; Barzan, C.; Martino, G.A.; Piovano, A.; Spoto, G.; Zecchina, A.; Groppo, E. Photoinduced Ethylene Polymerization on the Cr VI /SiO 2 Phillips Catalyst. *J. Phys. Chem. C* **2019**, *123*, 8145–8152, doi:10.1021/acs.jpcc.8b08118.

165. Zhu, S.; Panne, U.; Rurack, K. A rapid method for the assessment of the surface group density of carboxylic acid-functionalized polystyrene microparticles. *Analyst* **2013**, *138*, 2924, doi:10.1039/c3an36578f.

166. Hu, W.; Li, Z.; Yang, J. Surface and size effects on the charge state of NV center in nanodiamonds. *Comput. Theor. Chem.* **2013**, *1021*, 49–53, doi:10.1016/j.comptc.2013.06.015.

167. Gatto Monticone, D.; Quercioli, F.; Mercatelli, R.; Soria, S.; Borini, S.; Poli, T.; Vannoni, M.; Vittone, E.; Olivero, P. Systematic study of defect-related quenching of NV luminescence in diamond with time-correlated single-photon counting spectroscopy. *Phys. Rev. B* **2013**, *88*, 155201, doi:10.1103/PhysRevB.88.155201.

168. Laube, C.; Oeckinghaus, T.; Lehnert, J.; Griebel, J.; Knolle, W.; Denisenko, A.; Kahnt, A.; Meijer, J.; Wrachtrup, J.; Abel, B. Controlling the fluorescence properties of nitrogen vacancy centers in nanodiamonds. *Nanoscale* **2019**, *11*, 1770–1783, doi:10.1039/C8NR07828A.

169. Pezzagna, S.; Naydenov, B.; Jelezko, F.; Wrachtrup, J.; Meijer, J. Creation efficiency of nitrogen-vacancy centres in diamond. *New J. Phys.* **2010**, *12*, 065017, doi:10.1088/1367-2630/12/6/065017.

170. Orwa, J.O.; Ganesan, K.; Newnham, J.; Santori, C.; Barclay, P.; Fu, K.M.C.; Beausoleil, R.G.; Aharonovich, I.; Fairchild, B.A.; Olivero, P.; et al. An upper limit on the lateral vacancy diffusion length in diamond. *Diam. Relat. Mater.* **2012**, *24*, 6–10, doi:10.1016/j.diamond.2012.02.009.

171. Zeng, G.; Liu, M.; Shi, K.; Heng, C.; Mao, L.; Wan, Q.; Huang, H.; Deng, F.; Zhang, X.; Wei, Y. Surface modification of nanodiamond through metal free atom transfer radical polymerization. *Appl. Surf. Sci.* **2016**, *390*, 710–717, doi:10.1016/j.apsusc.2016.08.154.

172. Zhang, X.; Fu, C.; Feng, L.; Ji, Y.; Tao, L.; Huang, Q.; Li, S.; Wei, Y. PEGylation and polyPEGylation of nanodiamond. *Polymer (Guildf).* **2012**, *53*, 3178–3184, doi:10.1016/j.polymer.2012.05.029.

173. Yeap, W.S.; Chen, S.; Loh, K.P. Detonation Nanodiamond: An Organic Platform for the Suzuki Coupling of Organic Molecules. *Langmuir* **2009**, *25*, 185–191, doi:10.1021/la8029787.

174. Gaur, P.; Banerjee, S. C-N cross coupling: Novel approach towards effective aryl secondary amines modification on nanodiamond surface. *Diam. Relat. Mater.* **2019**, *98*, 107468, doi:10.1016/j.diamond.2019.107468.

175. Lang, D.; Krueger, A. The Prato reaction on nanodiamond: Surface functionalization by formation of pyrrolidine rings. *Diam. Relat. Mater.* **2011**, *20*, 101–104, doi:10.1016/j.diamond.2010.09.001.

176. Jarre, G.; Liang, Y.; Betz, P.; Lang, D.; Krueger, A. Playing the surface game—Diels–Alder reactions on diamond nanoparticles. *Chem. Commun.* **2011**, *47*, 544–546, doi:10.1039/C0CC02931A.

177. Bardelli, A.; Jänne, P.A. The road to resistance: EGFR mutation and cetuximab. *Nat. Med.* **2012**, *18*, 199.

178. Aprà, P.; Mino, L.; Battiato, A.; Olivero, P.; Sturari, S.; Valsania, M.C.; Varzi, V.; Picollo, F. Interaction of Nanodiamonds with Water: Impact of Surface Chemistry on Hydrophilicity, Aggregation and Electrical Properties. *Nanomaterials* **2021**, *11*, 2740, doi:10.3390/nano11102740.

179. Petrini, G.; Moreva, E.; Bernardi, E.; Traina, P.; Tomagra, G.; Carabelli, V.; Degiovanni, I. Pietro; Genovese, M. Is a Quantum Biosensing Revolution Approaching? Perspectives in NV-Assisted Current and Thermal Biosensing in Living Cells. *Adv. Quantum Technol.* **2020**, *3*, 2000066, doi:10.1002/qute.202000066.

180. Acosta, V.M.; Bauch, E.; Ledbetter, M.P.; Waxman, A.; Bouchard, L.-S.; Budker, D. Temperature Dependence of the Nitrogen-Vacancy Magnetic Resonance in Diamond. *Phys. Rev. Lett.* **2010**, *104*, 070801, doi:10.1103/PhysRevLett.104.070801.